CHALMERS UNIVERSITY OF TECHNOLOGY
Gothenburg, Sweden
www.chalmers.se

LICENTIATE THESIS

YINGQI ZHANG • Wideband and Wide-Scan Gap Waveguide Antenna Array at W-band for 6G Applications • 2023

Wideband and Wide-Scan Gap Waveguide Antenna Array at W-band for 6G Applications

YINGQI ZHANG

DEPARTMENT OF ELECTRICAL ENGINEERING
CHALMERS UNIVERSITY OF TECHNOLOGY
Gothenburg, Sweden 2023
www.chalmers.se

THESIS FOR THE DEGREE OF LICENTIATE OF ENGINEERING

Wideband and Wide-Scan Gap Waveguide Antenna Array at W-band for 6G Applications

Yingqi Zhang

Department of Electrical Engineering
Chalmers University of Technology
Gothenburg, Sweden, 2023

Wideband and Wide-Scan Gap Waveguide Antenna Array at W-band for 6G Applications

Yingqi Zhang

Department of Electrical Engineering

Chalmers University of Technology
SE-412 96 Gothenburg, Sweden
Phone: +46 (0)31 772 1000
www.chalmers.se

Printed by Chalmers Reproservice
Gothenburg, Sweden, June2023

朝聞道，夕死可矣

Abstract

The future wireless communication for 6G (or beyond 5G) holds the promise to reach Tbps level throughput at distances $\geq$ 1 km with flexible user mobility. The upper millimeter-wave bands (100+ GHz), especially W- and D-band, are being widely considered for these applications. In this context, high-gain mm-wave antenna systems with intelligent beam-forming are seen as the key technological enablers. However, high dissipation losses, components cost, and tight manufacturing tolerances at these frequencies severely restrict suitability of the traditional phased antenna array solutions.

This work attempts to fill in this knowledge gap by presenting a new array antenna type based on the open-ended ridge gap waveguide (RGW). Such an antenna is of a particular interest at 100+ GHz owing to its contactless waveguide sidewall design, which alleviates active beam-steering electronics integration. Its fractional bandwidth is broadened by a relatively simple wide-band impedance matching network, consisting of an aperture stepped ridge segment and a single-pin RGW section. Furthermore, the E- and H-plane grooves are added that effectively suppress antenna elements mutual coupling effects when used in arrays of such elements. Results demonstrate a wide-angle beam-steering range ($\geq 50°$) over $\geq 20\%$ bandwidth at W-band, with $\geq 89\%$ radiation efficiency. This significantly outperforms existing solutions at these frequencies. An experimental prototype of a 1×19 W-band array validates the proposed design concept through the embedded element pattern measurements.

In the second part of this Licentiate thesis, we present a linear array architecture as a building block of 2D arrays that can enable efficient beam-steering and a simplified array design. It includes a low-loss gap waveguide-based quasi-optical (QO) feed to provide a desired antenna port excitation with 1- /2-bit phase shifters which are co-integrated with the array antenna elements. The array design goals, i.e. the maximum available gain and minimum sidelobe levels are achieved through the optimum quasi-randomization of phase errors through the QO feed. The relationships between the key design parameters of the QO feed are determined analytically. The system-level performance for above-mentioned goals is studied numerically based on cascading the simulated / measured results of each individual system component: the QO feed, the RGW-to-phase-shifter transitions, the on-chip phase-shifters, and the array antennas.

Keywords: Array antenna, beam steering, W-band, ridge gap waveguide, quasi-optical feed.

List of Publications

This thesis is based on the following publications:

[A] **Y. Zhang**, A. R. Vilenskiy, M. V. Ivashina, "W-band Waveguide Antenna Elements for Wideband and Wide-Scan Array Antenna Applications For Beyond 5G". *2021 15th European Conference on Antennas and Propagation (EuCAP)*, Dusseldorf, Germany, Mar. 2021.

[B] **Y. Zhang**, A. R. Vilenskiy, M. V. Ivashina, "Wideband Open-Ended Ridge Gap Waveguide Antenna Elements for 1-D and 2-D Wide-Angle Scanning Phased Arrays at 100 GHz". *IEEE Antennas and Wireless Propagation Letters*, vol. 21, no: 5, pp. 883 - 887, 2022.

[C] **Y. Zhang**, A. R. Vilenskiy, M. V. Ivashina, "Mutual Coupling Analysis of Open-Ended Ridge and Ridge Gap Waveguide Radiating Elements in an Infinite Array Environment". *2022 52nd European Microwave Conference (EuMC)*, Milan, Italy, Sept. 2022.

[D] A. R. Vilenskiy, **Y. Zhang**, M. V. Ivashina, "Methods for Attenuating and Terminating Waves in Ridge Gap Waveguide at W-Band: Carbon-Loaded Foam, Carbonyl Iron Paint, and Nickel Plating". *2021 51st European Microwave Conference (EuMC)*, London, United Kingdom, Apr. 2022.

[E] A. R. Vilenskiy, **Y. Zhang**, E. Galesloot, A. B. Smolders, M. V. Ivashina, "Millimeter-Wave Quasi-Optical Feeds for Linear Array Antennas in Gap Waveguide Technology". *2022 16th European Conference on Antennas and Propagation (EuCAP)*, Madrid, Spain, Apr. 2022.

[F] A. R. Vilenskiy, E. Galesloot, **Y. Zhang**, A. B. Smolders, M. V. Ivashina, "Quasi-Optical Beamforming Network for Millimeter-Wave Electronically Scanned Array Antennas with 1-Bit Phase Resolution". *2021 15th European Conference on Antennas and Propagation (EuCAP)*, Dusseldorf, Germany, Mar. 2021.

Acknowledgments

In the realm of academia, solitary journeys are rare. On the cusp of completion, I reflect on those who illuminated my path.

Foremost, I extend my heartfelt gratitude to my supervisor, Prof. Marianna Ivashina, whose wisdom and patience have been instrumental in guiding my academic journey. Her unwavering trust and encouragement have been a significant source of inspiration, for which I am profoundly grateful.

I am indebted to Prof. Bart Smolders for his supervision at TU/e under the dual-degree program. My co-supervisor, Dr. Artem R. Vilenskiy, has offered invaluable insights, serving as a guiding compass in my research.

I express my gratitude to my colleagues and friends at the Antenna Group (Chalmers) and Microwave Electronics Laboratory (Chalmers). Your assistance, insightful advice, and invaluable help with my measurements have been instrumental in my research. Furthermore, I am thankful to the EU H2020-MSCA-ITN Mywave Project for the financial support, academic training opportunities, resources, and the amicable community. Our shared intellectual endeavors, moments of joy, and mutual bewilderment have enriched this journey.

To my cherished family, late grandmother, and husband, your resilience and unwavering support have been a beacon. Despite geographical separation and global adversities, your love has bridged the distance. Your steadfast presence has been my bulwark against isolation. The love and educational opportunities you provided have driven my academic advancement. I deeply appreciate your sacrifices and support.

Lastly, I acknowledge the scholarly giants whose work provided a solid foundation for my own. Their pursuit of knowledge served as a guiding light in my explorations.

This Licentiate thesis, though authored by one, is genuinely the product of many. It stands as a testament to collective efforts. To all, I express profound appreciation.

Acronyms

5G:	the fifth-generation of cellular networks
6G:	the sixth generation of cellular networks
ABS:	absorber
AF:	array factor
AiP:	antenna-in-package
AoC:	antenna-on-chip
B5G:	beyond 5G
BFIC:	beamforming integrated circuits
BiCMOS:	bipolar complementary metal oxide semiconductor
CATR:	compact antenna test range
CMOS:	complementary metal oxide semiconductor
CNC:	computerized numerical control
EBG:	electromagnetic bandgap
EEP:	embedded element pattern
EIRP:	effective isotropic radiated power
eWLB:	embedded wafer level ball grid array
FSPL:	free space path loss
GaAs:	gallium-arsenide
GaN:	gallium-nitride
GGW:	groove gap waveguide
GWG:	gap waveguide

HDI:	high density interconnect
IC:	integrated circuits
InP:	indium-phosphide
LNA:	low noise amplifier
LTCC:	low temperature co-Fired ceramic
MLO:	multi-layer organic polymer
MMIC:	monolithic microwave integrated circuits
mmWave:	millimeter-wave
PA:	power amplifier
PAA:	phased array antenna
PBC:	periodic boundary condition
PCB:	printed circuit board
PS:	phase-shifter
QO:	quasi-optical
RF:	radio frequency
RGW:	ridge gap waveguide
RX:	receiver
SC:	scientific contribution
Si:	silicon
SiGe:	Silicon Germanium
SLL:	side lobe level
SNR:	signal-to-noise ratio
THz:	terahertz
TX:	transmitter
WG:	waveguide

Contents

II Papers 75

Part I

Introductory chapters

CHAPTER 1

Introduction

The introduction of the thesis begins by outlining the motivation for research in the context of the current wireless communication environment. The specific design considerations and challenges associated with 100+ GHz array antennas are then discussed from various perspectives. Following this, a summary of the scientific contributions made by this thesis is provided to give a comprehensive overview of our work. Finally, the outline of the thesis is presented, detailing the structure and content of the subsequent chapters.

1.1 Motivation

The future wireless communication beyond 5G such as 5G advance and 6G hold the promise to reach Tbps level throughput at distances $\geq$ 1 km with flexible user mobility [1]. The upper millimeter-wave (mmWave) bands (100+ GHz), especially W-band (75–110 GHz) and D-band (110–170 GHz), are being widely considered for these applications, owing to the wide available bandwidth, a relatively low atmospheric attenuation, and cm-level positioning accuracy. The low part of these bands have already been explored for the automotive radar applications as well as in backhauling wireless links and multi-user wireless communications [2].

In the wireless channels at higher frequencies, the free space path loss (FSPL) with omnidirectional antennas increase with the operating frequencies and the distance (d) between the transmitter (TX) and receiver (RX). The block diagram of a wireless link example is shown in Fig. 1.1, and according to the following equations:

The receiving power of RX is:

$$P_r = \frac{P_t G_t G_r}{L_p} \tag{1.1}$$

where (Gt, Gr) and (Pt, Pr) stand for transmitted/received antenna gain and power, and L_p is the loss (a reduction factor) between TX and RX antenna.

$$L_p = \frac{(4\pi d)^2}{\lambda^2} \tag{1.2}$$

where λ is the wavelength in free space.

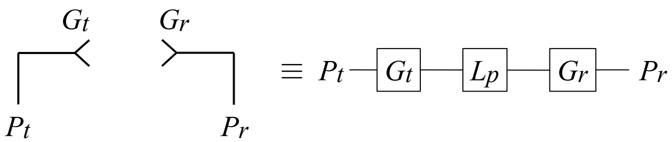

Figure 1.1: Block diagram of a simplified wireless link.

Substituting (1.2) into (1.1) we get:

$$P_r = \frac{P_t G_t G_r \lambda^2}{(4\pi d)^2} \tag{1.3}$$

or,

$$\mathrm{P_{r\ dB}} = \mathrm{P_{t\ dBm}} + \mathrm{G_{t\ dBi}} + \mathrm{G_{r\ dBi}} - \mathrm{L_{p\ dB}} \tag{1.4}$$

As gain of the antenna can be expressed as:

$$G = \frac{A_e 4\pi}{\lambda^2} \tag{1.5}$$

where A_e is the effective aperture of the antenna. Substituting (1.5) into (1.3), we have:

$$\frac{P_r}{P_t} = \frac{G_t G_r \lambda^2}{(4\pi d)^2} \tag{1.6}$$

here, (1.6) is the ideal model for FSPL assumes no obstacles, operating in vacuum.

However, it is important to note that the mmWave antennas (for a given physical size) will be more directional and have more gain. Friis free space equation (1.4) readily demonstrate that higher frequency links are viable with less loss, not more. With directional antennas at both link ends, theoretically the path loss in free space decreases quadratically as frequency increases, so long as the physical size of the antenna (effective aperture A_e) is kept constant over frequency at both link ends [3], [4].

For instance, research has been conducted comparing propagation measurements of transceiver links at 28, 73, and 140 GHz [4]. As depicted in Fig. 1.2(a), the measured path loss at different frequencies aligns well with the free space path loss (FSPL) equation given by Eq. 1.3. The enhanced coverage at higher frequencies for a constant antenna aperture at both ends of the link is illustrated in Fig. 1.2(b). Here, the received power in free space at 140 GHz is 5.7 dB and 14 dB greater than the power received at 73 GHz and 28 GHz, respectively, for the same TX output power and identical physical antenna areas at all frequencies.

These findings suggest that superior wireless links at higher frequencies enable the use of wider bandwidths while maintaining the same signal-to-noise ratio as at lower frequencies. It drives the research in 100+ GHz phased array antennas (PAAs) with electronic beam-steering that can provide a broad coverage and high energy efficiency [5].

1.2 100 GHz array antenna design and challenges

In this context, high-gain/efficiency mmWave antenna systems with intelligent beam-forming are seen as the key technological enablers of the next-generation telecommunication systems, capable to compensate the considerable free-space path loss, material losses and reduced power generation ability of active electronic devices at these frequencies. To satisfy these requirements, PAAs must generate high effective isotropic radiated power (EIRP) in the transmit mode, and high receiving sensitivity (or high signal-to-noise ratio

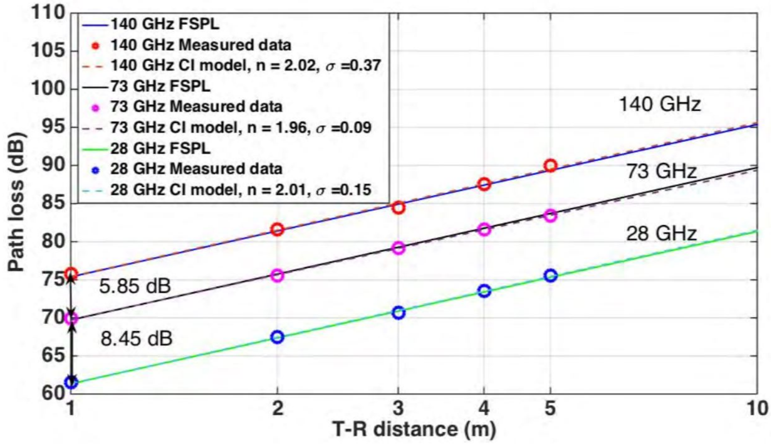

(a)

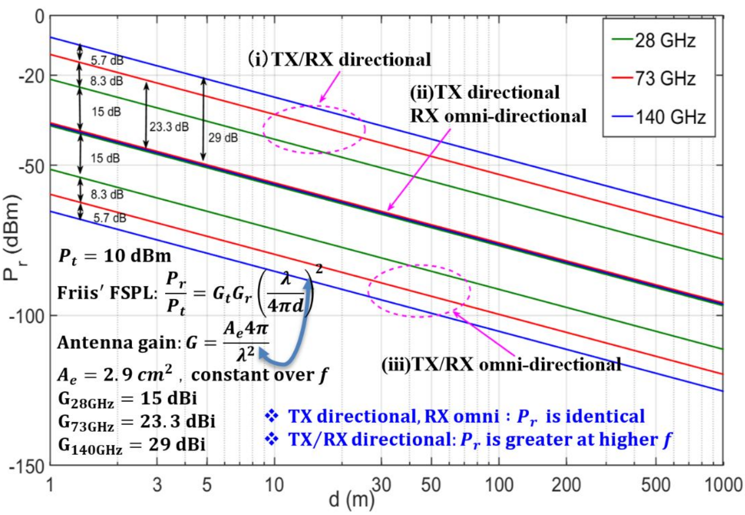

(b)

Figure 1.2: (a) 28, 73 and 140 GHz free space path loss (after subtracting out all antenna gains) verification measurements at distances of 1, 2, 3, 4, and 5 m. (b) Received power vs. distance with (i) TX and RX are both directional, (ii) TX is directional but RX is omni-directional, and (iii) both TX and RX are omni-directional at 28 GHz, 73 GHz, and 140 GHz. Directional antennas with equal effective aperture (A_e = 2.9 cm^2) at both TX and RX have much less path loss at higher frequencies [2]–[4].

(SNR)) in the receiver mode. These merits are mainly determined by the i) gain/efficiency of the PAAs; ii) the peak output power (P_{sat}) and power-added efficiency (PAE) and linearity of the power amplifiers (PA); iii) noise figure (NF) of the low noise amplifiers (LNA); iv) and the insertion/dissipation loss of interconnections and feeding lines in the system.

To achieve high gain and efficient PAAs, significant efforts are being dedicated to designing array antennas with many array elements. Conventionally such PAAs are fed through equal line-length corporate feeds and then connected to phase-shifter circuits and transmission lines or other types of transitions from the antenna port to the integrated circuits (ICs) [6]. For an N-element phased array, the EIRP in transmit mode is proportional to N^2[7]. For instance, a 1024-element Silicon-based phased array at 94 GHz can establish a link at over 10 km, whereas a 64-element array can only cover a few meters [8]. In addition, larger phased arrays can generate narrow (pencil) beams with larger flexibility of beam-steering, resulting in spatial filtering capabilities.

However, designing the phased arrays at W-/D-band is challenging as the antenna geometrical features and the required grating-lobe free physical inter-element spacing ($0.5\lambda_0 = 1.5mm$ at 100 GHz) become significantly smaller than those at traditional sub-6 GHz bands and 5G-adapted mmWave band (24–40 GHz). As a consequence, integrating modular antenna circuits with conventional beam-forming networks becomes difficult due to the physical constraints in accessing and feeding each antenna element port. This is especially critical for large-scale arrays of closely spaced antenna elements as required for wide-angle beam-steering.

The aforementioned requirements necessitate tighter manufacturing tolerances in suitable materials capable of implementing array antennas with high gain and efficiency. In recent mmWave phased array designs, the PAAs and ICs are integrated into modules with one or more substrates stacked vertically or laterally. This approach is advantageous for supporting a large number of antenna elements with flexibility in terms of beam-forming implementation [9]. The architectures represented in these designs include Antenna-in-Package (AiP) and Antenna-on-Chip (AoC) systems, where PAAs are implemented on the first-level package in substrates with higher dielectric constants (embedded wafer level ball grid array (eWLB): 3.2; high density interconnect (HDI): 2.8–4.6; low temperature co-fired ceramic (LTCC): 5–7.8; quartz 3.8 [10], [11]) than those of printed circuit boards (PCB). This allows for thinner line widths and pitches that are beneficial for designing antenna variations, interconnections to ICs, and radio frequency (RF) signal routing. However, the high dielectric constants combined with high loss tangents (0.003–0.008) in these materials at W-/D-bands can also deteriorate radiation efficiency and result in significant insertion loss in transmission lines.

The RF power supply, specifically power amplifiers, is another crucial design factor that contributes to the system EIRP and array scaling rules. Despite the availability of various semiconductor technologies, it remains challenging to develop efficient high-power and cost-effective in-system packaging solutions in the W-/D-band. The key TX/RX metrics of ii) the P_{sat}, PAE and linearity of PAs and iii) the NF of the LNAs degrade rapidly with increasing operating frequency according to the reported PA survey as Fig. 1.3 shows [4], [12]. III-V compound semiconductors, such as gallium-arsenide (GaAs), gallium-nitride (GaN), and indium-phosphide (InP), have the potential to generate more power at mmWave frequencies compared to silicon (Si). However, their relatively low thermal conductivity limits the maximum power density, resulting in devices with larger areas. The relatively lower level of integration for III-V compound devices has also restricted their mainstream use. Therefore, most reported packaging solutions utilize silicon-based technologies (SiGe BiCMOS and Si CMOS processes) [13], [14] at 24–60 GHz bands, but fewer solutions have been presented for W-/D-bands.

The above-discussed difficulties steer the 100 GHz PAAs research towards non-conventional phased array architectures with hybrid integration solutions, such as Antenna-in-Module phased arrays that integrate active circuits into antennas [15], and beam-forming networks with reduced-order controls: e.g., quasi-optical feeding networks or modular sub-array feeds. Examples include transmitarrays, active lens antennas and multi-beam antennas. Such non-conventional solutions demonstrate high gain for the optics defined excitation scenario, and can be implemented in low-cost technology with low insertion loss. However, these solutions are more complex in design and lack well-established implementations especially at W-/D-band.

1.3 Scientific contributions of the thesis

Original scientific contributions (SCs) of this thesis are discussed below:

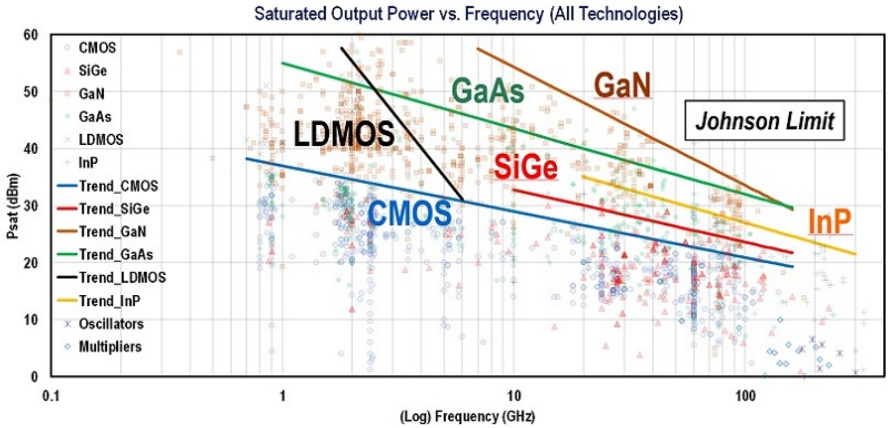

Figure 1.3: Saturated output power vs. frequency from the cited PA works since 2000 [12].

We propose a full-metallized reconfigurable active array design at 100 GHz that addresses the critical design and manufacturing challenges at these high frequencies. This design employs an antenna subarray modularization approach and hierarchical array beam-forming. In this way, the 2-D beam-steering is realized by traditional electronic beam-forming ICs (BFIC) in one plane, and by hybrid beam-forming control combining a quasi-optical feed and low-bit phase-shifters in the orthogonal plane. We demonstrate a 1-D subarray (linear array) by de-composing the key design steps and the associated SCs as follows:

1. A novel antenna element type based on the open-ended ridge gap waveguide (RGW) and its implementation solutions are proposed for application in 1-D and 2-D wide-angle scanning phased arrays. The RGW features contactless metal sidewalls, which facilitate the integration of active beam-steering electronics. Results demonstrate a wide-angle beam-steering ($\geq$ 50°) over $\geq$ 20% fractional bandwidth at W-band with $\geq$ 89% radiation efficiency that significantly outperforms existing solutions (e.g. patch antennas, dipoles) at these frequencies. The proposed design concept is validated in a 1×19 array through the embedded element pattern measurements. (*presented in Paper* A, B, D)

2. A quasi-optical (QO) feed for linear millimeter-wave (sub-)array antennas in gap waveguide technology is demonstrated. The proposed feed employs an input ridge gap waveguide (RGW), an H-plane sectoral groove gap waveguide (GGW) section, and a transition to an output RGW array. Several 20-element QO feed implementations are investigated demonstrating a 20% relative bandwidth (85–105 GHz), 0.5 dB insertion loss, and the capability of the amplitude taper control within the 3-20 dB range. An analytical approach based on the modal contents for controlling the amplitude taper of the QO feed is proposed. (*presented in Paper* E, F; collaborated work)

3. A system-level numerical analysis of the hybrid beam-forming linear (sub-)array antenna including the spatial QO beam-forming network is presented. This analysis is done by cascading the scattering parameters of the individual system components and applying optimal beam-forming coefficients to the array elements to obtain the beam-steered radiation patterns.

4. A numerical study of mutual coupling effects in 2-D beam-steerable antenna arrays of open-ended ridge waveguide (WG) and ridge gap waveguide (RGW) radiating elements is presented to demonstrate the decoupling impacts of the grooves structures and protruding pins in the array aperture that extends achievable beam-steering range. This analysis demonstrates the inter-element mutual coupling levels ≤ -20 dB for the proposed RGW array elements with both E-/H-plane grooves or pins with a wideband ($\geq 20\%$) and wide-scan ($\geq 50^o$) performance. (*presented in Paper* C)

1.4 Outline

Following the introduction, Chapter 2 presents a review of the state-of-the-art W-/D-band PAAs. In Chapter 3, a new type of RGW-based wide-band, wide-scan PAA is proposed. A comparative analysis of the beam-steering capabilities and mutual coupling effects of the WG and RGW PAAs with various decoupling structures is conducted. An experimental study of the proposed RGW antenna in a linear array is also demonstrated. In Chapter 4, a QO feed for linear array antennas is proposed. A system-level numerical analysis of the hybrid beam-forming linear array antenna, including the QO beam-forming network, is presented.

CHAPTER 2

W-/D-band State-of-art Array Antennas

To address the design challenges associated with beam-steering array antennas for 6G applications in the W-/D-band, various architectural options have been developed to balance system package design complexity, cost, and achievable performance metrics such as impedance bandwidth and radiated power. The prevalent solutions for implementing conventional PAAs include Antenna-in-Package (AiP) and Antenna-on-Chip (AoC) systems. These systems are advantageous for phased-array scaling, allowing for the creation of phased arrays by combining repeatable ICs and/or antenna units with low-loss interconnections [7], [16]. Typical limitations are low radiation efficiency, small scan range and narrow bandwidth. However, creating high-gain array antennas in these technologies can be expensive due to the need for large apertures and the associated high chip area cost. In addition to conventional PAA solutions, non-conventional PAA solutions such as lens and transmitarrays are also being used to reduce cost (e.g. less components and chip area), though at the price of the reduced performance: e.g., beam-steering flexibility and multi-functionality. These solutions create electronic beam control in a hybrid way, by combining the quasi-optical structures with active integrated circuits. Various state-of-art W-/D-band PAA designs are compared in Table

2.1 and discussed in the following sections.

2.1 Conventional PAAs

At lower mmWave frequencies, Antenna-on-PCB technology is a commonly used as the cost-effective solution. In this approach, the radio-frequency integrated circuits (RFIC) are flip-chip bonded to the board on the opposite side from the direction of radiation. However, wire bonding the ICs cannot meet the tight pitch demands required for array scalability, and maintaining radiation efficiency in a lossy material with tight manufacturing tolerance present challenges, limiting its applications to the W-/D-bands. In 2018-2019, Nokia Bell Labs presented a tiling architecture with one IC per 24-antenna tiles in a 384-element phased array for point-to-multipoint applications at 91 GHz [17] as shown in Fig. 2.1(a). Although the significant amounts of elements enable high gain, the scan ability is very limited ($\pm 20°$) due to the tight feeding networks distribution that impose a 0.63λ spacing between the elements.

To reduce the interconnections between discrete antennas and beamformer ICs, Antenna-in-Pacakge (AiP) technology implements antennas with transceiver dies into a standard surface-mounted device [10], [14]. Substrate technologies suitable for implementing the array modules include LTCC (low-temperature co-fired ceramic) [19], multi-layer organic polymer (MLO) [20], and embedded wafer level ball grid array (eWLB) [14]. Its main advantage is that the 1st-level embedded subarray tiles can be duplicated to form large arrays, but with challenges of system complexity and excessive heat dissipation. In 2014-2018, IBM developed a 94 GHz four-IC phased-array tile with 8×8 dual-polarized antennas embedded in a MLO substrate, with four SiGe transceiver ICs flip-chip attached to the package [18], as Fig. 2.1(b) shows. The required IC area is almost identical to that needed for a 4×4 antenna subarray with 0.5λ spacing. Nonetheless, the scanning range of the array is limited to $\pm 30°$ due to constraints in the manufacturing process for antenna variations.

To further eliminate the power and RF distribution loss associated with the antenna-IC transition and distribution network, Antenna-on-Chip (AoC) phased arrays have been proposed. This technology involves embedding wafer-scale arrays on a single die, where each element is directly matched to the IC. This approach is scalable to a large number of elements, but power and RF distribution loss present significant design challenges. The antennas used in

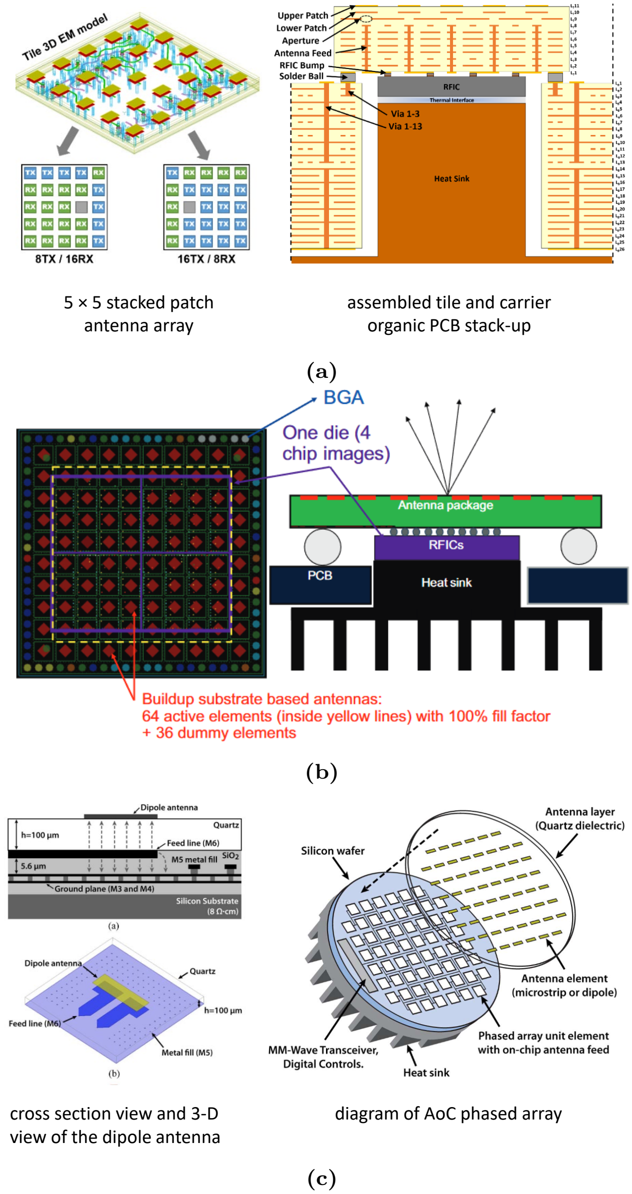

Figure 2.1: Examples of the W-/D-band state-of-art PAAs: (a) 384-element, 16-tile PA at 90 GHz and its Antenna-on-PCB section with 34 dBm EIRP [17]; (b) 64-element PA at 94 GHz and its AiP section [18]; (c) 16-element PA at 110 GHz and its AoC diagram [11].

such systems are expected to have an efficiency of at least 50% to be competitive with other packaging techniques. In 2013, researchers at UCSD built a 4×4 on-chip phased array (PAA) using the SiGe BiCMOS process [11], as illustrated in Fig. 2.1(c). The PAA achieved approximately 45% efficiency and a scanning range of $\pm 30°$. This design has the potential to be scaled up to 32–64 elements on a single chip. However, despite the high integration and the advantages of employing commercial semiconductor processes, on-chip PAAs still face challenges, such as a relatively narrow bandwidth ($\leq 10\%$), low radiation efficiency, and limited beam-steering range, primarily due to high material loss.

2.2 Non-conventional PAAs

The-above mentioned challenges steer research towards non-conventional PAA that can provide relatively high electrical performance with a simple design. One approach is to employ 2-D beam-steerable reconfigurable reflectarrays, where fast phase control can be realized by phase-shifting components integrated with radiating elements [21], [22]. For example, *Pan. et. al* proposed an on-chip reflectarray with active elements in GaAs process. In this work, a 1-bit P-I-N diode is connected to the patch antenna. Hence, the array structure is rather simple with 16×16 elements. However, the narrow bandwidth ($\leq 5\%$) and moderate scan capability ($\leq 20°$) are featured due to the limited degree of design freedom in GaAs substrate and the low-bit phase control scheme limited by element size [21]). Other beam-steerable array antennas use quasi-optical structures, e.g., Luneburg lens [23], [24], to extend the scan range, but at the cost of bulky design. Another wideband solution is dielectric rod arrays with liquid crystal-based phase control [25]. This technology offers low loss in the mmWave regime with continuous tunability and can be readily integrated into dielectric waveguides. However, one drawback is a relatively small beam-steering range and complicated assembly.

2.3 Fully-metal array antennas

To minimize material loss and reach higher radiation efficiency, full-metal array antenna designs have been investigated at W-/D-band [26]–[31]. Thanks to high-precision CNC-milling and silicon micro-machining manufacturing techniques, hollow waveguide (WG) type antennas have much higher efficiency ($>$ 50%) [28], [32] than printed antennas in substrate, but are less versatile in terms of beam-forming capabilities. The reason is that these metal antennas usually require dedicated waveguide-to-IC (WG-to-IC) transitions that are typically lossy and occupy much space. Recent developments in silicon micromachining have demonstrated even higher efficiencies ($>$70%) thanks to their nanometer surface roughness [29], [30]. It's worth mentioning that the leaky waveguide array proposed in [30] is fed by an quasi-optical radial waveguide instead of corporate feeding network, contributing to a low-profile ($\leq 0.78\lambda$) and compact array architecture. However, most reported arrays have been designed for fixed-beam scenarios, or as frequency beam-steering arrays, while the latter is not practical for telecommunication applications [30], [31].

2.4 Summary

Table 2.1 summarizes the beam-steering characteristics of the previously reported W-/D-band array antennas implemented in different technologies. Compared to AoC, AiP solutions, full-metal array elements are promising candidates for beam-steerable implementations in terms of the high radiation efficiency and wide-band performances. At the same time, non-traditional PAAs with hybrid phase control, e.g. the combination of QO feeding network and phase shifters allow a relatively simple array architecture, suitable for designing large-scale beam-steerable arrays at W-/D-bands.

Table 2.1: Performances of W-band beam-steerable antennas

Antenna/array type		Technology	Number of elements	Element spacing ($\times\lambda_0$)	f0, FBW (GHz, %)	Efficiency (%)	Scan range ($\pm^\circ$ in E-/H-plane)
[18]	patch antenna PA [1] (2-D electronic scan)	AiP	64 [2]	0.5	94, 5	N/A	30, 30
[17]	stacked patch antenna PA(2-D electronic scan)	antenna on PCB	384 [3]	0.63	90, 22	87	20, 20
[11]	mictrostrip/dipole PA (2-D electronic scan)	AoC	4×4	0.5	111, 5	45	30, 30
[25]	Dielectric rod (1-D electronic scan)	Milled Rexolite assembly	1×4	0.86	92.5, 38	N/A	-25 to 15 [4]
[21]	reconfigurable reflectarray (2-D electronic scan)	AoC (1-bit GaAs pin-diode control)	16×16	0.64, 0.54	96, 4	N/A	10, 10 [4]
[24]	Luneburg antenna (feed switch)	Lens fed by horn array	lens diameter=25 mm		77, 84	N/A	30, 30 [6]
[30]	planar leaky waveguide (1-D frequency scan)	Si Micromachining (gold)	$24\times24\times0.9$ mm^3 [7]		260, 31	76 [M arr]	-75 to -30 [f.s.]
[26]	dipole	Micromachined copper	16×16	0.59	142, 30	99 [r]	N/A
[28]	slot waveguide	diffusion bonding, copper	64×64	0.86	120, 12	50	N/A

[1] Phased array; [2] 64 embedded elements out of 100; [3] 16TX/8RX×16 tiles; [4] E-plane at 85 GHz; [5] at 96 GHz; [6] increment 7.5°; [r] radiation efficiency; [7] array size with quasi-optical feed; [f.s.] frequency scan; [M] Measured; [arr] full array.

CHAPTER 3

Array Antenna Unit Cell and Linear Array Antenna

A new antenna element type based on the open-ended ridge gap waveguide (RGW) operating at 100 GHz is proposed to overcome critical design challenges and physical space limitations in arrays with electronic beam-steering capabilities. Starting from a traditional ridge waveguide (WG) array element, a set of WG and RGW antennas with various inter-element decoupling features are designed and cross-compared in an infinite array environment. The chosen RGW element design is demonstrated in an experimental linear array to validate its design concept and performance.

3.1 Open-ended ridge and ridge gap waveguide (WG/RGW) radiating elements in an infinite array environment

Following considerations in Ch. 2, fully-metal open-ended WG elements are selected as the starting point of our design. At high mm-wave frequencies, traditional WGs' hollow metal designs are rare due to the increased manufacturing complexity. On the other hand, the relatively new gap waveguide

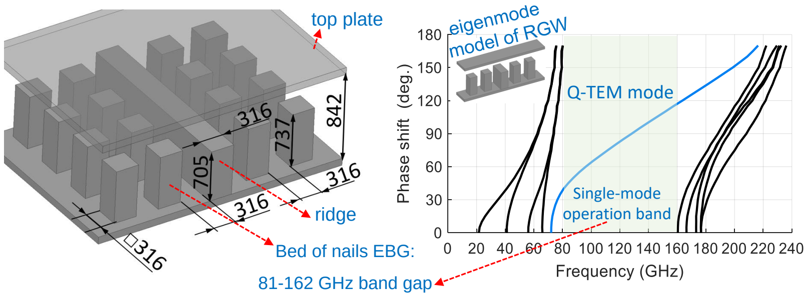

Figure 3.1: An initial RGW structure with design dimensions (in μm) and its dispersion diagram.

technology [33], realizing contactless WGs in a bed of nails, can be effectively utilized to resolve these problems. Fig. 3.1 demonstrates a geometry of the initial RGW structure used in this study, and its dispersion diagram simulated in eigenmode in Ansys HFSS. Two rows of pins are employed at each side of the central ridge, which is proved to prevent any unwanted mm-wave energy leakage in its eigenmode simulation. As seen in the RGW dispersion diagram (for a single-period pin structure) [34], a single quasi-TEM mode operation regime is realized in the (80–160) GHz range. At the same time, the RGW can operate above 82 GHz (the weak-dispersion region).

In the following discussions, all PAA radiating elements are designed using open-ended ridge WG and RGW structures. We evaluate and compare the performance of various WG and RGW array elements by adding different decoupling structures in the array aperture. These additions suppress the inter-element electromagnetic fields coupling and extend the achievable beam-steering range.

Elements in the triangular array lattice

In the rectangular grid phased arrays, as shwon in Fig. 3.2(a), the inter-element spacing within $0.5\lambda_h$ (λ_h is the free-space wavelength corresponding to the highest design frequency f_h) is required to avoid radiating grating lobes [6]. Alternatively, adopting triangular grid arrays as shown in Fig. 3.2(b), will relax this requirement with $\geq 0.5\lambda_h$ inter-element spacing [6]. The larger inter-element-spacing is especially beneficial for WG's H-plane spacing / size, which lowers the WG cut-off frequency and increases the available physical space for active electronics integration. A triangular array lattice ($tan\gamma = 2b/a$) is therefore chosen for all the following WG and RGW PAA designs, where the inter-element spacing values are chosen as $0.5\lambda_0$ and $0.6\lambda_0$ in the E- and H-plane, respectively.

The initial design of the open-ended WG antenna array element and the array lattice view are shown in Fig. 3.2(c). A single ridge is adopted inside the WG structure to lower the cut-off frequency of its fundamental mode, thus providing a wideband low-dispersive operation [35]. The ridge height is reduced in two-step towards the aperture, thus improving a wideband impedance matching with the free space. Similarly, the RGW element topology and its view in the array lattice is depicted in Fig. 3.2(d). The main advantage of the RGW design is its intrinsically contactless structure between top and bottom metal plates, which thereby allows for low-cost manufacturing, especially at high millimeter wave frequencies [33]. Also, the gap provides the desired extra space (around 100 μm along y-axis) for ICs and WG-to-IC transition structures. The RGW unit cell sizes are the same as for the ridge WG element. The stepped ridge and the shifted pins near the aperture area are customized to improve the impedance matching, which will be addressed in details at the end of the section.

It has been shown that open-ended WG array antennas have relatively strong antenna element mutual coupling effects [36], [37]. This can be a limiting factor of the bandwidth and scan range, where the latter often results in scan-blindness. This problem can be successfully overcome by adding grooves between the radiating WG elements [38]. These grooves operate as a soft surface, and hence, stop the electromagnetic waves propagation above the array aperture, thus effectively decoupling the array elements. To study this approach, we consider two additional variations of the elements: the WG/RGW element with only E-plane grooves as Fig. 3.3(a), 3.3(b) show, and the WG/RGW element with both E- and H-plane grooves in Fig. 3.3(c), 3.3(d). Furthermore, the last variation is adding a bed of pins protruding over the RGW element aperture, as Fig. 3.3(e) shows. Although these pins are frequently utilized to mitigate mutual coupling in wide-angle scanning printed PAAs [39], they are seldom employed over WG PAA apertures due to the thin E-plane walls, and their effects on WG elements remain untested. The design parameters of the WG and RGW array elements are

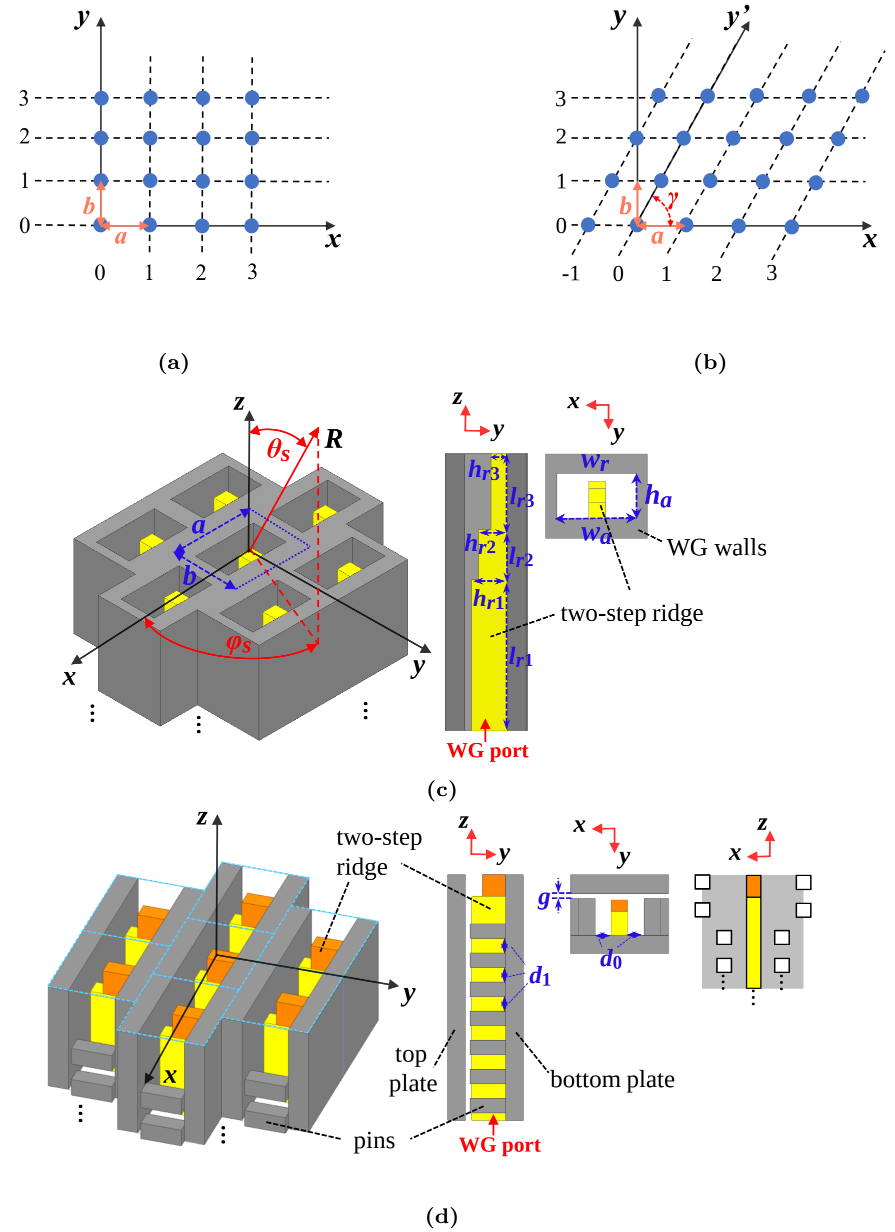

Figure 3.2: Considered rray configurations of (a) the rectangular lattice and (b) the triangular lattice; (c) the open-ended ridge WG, and (d) RGW topologies and the elements in triangular lattice.

shown in Table. 3.1.

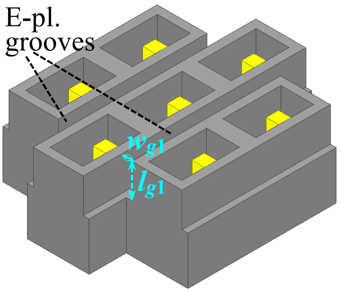

(a) WG + E-pl. grooves

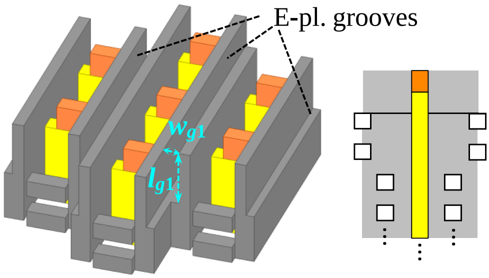

(b) RGW + E-pl. grooves

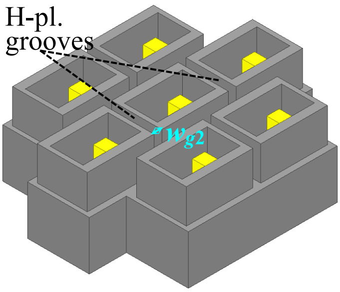

(c) WG + E- & H-pl. grooves

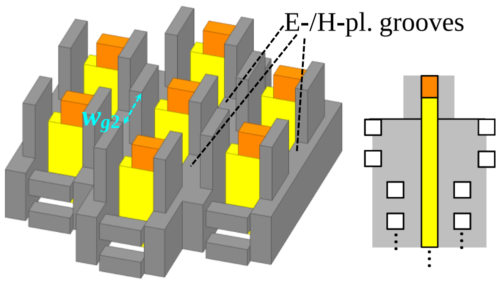

(d) RGW + E- & H-pl. grooves

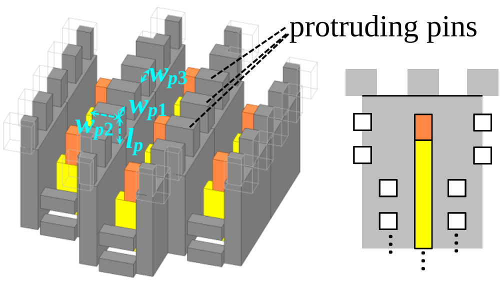

(e) RGW + protruding pins (the pins in the adjacent array area are shown as transparent)

Figure 3.3: WG and RGW array elements with various decoupling structures.

	a	b	w_r	h_{r1}				
	1896	1576	316	705				
WGs	w_a	h_a	l_{r1}	l_{r2}	l_{r3}	h_{r2}	h_{r3}	
	148	742	3000	980	1510	550	320	
	w_{g1}	w_{g2}	l_{g1}					
	300	200	870					
RGWs	d_0	d_1	g	l_{r1}	l_{r2}	l_{r3}	h_{r2}	h_{r3}
	316	316	105	3690	1170	466	705	480
	w_{g1}	w_{g2}	l_{g1}	w_{p1}	w_{p2}	w_{p3}	l_{p1}	
	300	1000	1060	600	400	548	650	

Table 3.1: Geometrical parameters of the WG and RGW designs illustrated in Fig. 3.2, 3.3. (unit: μm)

Beam-steering range cross-comparison

To characterize the array antenna element beam-steering performance in large finite array configurations, we have employed a full-wave simulation model of the array unit cell (UC). This UC has sidewall periodic boundary conditions in the triangular array lattice and a Floquet port is empolyed above the element aperture. The analysis was performed in the Ansys HFSS environment. The central design frequency is $f_0 = 95$ GHz. All the considered element designs have been optimized to reach the largest beam-steering angle (θ_{max}) through the criterion of $|\Gamma| \leq -10$ dB over the 20% relative bandwidth (BW) in 85–105 GHz. The magnitude of the scan reflection coefficient ($|\Gamma|$) for the beam-steering in the E- and H-planes is shown in Fig. 3.4.

The initial results for the ridge WG/RGW element configuration are presented in Fig. 3.4(a), 3.4(b). The black dashed line indicates the grating lobe-free border in the E-plane, where no grating lobes can exist in the H-plane within the studied frequency-scan angle range due to the triangular lattice. The impedance matching deteriorates as the scanning angle and bandwidth increase. The red dash-dotted lines illustrate the exemplified targeted BW goal of 20% ($|\Gamma| \leq -10$ dB). In the E-plane, both WG and RGW elements achieve a θ_{max} of 37°. However, in the H-plane, the 20% BW goals are attained for beam-steering up to 17° and 32° for WG and RGW, respectively. In comparison, RGW demonstrates a clear advantage in terms of wide-band and wide-scan characteristics.

The beam-steering performance of the ridge WG/RGW UCs with only E-plane grooves and with both E- and H-plane grooves are demonstrated in Fig. 3.4(c) - 3.4(f). The width and depth values of the grooves were optimized to improve the active $|\Gamma|$. When the E-plane grooves are added, the UCs demonstrates a significantly larger bandwidth for the broadside beam in both E- and H-planes. Although the θ_{max} in the E-planes for WG/RGW remain the same, the θ_{max} in the H-planes improve to 27° and 39°, respectively (see Fig. 3.4(c), 3.4(d)). However, the appearance of scan-blindness phenomena in the H-plane (upper right area of the plot) is observed, which is associated with the mutual coupling effects in the triangular grid as caused by the E-plane grooves. We proceed to analyze the results of the UCs with E- and H-plane grooves, as shown in Fig. 3.4(e), 3.4(f). The beam-steering performance is further improved compared to the previously described configurations. For WG UCs, the θ_{max} reach 42° and 26° for E- and H-planes, respectively, where scan blindness is still affecting the H-plane scan ability. On the other hand, RGW UCs with E- and H-plane grooves achieve wide-band performance with θ_{max} greater than 50°. The impedance matching covers almost 60° in 20% BW up to the grating lobe border in the E-plane, while the scan blindness in the H-plane is largely mitigated. Finally, we present the results of RGW UCs with protruding pins over the aperture, as depicted in Fig. 3.4(g). Compared to RGW with E- and H-plane grooves, the primary improvement is observed in the H-plane, as the scanning range reaches 60° in 20% BW. However, severe scan blindness in the E-plane at high frequencies and the bottom limit of the pins' bandgap at low frequencies significantly affect the BW. The scan range in both planes can be further improved only if the requirement of BW becomes less strict. To further understand how the beam-steering performance is affected by various RGW element aperture modifications, these results are discussed in connection with the post-processed mutual coupling coefficients in the following subsection.

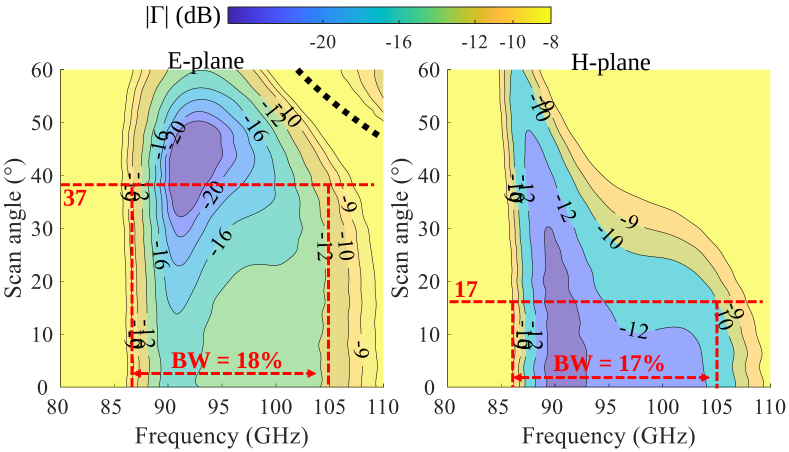

(a) WG

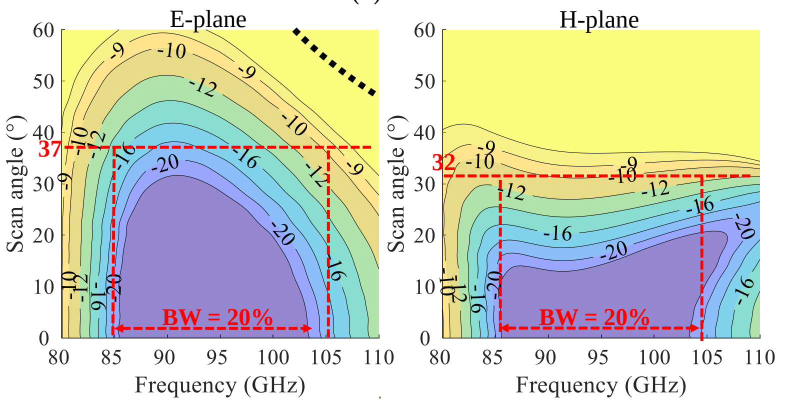

(b) RGW

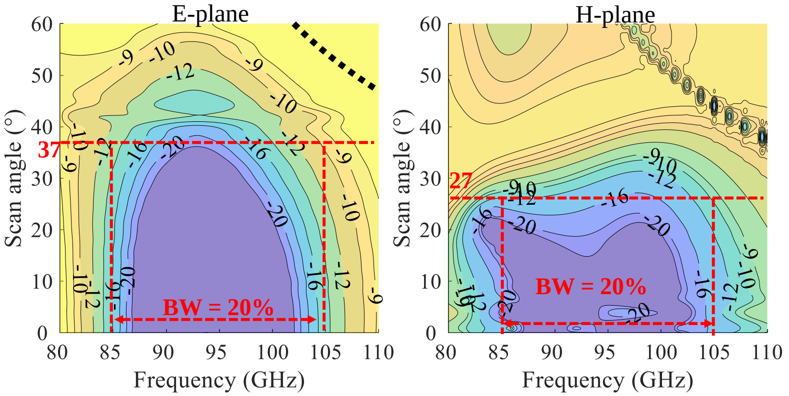

(c) WG with E-plane grooves

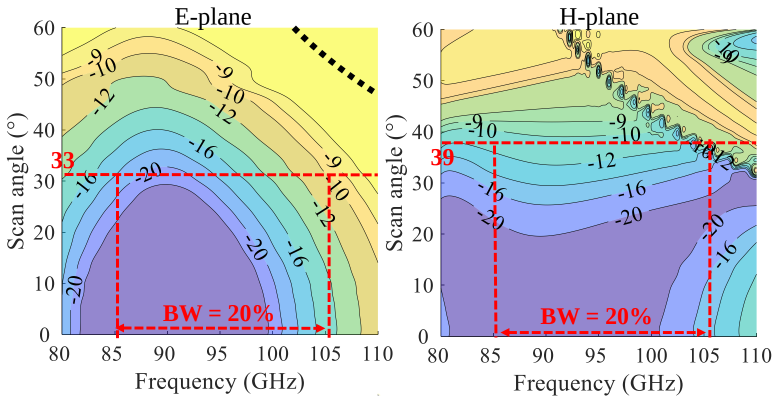

(d) RGW with E-plane grooves

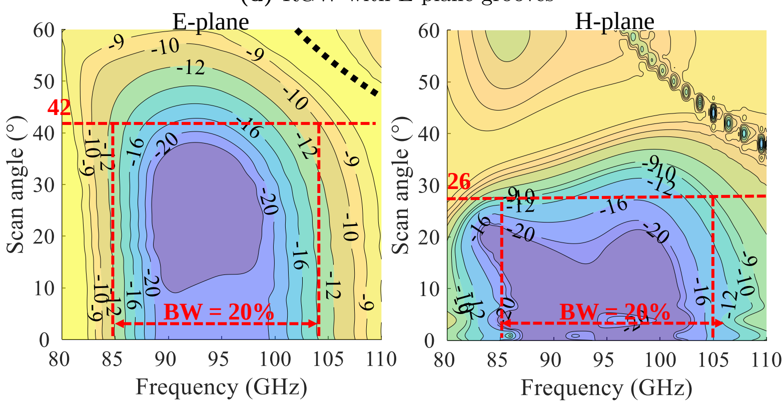

(e) WG with E-/H-plane grooves

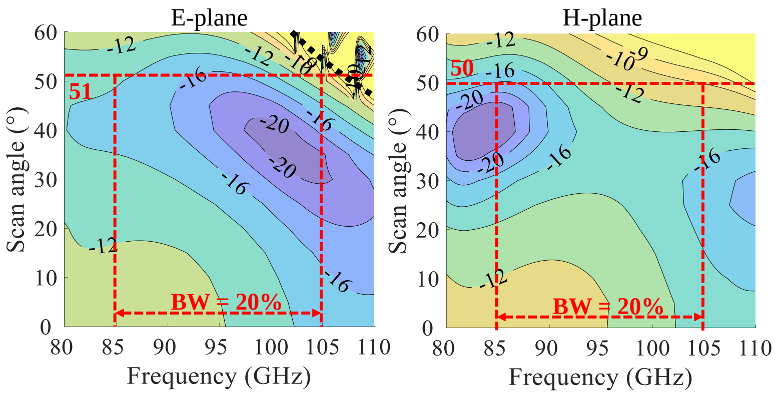

(f) RGW with E-/H-plane grooves

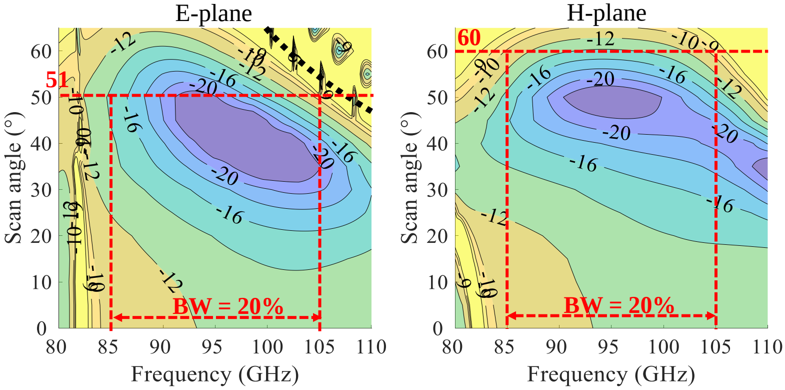

(g) RGW with protruding pins (the parts of the adjacent elements are shown semi-transparent)

Figure 3.4: Simulated scan reflection coefficient (Γ) contour plots for the various WG and RGW UCs of the 2-D infinite array.

Antenna elements mutual coupling effects

$$S_{ij} = \frac{1}{4\pi^2}\int_{-\pi}^{\pi}\int_{-\pi}^{\pi}\Gamma\left(\psi_x,\psi'_y\right)\exp\left[j\left(p\psi_x+q\psi'_y\right)\right]d\psi_x d\psi'_y \tag{3.1}$$

The array mutual coupling coefficients between the reference $(0,0)$- and (i,j)-element (S_{ij}) can be calculated using the 2-D Fourier series expansion of Γ, with S_{ij} representing the (i,j)-th Fourier coefficient in the $(\Psi_x, \Psi_{y'})$ phase space as depicted in Eq. 3.1 [36], [40], [41], where Ψ_x and $\Psi_{y'}$ are the phase differences between adjacent elements along x- and y'-axis in Fig. 3.2(b), i.e., $\Psi_x = 2\pi au/\lambda$, $\Psi_{y'} = 2\pi bv/\lambda + \Psi_x/2$.

Here, u and v are the scan directions in u,v-coordinates ($u = sin\theta_s cos\phi_s$, $v = sin\theta_s sin\phi_s$). Note that $\Psi_x, \Psi_{y'} \in [-\pi,\pi]$ that in general includes the invisible region of the (u,v) space. To consider both accuracy and time-efficiency, the resolution of $\Delta\Psi_x = \Delta\Psi_{y'} = 6°$ was used in numerical integration in Eq. 3.1. The results of UCs with the best performances are cross-copared in Fig. 3.5: the WG and RGW with E- /H-plane grooves, and the RGW with protruding pins.

As Fig. 3.5(a), 3.5(b) show, when both the E- and H-plane grooves are added, the mutual coupling between elements are well-suppressed in both planes. For $i \le 5$, the $|S_{i0}|$ drops faster at higher frequencies for the WG element, but the RGW elements show rapid coupling suppression for $i \leq 3$ over the operational bandwidth. Overall, this results in the larger H-plane θ_{max} of the RGW element. The RGW element performance improves further as the protruding pins are applied over the aperture, shown in Fig. 3.5(c): the mutual coupling coefficients are very close to the grooved RGW element, but they decrease rapidly and continuously as element index increases over all frequencies.

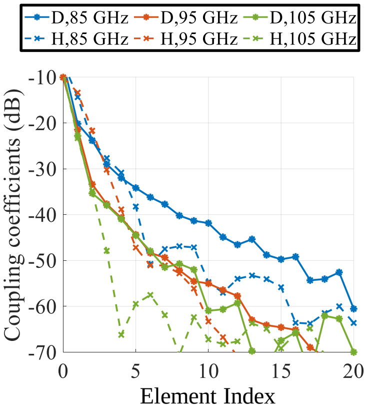

(a) WG with E-/H-pl. grooves

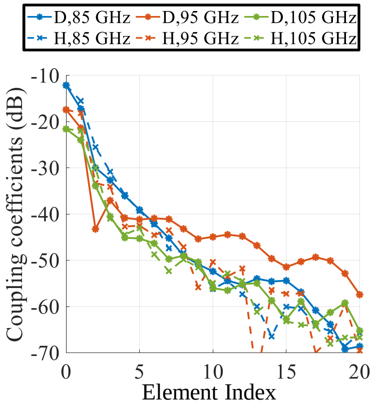

(b) RGW with E-/H-pl. grooves

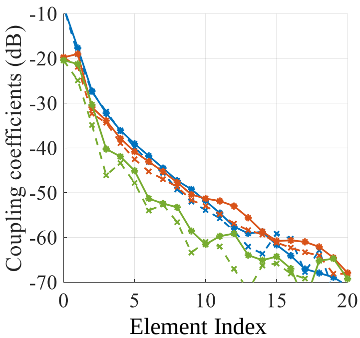

(c) RGW with protruding pins

Figure 3.5: Simulated coupling coefficients in the D- and H-plane for (a) the WG UC and the (b) RGW UC with E- / H-plane grooves, and (c) the RGW UCs with protruding pins in the infinite array environment. The elements numbering is given in Fig. 3.2(b).

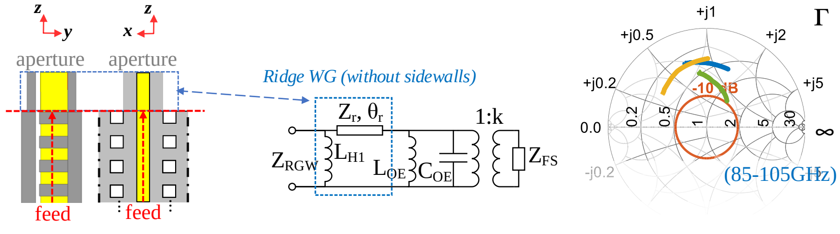

(a) No matching circuit

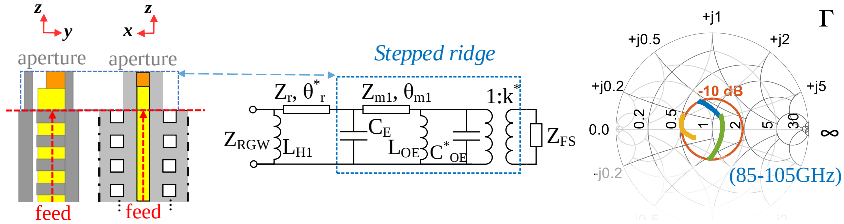

(b) Stepped ridge segment

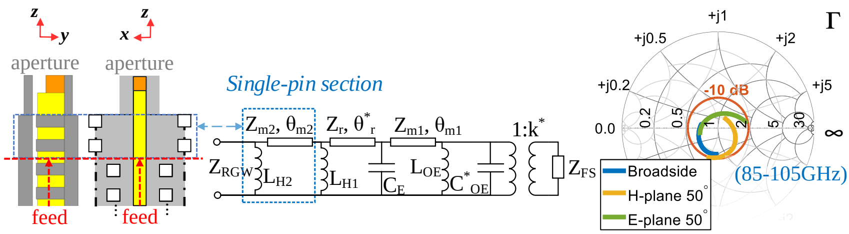

(c) Stepped ridge + single-pin section

Figure 3.6: Illustration of the impedance matching approach of the RGW element using the equivalent circuit representation. Open-ended RGW aperture parameters (beam-steering-dependent): Z_{FS} is the free-space impedance, $k^{(*)}$, $C_{OE}^{(*)}$, and L_{OE} are the equivalent transformer turn ratio, capacitance, and inductance with (*) and without the stepped ridge, respectively. Matching circuit parameters: $(Z_r, \theta_r^{(*)})$, (Z_{m1}, θ_{m1}), and (Z_{m2}, θ_{m2}) are the characteristic impedance and electrical length of the output ridge WG, stepped ridge, and single-pin segments; C_E and $L_{H1,2}$ are the equivalent capacitance and inductance of the E-plane ridge and H-plane pin sidewalls steps.

The proposed 2-D RGW element with E- /H-plane grooves

Considering the manufacturing complexity of the experimental array prototype, the RGW element with E- /H-plane grooves is chosen for performance demonstration. The RGW employs a single ridge with two rows of pins on each side. The RGW material is aluminum. In all simulations, the 0.5-μm Groisse surface roughness model is used.

The design of the proposed RGW element with grooves for a 2-D array was detailed in Fig. 3.3(d). As seen, the basic RGW is terminated in the open-ended manner that couples the propagating RGW wave to free space. A structure comprised of a stepped ridge segment and a single-pin RGW section realizes a broadband impedance match and is discussed below. In the H-plane, multiple array elements are manufactured on a common metal plate being separated by the pins. By stacking such sub-arrays in the E-plane (yz-plane) the full 2-D array is constructed. Active beam-steering electronics can be integrated in a top metal plate of each RGW and contactlessly coupled to the ridge employing an E-plane WG bifurcation [42]. That creates an important design advantage of such element at high mm-wave frequencies.

The element's design parameters have been optimized to achieve a maximum scanning range in the 20% relative bandwidth (85–105 GHz), as defined by the scan reflection coefficient $|\Gamma| \leq -10$ dB criterion. Fig. 3.6 consistently explains the impedance matching strategy utilizing a simplified equivalent circuit representation:

1. As seen in Fig. 3.6(a), the open-ended ridge WG fails to achieve the desired impedance match condition. This is largely due to the excessive shunting edge capacitance of the ridge C_{OE}.

2. The high-impedance (Z_{m1}) stepped ridge segment [Fig. 3.6(b)] realizes (i) a C_{OE} reduction to C^*_{OE} and (ii) an impedance transformation, while adding an equivalent E-plane ridge step capacitance C_E. As a result, the Γ curves are effectively shifted to the center of the Smith chart.

3. Finally, the low-impedance (Z_{m2}) single-pin section [Fig. 3.6(c)] locates all Γ curves well inside the -10-dB circle by providing a fine impedance transformation and adding an inductance L_{H2} of the H-plane sidewalls step.

The resulting beam-steering performance is demonstrated in Figs. 3.4(f).

For the 20% bandwidth the beam-steering range is $\pm 51°$ and $\pm 50°$ in the E-and H-plane, respectively. In the E-plane, at higher-frequencies, the scan range is limited by the grating-lobe border. Here, the element also experiences the scan blindness. On the other hand, in the H-plane, we observe no scan blindness. The elimination of this phenomenon is attributed to the E- and H-plane grooves that effectively create an aperture quasi-periodic electromagnetic soft surface [43] (see Fig. 3.3(d)). Within the beam-steering range, the simulated element radiation efficiency is $> 95\%$; the relative cross-polarization level is below -60 dB and -17 dB in the E- and H-plane, respectively.

3.2 Experimental study of the 1-D array

1-D array RGW element

A linear array design is of practical interest as a building block (sub-array) of the 2-D array antenna. Furthermore, mm-wave 1-D beam-steering arrays have found their application for the indoor communication [44] and automotive radar systems [45]. In these cases, the proposed open-ended RGW element concept can be readily utilized. The 1-D array and element structure is detailed in Fig. 3.7. As seen, the design has been, in general, inherited from the 2-D array element. The main difference is the two-groove structure formed in the E-plane. The resulting aperture electromagnetic soft surface predictably terminate and stop the leakage of the electrical currents to the exterior surfaces of the top and bottom metal plates. To be consistent with the previous 2-D array element design in the triangular lattice, we have used $d_H = 0.6\lambda_0$ for the 1-D array as well. The updated paratmeters are shown in Table. 3.2.

The 1-D element design has been optimized for the maximum scan range as the key design goal. A full-wave HFSS simulation model with the H-plane

1-D RGW	a	b	w_r	l_{r1}	l_{r2}	h_{r1}	h_{r2}
	1896	4542	316	4770	626	705	529
	w_{g1}	l_{g1}	w_{p1}	l_{p1}			
	370	1130	430	1850			

Table 3.2: Geometrical parameters of the 1-D RGW array illustrated in Fig. 3.7. (unit: μm)

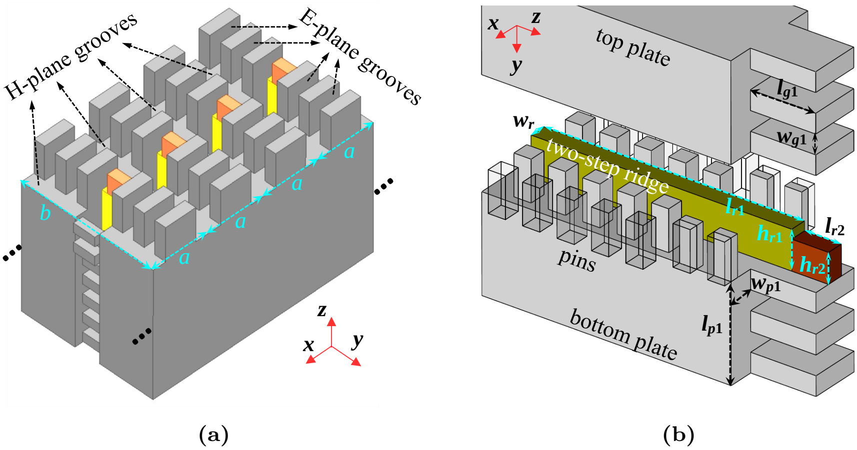

Figure 3.7: The proposed open-ended RGW element designs for a 1-D array: (a) close view of the array aperture; (b) explode view of the array element. The geometrical features of the adjacent elements in the H-plane are shown semi-transparent.

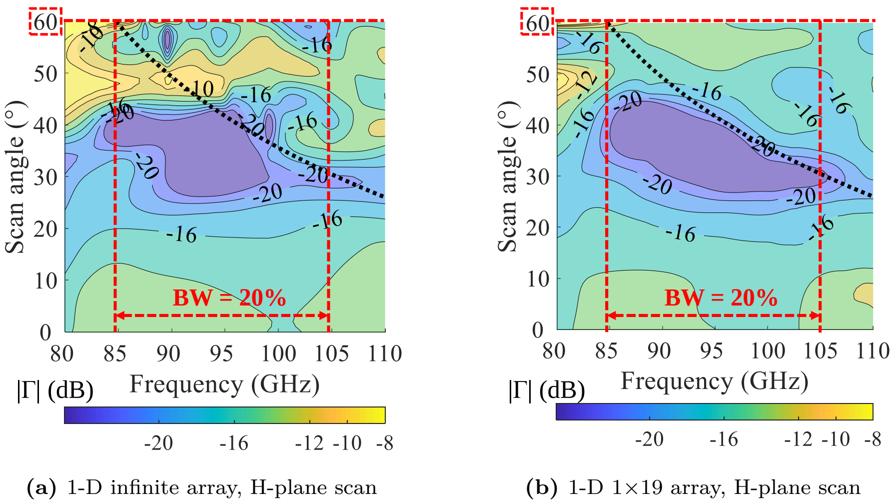

Figure 3.8: Simulated scan reflection coefficient (Γ) maps for the RGW element of the 1-D infinite, and 1-D finite (1×19) arrays.

PBC and perfect matched layers (along y- and z-axis) has been employed for this purpose. The simulated $|\Gamma|$ contour plot is presented in Fig. 3.8(a). The 1-D element demonstrates a wideband impedance matching performance with $|\Gamma| \leq -10$ dB. The grating-lobe border limits the scan range for some applications. However, this can be easily compensated by decreasing d_H.

Array design and measurement considerations

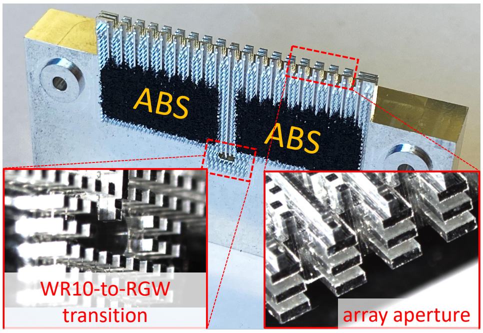

(a)

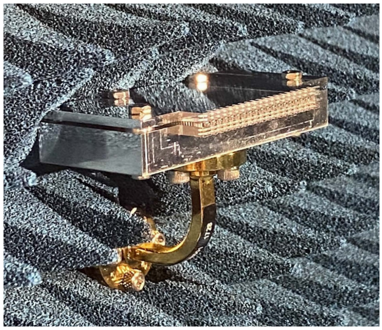

(b)

Figure 3.9: (a) Photograph of the manufactured 1-D 19-element open-ended RGW array (top plate removed) and (b) the antenna in the CATR measurement setup.

At this research stage, the first prototype of the 1-D array has been designed for the experimental characterization to verify the predicted RGW element scan performance, as well as to test its manufacturing and assembling tolerances. The 1×19 1-D array (Fig. 3.9) has been fabricated using a CNC milling process. This array size was found sufficient to reconstruct the 1-D infinite array environment as supported by results in Fig. 3.8(b) demonstrating simulated $|\Gamma|$ of the central array element. Since the standard WR-10 interface flange is much larger than d_H, measuring the full array S-matrix (to compute Γ) is practically impossible. Therefore, the beam-steering performance of the element was characterized through embedded element pattern (EEP) measurements [46]. To realize this, the central array element was excited using a WR10-to-RGW orthogonal transition (see Fig. 3.9(a)) [33], while all neighboring elements were terminated with matched loads (detailed in Paper *D*).

The loads were made of carbon-loaded absorbing foam (ABS) WAVASORB FS from Emerson & Cuming .

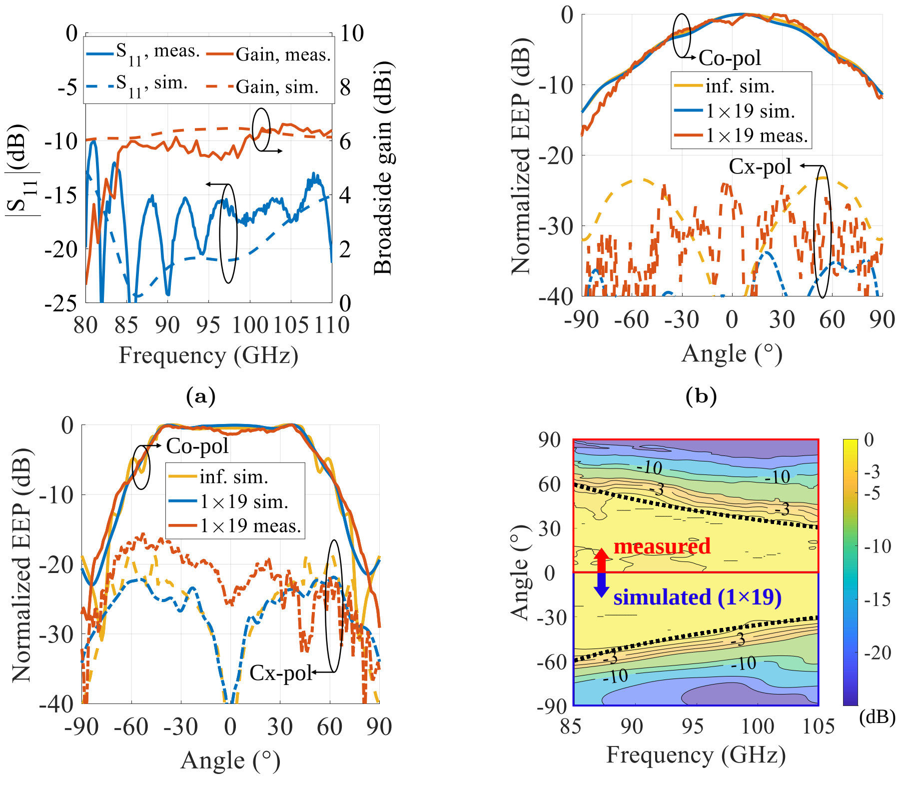

Figure 3.10: The simulated and measured performance of the 1-D array center RGW element: (a) reflection coefficient (S_{11}) and broadside realized gain; (b) E-plane and (c) H-plane normalized embedded element patterns (EEPs) at 95 GHz; (d) the H-plane co-polarized frequency-angle 2-D EEP maps (the dashed black lines indicate the grating-lobe border).

Beam-steering performance prediction

Element performance was measured at the WR-10 input flange in the compact antenna test range (CATR) setup of Chalmers THz antenna chamber [Fig. 3.9(b)]. The measured central element passive reflection coefficient (S_{11}) and the broadside realized element gain are given in Fig. 3.10(a) in comparison with the simulated curves. An additional insertion loss (~0.7 dB) of the WR10-to-RGW transition and an RGW feed line has been extracted from back-to-back structure measurements and subtracted from the measured gain results.

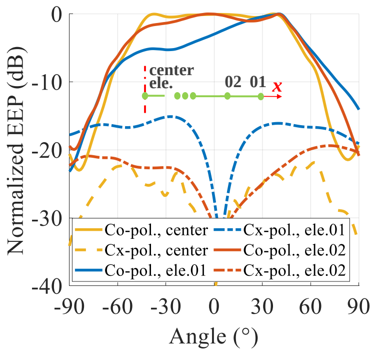

Figure 3.11: Simulated EEPs at 95 GHz for the different element positions in the 1×19 linear array.

Some frequency ripples are observed for both S_{11} and gain measured curves. These ripples are attributed to relatively high manufacturing errors ($\leq 20\ \mu m$) of the stepped ridge height in the transition and aperture areas. Moreover, the realized gain is affected by imperfect ABS loads performance (average reflection coefficient ~17 dB (detailed in Paper *D*). The experimental embedded element radiation efficiency was estimated to be $\geq 91\%$, considering simulated values of $\geq 97\%$ and an average measured gain loss of 0.3 dB compared to simulation. The simulated (for both the 1×19 array and the 1-D infinite array model) and measured normalized EEPs at 95 GHz are compared in Figs. 3.10(b), 3.10(c) for the E- and H-plane, respectively. A small (~1 dB) H-plane broadside dip, observed for the measured pattern, is due to the above-mentioned non-zero reflections in the ABS-terminated channels.

The measured cross-polarized EEP is slightly asymmetrical that is, likely attributed to the measurement setup as the WG transition and the bottom plate are quite bulky. Fig. 3.10(d) depicts the frequency-angle 2-D co-polarized EEP maps in the H-plane revealing a wide-angle flat-top EEP shape. Array edge effects have been studied in simulations and shown in Fig. 3.11, from which we can conclude that already for the second edge element the EEP shape in the $\pm 50°$ range deviates by less than 2 dB from the results in Fig. 3.10. Overall, the simulated and measured results in the 85–105 GHz range are in a very good agreement, verifying the expected wideband and wide-angle RGW element beam-steering performance with low sensitivity to manufacturing and assembling tolerances ($\pm 20\ \mu m$).

Table 3.3 summarizes the beam-steering performance of the previously reported mm-wave (100+ GHz) array elements implemented in different technologies. The proposed designs outperform the state-of-the-art W- and D-band antenna solutions based on AoC, AiP, and dielectric rod arrays [11], [17], [18], [25], as well as leaky-wave metal antennas [30], [31] in terms of wide-angle, wideband beam-steering capabilities with high radiation efficiency. The demonstrated 2-D array element performance has been, thus far, achieved for the open-ended ridge WG elements [37] and rectangular WG elements [47] only at much lower frequency bands (L- and X-bands), employing impedance-matching dielectric sheets and WG insets.

Table 3.3: Performance comparison of reported array antenna elements at mm-wave frequency bands.

Array element type		Implementation technology	Freq. range (GHz) ($\|\Gamma\| \leq -10$ dB)	Element size (λ_0^2)	Radiation efficiency (%)	Scan range / scan loss
[18]	Planar stacked patch	AiP	88-94, 7%	0.49×0.49	N/A	±32° (E/H-plane) / NA
[11]	Planar dif.-fed dipole	AoC (quartz)	108-114, 5%	0.5×0.5	45	±30° (E/H-plane) / ≤ 2.5 dB
[30]	Leaky-wave slot WG	Si micromachining (gold)	220-300, 30%	0.49×0.35	79 (full antenna)	–75° to –30° (E-plane) / NA
[25]	Dielectric rod	Milled Rexolite assembly	75-110, 38%	0.86×0.86	N/A	–25° to 15° (E-plane, 85 GHz) / ≤2.5 dB
This work	Open-ended RGW: **1-D**	Fully-metal (aluminum), contactless	85-105, 21%	1.37×0.6	≥ 91	±40° (H-plane) / ≤ 3 dB
	2-D		85-105, 21%	0.5×0.6	≥ 89	±51°/±50° (E/H-plane) / ≤2.5 dB

3.3 Conclusion

In this chapter, we proposed the open-ended ridge gap waveguide (RGW) antenna element concept for 1- and 2-D array configurations. This RGW element is easily manufacturable from two split blocks which can be thereafter assembled contactlessly. The latter provides that the element is suitable for the integration of active electronics inside its structure to enable electronic beam-steering at high mm-wave frequencies. The results of the infinite array simulation model have been verified through the experimental study of the 1-D array element. At W-band, the 2-D array element demonstrates a wide-band ($\geq 20\%$) and wide-angle ($\geq 50°$) beam-steering performance with high radiation efficiency ($\geq 89\%$, with 0.3 dB additional loss included).

As the final goals we focus on at the development of a 2-D array prototype as well as the integration of phase-shifting circuitry into the element's RGW. A quasi-optical feed architecture is being considered for efficient array elements excitation in the following chapter.

CHAPTER 4

Qausi-optical Feed Design Network and the Array Performance Analysis

In this section, a concept of the linear (sub-)array combining low-order (1-bit or 2-bit) phase-shifters (PS) and a spatial quasi-optical (QO) beam-forming network is proposed and demonstrated in gap waveguide technology. This active linear array concept realizes 1-D beam-steering performances and can be used as a building block of a 2-D PAA system. A system-level numerical analysis of the hybrid beam-forming linear (sub-)array antenna including the spatial QO beam-forming network is presented. This analysis is done by cascading the scattering parameters of the individual system components and applying optimal beam-forming coefficients to the array elements to obtain the beam-steered radiation patterns.

4.1 Operational principle and theoretical background

Given the increasing demand in millimeter-wave communication systems, phased array antennas (PAAs) that offer high gain and dynamic beam control have

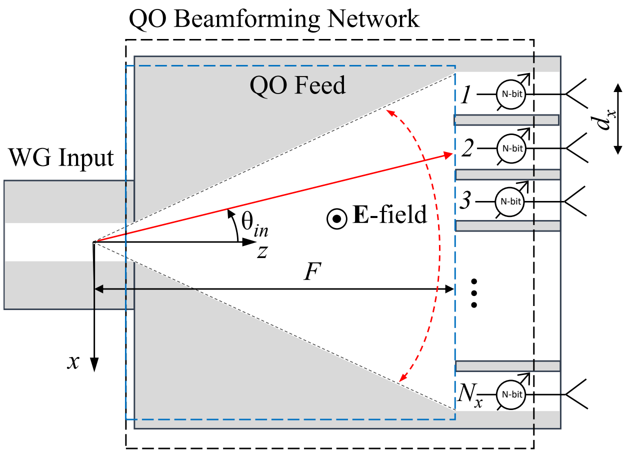

Figure 4.1: A linear (sub-)array antenna with a QO beam-forming network comprising a QO feed and N-bit integrated PSs.

been extensively explored [2]. These PAAs can mitigate the high free-space path loss and power-generation limitations inherent at these frequencies. As discussed in Ch. 2, conventional PAAs encounter notable difficulties at frequencies above 100 GHz, primarily due to the large dissipative losses in antenna, conductor and dielectric materials, and the difficulty to integrate the ICs within the small inter-element spacing.

Recently, researchers have proposed energy-efficient, non-conventional PAA designs that utilize low-order (1- and 2-bit) phase control to facilitate beam-steering at frequencies below 30 GHz [48]–[51]. This strategy shows particular promise for higher frequencies. In fact, at high mm-wave frequencies, contemporary monolithic digital PSs typically exhibit an insertion loss of ∼2.53 dB per bit [52]. At the same, the PAA gain loss due to 1-bit phase quantization errors is ∼3.8 dB, and ∼1 dB for 2-bit quantization [50]. Thus, at W-band, 1-bit and 2-bit based architectures demonstrate comparable antenna gain and efficiency. However, 1-bit PAAs boast a more straightforward and compact design. A significant challenge of such designs is the phase quantization sidelobes that emerge due to periodic PAA aperture phase errors [6]. These sidelobes are particularly severe for 1-bit PAAs. Due to the 1-/2-bit phase quantization, these designs require a specific nonlinear initial phase distribution at the array ports (demonstrated in details in Sec. 4.3). This can be achieved through a quasi-optical feeding structure, as illustrated in Fig. 4.1. This approach can be considered a phase error randomization method that can perform close to the phase-added method [53].

To demonstrate this concept at high mmW frequencies with lower insertion loss, this initial excitation can be implemented by feeding the sub-array through a tapered waveguide section with the focal ratio $F/(N_x d_x)$ [54], where F is the focal length, as depicted in Fig. 4.1. The proposed hybrid (QO feed + PSs) beam-forming network is connected to an array of $N_x = 20$ radiating antenna elements excited through a planar quasi-optical (QO) feed. In addition, each element has its own integrated PS to support beam-steering. The QO feed represents a low-loss free-space feeding alternative to conventional corporate feed networks for mm-wave large-scale arrays ($N_x > 10$). The PS's states differ from element to element between 0 and 180° (or 0, 90, 180 and 270°) values depending on a beam-steering direction. The main advantage of this architecture is its highly-integrated and simple design, which can be manufactured in a standard waveguide technology. Moreover, as opposed to corporate feed PAAs, such an architecture conveniently realizes the required nonlinear initial phase distribution for high N_x.

4.2 Design goals

In previous chapters, we realized an RGW antenna element and a linear array design that can be co-integrated with PSs for electronic beam-steering PAAs as opposed to most reported GWG antennas that are fixed-beam. The on-chip 1- and 2-bit PSs can be designed in *WIN PIH1-10* GaAs process that is suitable for mmWave applications and which Chalmers has access to via the WIN & Universities collaboration programe. And a contactless monolithic microwave integrated circuits (MMIC) -to-RGW transition is customized to fit the low-bit PS into each RGW antenna element. The PSs with the transition are studied in another collaborated work [55]. In this chapter, the results of the PSs and the transitions are used for the numerical analysis of the QO + antenna array system.

In this way, the GWG QO feed can be used to realize the desired initial phase distribution. The final design goal for the proposed QO feed + PSs beam-forming network is to reach the maximum system available gain and minimum side lobe levels (SLLs) over the operational frequency band of 85 -105 GHz and in 2-D scan range of $\pm 50°$. In this Licentiate thesis, we focus on 1-D scan range.

To realize the QO feed design fulfilling the above system requirements, we need to consider the following critical aspects and questions:

1. What is the optimum initial phase distribution of the QO feed for the minimum sidelobe level (SLL) of the 1-D array?
2. What is the suitable feed design implementation of the QO feed that can overcome manufacturing complexities at these high frequencies?
3. What are the final realized gain and SLLs for the proposed implemented total array + PS + QO feed system?

The below-described design methodology of the QO feed addressed these questions.

4.3 Design methodology

In this section, we will discuss the process of designing the QO feed, from the initial numerical analysis to its implementation in gap waveguide technology.

First order design approach and initial design parameters

We aim to design a linear array with the minimized sidelobe levels (SLL) through optimum quasi-randomization of the phase errors in the elements excitation to approach the desired linear phase excitation as close as possible. An analytical expression for the optimum focal ratio of the QO feed has been derived to establish the relationships between the key design parameters of F, N_x, d_x. We consider a linear array of N_x elements (see Fig. 4.1). Neglecting the array edge truncation effects, the array far field can be represented as

$$\mathbf{E}_{FF}(\theta) = \mathbf{F}_e(\theta) \sum_{i=1}^{N_x} A_i \mathrm{exp}(j[\Phi_i + \varphi_i^{\Sigma}]), \tag{4.1}$$

where $\mathbf{F}_e$ is the embedded element pattern (where the azimuthal dependence is omitted); $\Phi_i = k_0 x_i \mathrm{sin}(\theta)$, $x_i = [i - (N_x + 1)/2]d_x$, $k_0 = 2\pi/\lambda_0$ is the wavenumber, λ_0 is the free-space wavelength; A_i and φ_i^{Σ} are the i-th element excitation amplitude and phase. The latter can be expressed through the output phase φ_i^{QO} at the reference plane and the 1-bit PS phase φ_i^{PS}:

$$\varphi_i^{\Sigma} = \varphi_i^{QO} + \varphi_i^{PS}. \tag{4.2}$$

On the other hand, $\varphi_i^{\Sigma} = \Phi_i^0 + \delta\varphi_i$, where $\Phi_i^0 = -k_0 x_i \sin(\theta_s)$ is an ideal element phase, θ_s is a beam-steering angle, $\delta\varphi_i$ is a phase quantization error. The excitation function of the QO feed is approximated by a cylindrical phase front emanating from its focal center at the distance F from the reference plane (see Fig. 4.1):

$$\varphi_i^{QO} = -k_0\big(\sqrt{x_i^2 + F^2} - F\big). \tag{4.3}$$

In Eq. (4.3), we assume the QO feed propagation constant equals k_0. At the same time, the amplitude distribution is modeled as the cosine-on-a-pedestal function [56] (with the taper parameter C), which was found to be a reasonable approximation for the QO feed with y-oriented E-field:

$$A_i = C + (1 - C)\cos\big(\pi x_i/(N_x d_x)\big). \tag{4.4}$$

Taking the describes 1-bit PS case as an example, the PSs' state switches between 0 and 180° values during beam-steering [57], and the far-field simulated results for the linear PAA can be computed from Eq. (4.1). The scattering matrix and the radiation patterns of the linear array results from Ch. 3 are used here for numerical models. The number of the antenna elements is $N_x = 20$ and the inter-element spacing is $d_x = 0.6\lambda_0$. The center embedded element pattern is used for the array + PS + QO feed system analysis. The linear array radiating element has been designed to enable grating lobe-free and impedance-matched beam-steering up to $|\theta_s| = 60°$. The amplitude taper has been computed as $-20\log(A(x_1))$.

The simulated SLL and system gain for different tapers at $f_0 = 95$ GHz are given in Fig. 4.2(a), where the QO feed focal ratio is varying with $F/(N_x d_x)$. The maximum SLL and mean SLL are computed for each θ_s and then averaged over the ±40° beam-steering range. As we can see, the mean SLL values are relatively invariant with focal ratio, and generally depend on N_x only. An important observation in Fig. 4.2(a) is that the maximum SLL curves demonstrate local minima around $F/(N_x d_x) = 1$. At the same time, the SLL improvement is more significant for the stronger tapered distributions, which

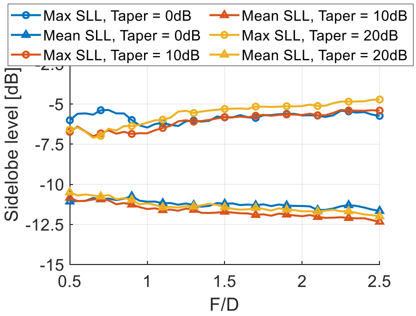

(a)

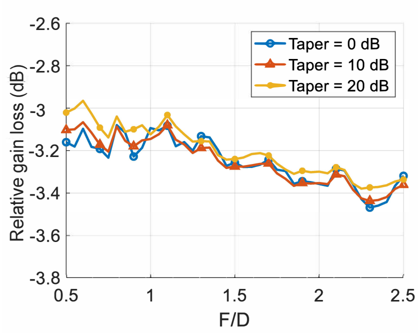

(b)

Figure 4.2: Averaged (over $|\theta_s| \leq 40^\circ$ beam-steering range) (a) SLL and (b) gain loss relative to the ideal phase control, where this loss is due to phase quantization errors at $f_0 = 95$ GHz with $N_x = 20$ and 1-bit PS.

is an expected result from the aperture antenna theory. If we consider the array factor (AF) using the summation factor in Eq. (4.1), the array gain loss due to the phase quantization errors of the 1-bit PS can be computed as $|\sum_{i=1}^{N_x} A_i|^2/\max(|AF(\theta)|^2)$. The averaged results are shown in Fig. 4.2(b). As seen, the gain degrades by 3–3.6 dB and is virtually independent from the taper values. It is an average gain loss associated with the quantization errors with the 1-bit PS case.

Hardware implementation of GWG QO feed

In Fig. 4.3, the QO feed design based on a radial (sectoral) groove gap waveguide (GGW) is considered, which interconnects an array of output ridge gap waveguide (RGW) channels with an RGW input. In this setup, the output channels are designed with the same dimensions as the RGW antenna elements. The proposed design concept can be visualized as a bed of nails forming an electromagnetic bandgap (EBG) surface. This EBG surface acts as the sidewalls of both the RGW and radial GGW. The QO feed comprises three main parts: (i) the input RGW with a transition to the GGW input; (ii) the linear tapering or the radial GGW; (iii) the array of the output RGWs with transitions to the radial GGW output. The inter-element spacing of the output array $d_x = 1.896\,\text{mm} = 0.6\lambda_0$, where λ_0 is the free-space wavelength at the central design frequency $f_0 = 95$ GHz. The targeted design bandwidth for all the system components is 85–105 GHz. The bed of nails used in the QO feed has the same dimensions with that in Ch. 3.

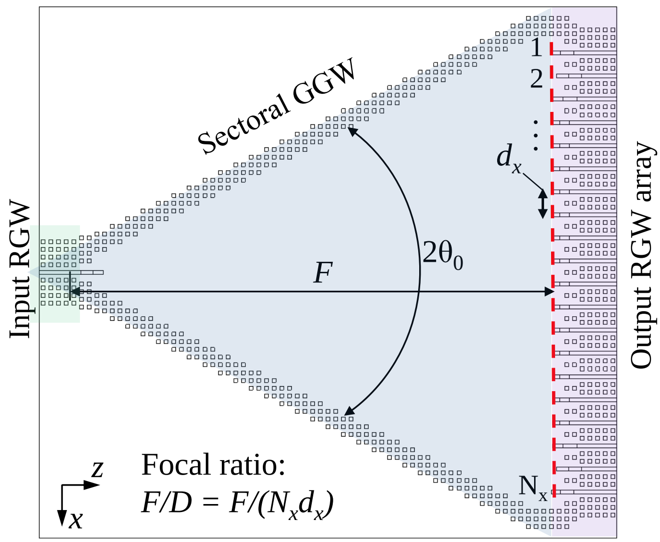

Figure 4.3: A proposed implementation of the QO feed in the GWG technology. The inset demonstrates the RGW structure. Its geometrical paramters are listed in Table. 4.1.

As discussed above, for PAAs with a low-order phase resolution (e.g., 1-bit) a crucial design parameter is the QO feed focal ratio $F/(N_x d_x)$. In this study, the focal ratio is chosen as 1.0, which corresponds to the GGW sidewall tapering angle of 26.5°. This configuration allows for the widening of the GGW such that for every two EBG periods ($P_{EBG} = 0.632$ mm) along the z-axis, the sidewall shifts by one period along the x-axis. It helps us to generate a more homogeneous field in the GGW area, which results in transmission coefficients that exhibit fewer ripples and show less variation over frequency.

Since the direct optimization of the QO feed with $N_x = 20$ represents an electrically large simulation problem, we have developed a decomposition modeling approach allowing a separate design of the input and output GGW-

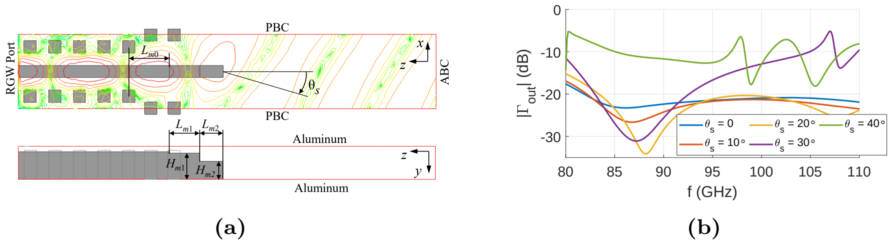

Figure 4.4: (a) The output RGW element in the infinite 1-D array environment. The overlapping E-field distribution (top plot) is given at 95 GHz and $\theta_s = 30°$. (b) Frequency dependencies of the output periodic element's active reflection coefficient for different scan angles θ_s. Design parameters are listed in Table. 4.1.

to-RGW transition structures. That will be detailed in the following subsections. For all simulation models, aluminum has been used with 0.5-μm surface roughness via Ansys HFSS Groisse model.

Impedance matching of the RGW output channels

The performance of the output RGW channels can be simulated using the reciprocity principle [36], by representing the channel as an element of an infinite transmitting 1-D array. Fig. 4.4(a) illustrates this simulation model with the assigned sidewall ($\pm x$-direction) periodic boundary conditions (PBC), absorbing boundary conditions (ABC) in front ($-z$-direction) of the element, and aluminum walls at $\pm y$-direction. Thus, optimizing element's active reflection coefficient Γ_{out} for a given scan angle θ_s results in the matched receiving of an incident wave from the $\theta_{in} = \theta_s$ direction (inside the QO feed), as depicted in Fig. 4.1. To provide optimal impedance matching, we have introduced a wideband matching circuit comprising a 2-step RGW impedance transformer and an EBG sidewalls transition from the 2- to a 1-pin configuration. Fig. 4.4(b) shows the final Γ_{out} for different θ_s after the full-wave model optimization in Ansys HFSS. As seen, the element is well-matched for $\theta_s \leq 30°$. When θ_s approaches 40°, the impedance matching significantly degrades, which resembles the scan blindness phenomenon in conventional 2-D arrays [36].

Input RGW-to-GGW transition

The input transition model has been developed to optimize input impedance matching and investigate the primary (illumination) field of the QO feed. Fig. 4.5 details three input configurations (*Input* 1–*Input* 3) based on this model. The model is surrounded by the ABC region in the xz-plane. These designs utilize the same structure of the wideband impedance-matching circuit (Fig. 4.4(a)) with different input ridge lengths. The RGW-to-GGW transition is created by an opening of the input RGW sidewalls, where every two row of pins are shifted by $1P_{EBG}$ alongside the tapering angle 26.5°. Specially, the second period applies a $2P_{EBG}$ shift. From the electromagnetic perspective, the input RGW-to-GGW transition can be seen as: (i) a transition from the input RGW to a stepped rectangular GGW; (ii) a transition from the stepped GGW to the radial (H-plane sectoral) GGW when the local transverse size of the GWG is much larger than $2P_{EBG}$. Thereby, a transverse structure of the primary field will be defined by an excited modal content of the radial GGW, which, in turn, depends on a modal content excited by the stepped GGW.

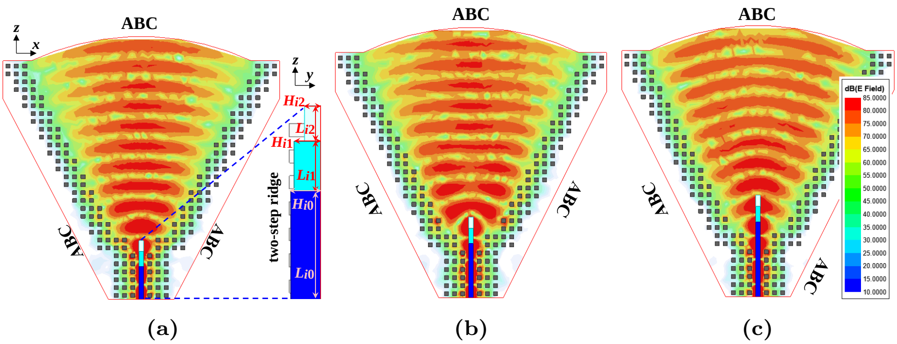

Figure 4.5: Different configurations of the QO feed input: (a) configuration *Input* 1; (b) configuration *Input* 2; (c) configuration *Input* 3. The instantaneous E-field distributions are given at 95 GHz. Geometrical parameters are illustrated in Table. 4.1.

As Fig. 4.5 shows, the total length of the input stepped ridge is increased by a quarter wavelength in each configuration from *Input* 1 to *Input* 3. While the heights of the stepped ridges are modified to reach $\Gamma_{in} \leq -10$ dB impedance matched over the target bandwidth. In the transition areas of *Input* 1 to

Input 3 (see Table. 4.1), the electromagnetic waves propagate in different modes as the radial shapes at the end of the ridge are different. This result in various dominant modes in the radial GGW parts. As *Input* 1 configuration excites mainly TE_{10} mode with respect to z-axis; and *Input* 2 configuration combines TE_{10} and TE_{30} modes; while *Input* 3 configuration is dominated by the TE_{30} mode. This behavior is observed in the instantaneous E-field within Ansys HFSS simulation models. In fact, the propagation modes in the radial GGW do not perfectly align with the performance predicted by Eq. (4.3) and (4.4) due to the presence of high-order modes. This discrepancy accounts for the changes in the taper distribution within the QO feed, even when the focal ratio is fixed.

QO feed	F/D	N_x	d_x	θ_0		
	1.0028	20	1896	26.5°		
output RGW	L_{m0}	L_{m1}	L_{m2}	H_{m1}	H_{m2}	
	1051	777	602	665	457	
input RGW						
# *Input* 1	L_{i0}	L_{i1}	L_{i2}	H_{i0}	H_{i1}	H_{i2}
	2638	1203	864	705	627	379
# *Input* 2	L_{i0}	L_{i1}	L_{i2}	H_{i0}	H_{i1}	H_{i2}
	4800	990	910	705	630	380
# *Input* 3	L_{i0}	L_{i1}	L_{i2}	H_{i0}	H_{i1}	H_{i2}
	5798	1203	856	705	627	379

Table 4.1: Parameters of the QO designs. (unit: μm)

Output amplitude and phase distribution control

To search the best performance for the GWG QO feed fulfilling the predicted array model with a SLL suppression, we have designed several QO feeds with different combinations of the input and output transitions. In all cases, the output configuration has 20 optimized RGW outputs. Two output configurations are considered and shown in Fig. 4.6, the configuration *Output* 1 applies $17P_{EBG}$-long straight GWG sidewalls (along z-axis) transiting from radial GWG QO to outputs, and the configuration *Output* 2 applies $7P_{EBG}$-long sidewalls.

Fig. 4.7 presents the results for different configurations including the instantaneous E-field distributions at $f_0 = 95$ GHz (input port excited), the

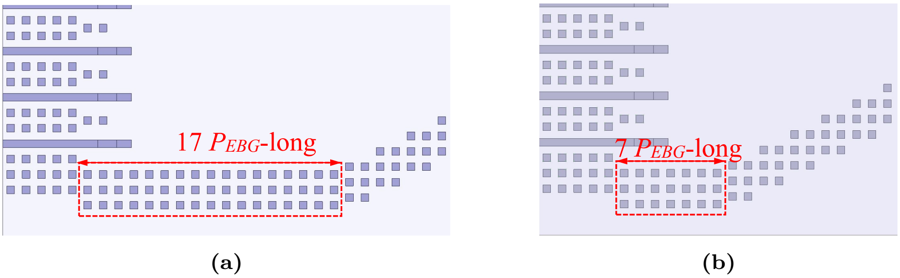

Figure 4.6: Different configurations of the QO feed output: (a) configuration *Output* 1; (b) configuration *Output* 2. $P_{EBG} = 316\mu m$, which stands for a period length of the EBG pins.

output amplitude and phase distributions, and the corresponding transmission coefficients over frequency. As Fig. 4.7(a), 4.7(b) and 4.7(c) show, the same output QO configurations with different input configurations from *Input* 1 to *Input* 3 demonstrate an reduced output amplitude taper from 7 to 0.9 dB in average; meanwhile, the phase distributions remain non-variant and are equivalent to Eq. (4.3) with the focal ratio around 1.1 to 1.3. As depicted in Fig. 4.5, the *Input* 1 to *Input* 3 excite different modes in the QO structure, which have similar impacts in QO configurations *Output* 1 & *Input* 1 to *Output* 1 & *Input* 3. In Fig. 4.7(a), the shortest ridge, *Input* 1, excites the dominant mode TE_{01}, along with other $TE_{0\delta}$ modes propagating in the QO feed. These modes are less variant over frequencies. In 4.7(b), as the ridge length increases, more higher-order modes are generated in the radial GWG, and they vary with frequencies. When the ridge length increases to that of configuration *Output* 1 & *Input* 3, the excited higher-order modes create a small amplitude taper of 4 dB on average, which is weakly dependent from frequencies with the maximum ripple in ±3 dB (85–105 GHz range).

To ensure optimal illumination to the output edge elements, the elongation length from the radial GWG to the output elements are modified to be $17P_{EBG}$ in length (see Fig. 4.7(c)). In comparison, configuration *Output* 2 with $7P_{EBG}$ elongation (see Fig. 4.7(d)) cannot realize efficient transmission to the edge elements and the transmission performance flatness over frequency is deteriorated due to significant field reflections from the extended corner regions. In all the considered cases, a simulated dissipative loss is below 0.5 dB.

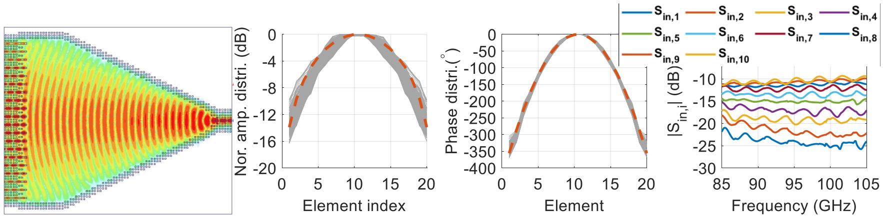

(a) *Output* 1 & *Input* 1

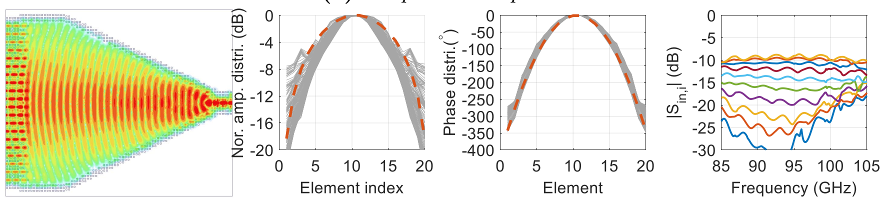

(b) *Output* 1 & *Input* 2

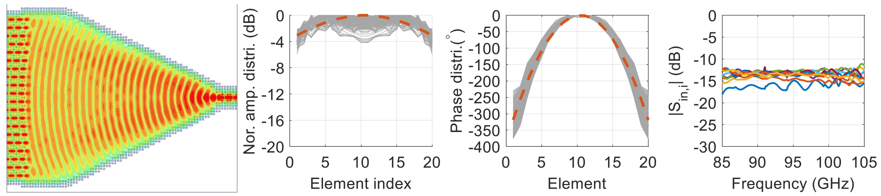

(c) *Output* 1 & *Input* 3

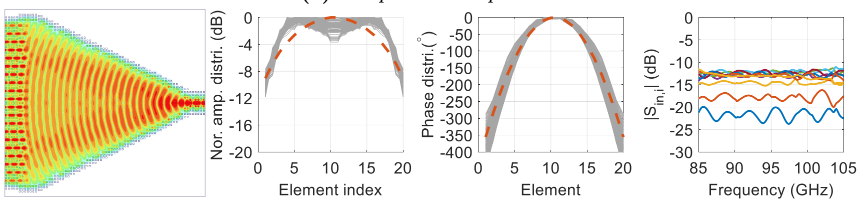

(d) *Output* 2 & *Input* 3

Figure 4.7: Different configurations of the full QO feed and corresponding (from left to right): (1) E-filed distribution at $f_0 = 95GHz$; (2) normalized amplitude tapers and (3) phase distributions of the S-parameters of the QO output ports, and (4) QO's transmission coefficients.

System level numerical results

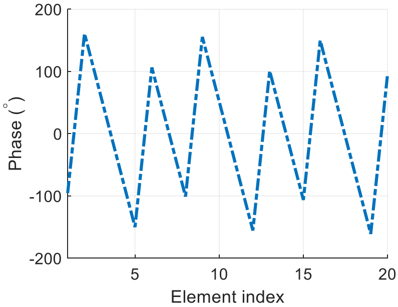

(a) Required (ideal) linear phase excitation of the array elements at $\theta_{sc} = 30°$

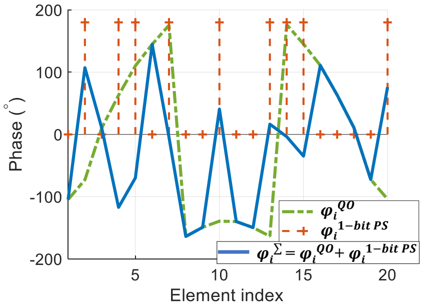

(b) Realized phase excitation φ_i^{Σ} by 1-bit PS + QO feed at $\theta_{sc} = 30°$

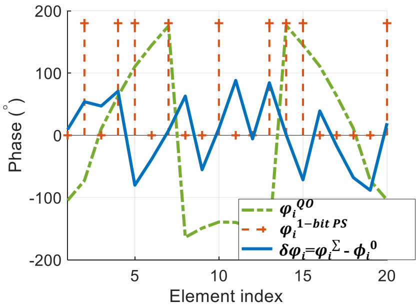

(c) Predicted phase errors $\delta\varphi$ by 1-bit PS + QO feed compared to the ideal phase at $\theta_{sc} = 30°$

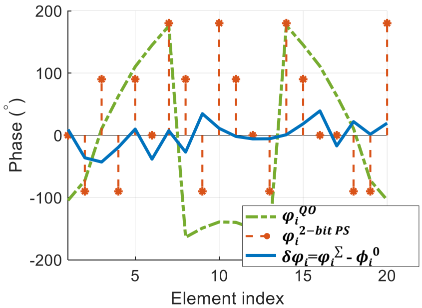

(d) Predicted phase errors $\delta\varphi$ by 2-bit PS + QO feed compared to ideal phase at $\theta_{sc} = 30°$

Figure 4.8: Predicted or simulated phase excitations with 1-bit and 2-bit PSs and the QO feed at $\theta_{sc} = 30°$.

In this section, the array + beam-forming (BF) performance is analyzed numerically using the simulated/measured results of the individually modelled system components. In accordance with the system block diagram in Fig. 4.1, the implemented system comprises the QO configuration *Output* 1 & *Input* 3, 1×20 RGW-MMIC transitions, 1×20 on-chip 1-/2-bit PSs, 1×20 MMIC-RGW transitions, and the 20-element linear antenna array. The beam-steering performance of the active array is computed within $\pm 50°$ scan range by utilizing active PSs' states at each scan angle according to Eq. (4.1) and (4.2). The system level performance is analyzed by cascading the S-matrix of all corresponding components and post-processing these results with the embedded element patterns of the linear array.

Phase excitation of the sub-array elements with 1-/2-bit PSs and the QO Feed

For clarity, the concept of achieving the designed phase excitation with a combination of 1-bit / 2-bit PSs and the QO feed is illustrated in Fig. 4.8. Firstly, the ideal phase excitation of the elements for a scan angle $\theta_s = 30°$ is depicted in Fig. 4.8(a). It's computed using $\Phi_i^0 = -k_0 x_i \sin(\theta_s)$ for 1×20 elements, implying optimal phase control.

Fig. 4.8(b) demonstrates the composition of the QO phase excitation φ_i^{QO} from QO configuration *Output* 1 & *Input* 3 and the phase shifts φ_i^{PS} from ideal PSs. Given that φ_i^{PS} only contains 0° and 180° states, the result of $\varphi_i^{\Sigma} = \varphi_i^{QO} + \varphi_i^{PS}$ (see Eq. (4.2)) deviates from the desired phase distribution Φ_i^0.

The phase difference $\delta\varphi_i = \varphi_i^{\Sigma} - \Phi_i^0$ is due to quantization errors (see Fig. 4.8(c)). If the system employs 2-bit PSs, the quantization errors are reduced (see Fig. 4.8(d)). To take into account the actual phase states of on-chip PSs, the measured results of 1-/2-bit PSs are used in the following system numerical analysis, rather than ideal phase states. These results are presented in Fig. 4.9. In the following section, $\delta\varphi_i$ represents the system phase errors.

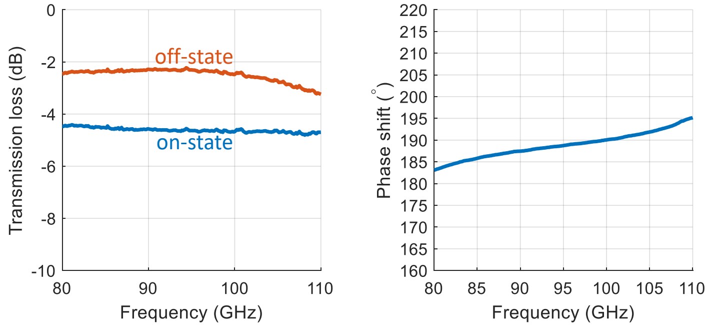

(a) 1-bit PS's transmission loss in on / off states and the phase shift

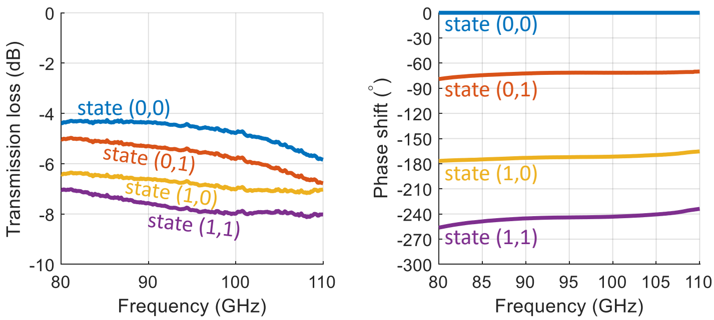

(b) 2-bit PS's transmission loss and phase shift in four states

Figure 4.9: Measured results of (a) the 1-bit and (b) 2-bit on-chip PSs with *WIN PH1-10 GaAs process*.

System gain loss budget analysis

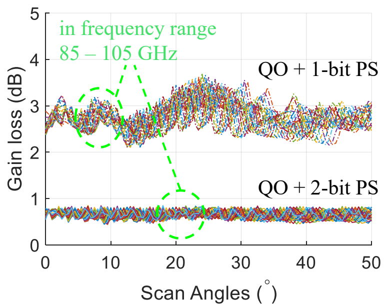

(a) numerical QO model, F/D = 1.2

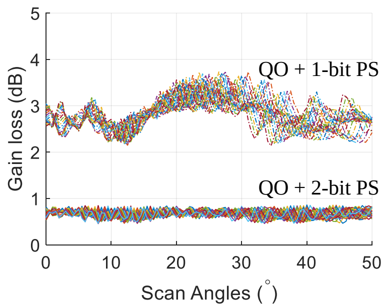

(b) numerical QO model, F/D = 1.4

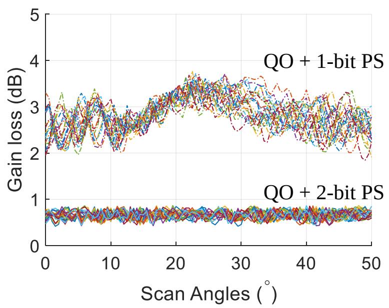

(c) QO configuration *Output* 1 & *Input* 3

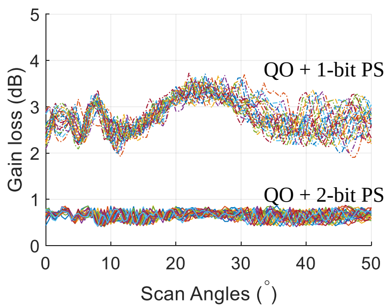

(d) QO configuration *Output* 1 & *Input* 1

Figure 4.10: The gain loss due to the system phase errors of different QO configurations with active PSs' states as obtained from on-chip measurements over the operational frequency band 85–105 GHz. Each frequency range plot show 81 gain loss curves from 85–105 GHz.

The average system gain loss due to the quantization errors and the phase shift deviations is analyzed here. We observe that the phase errors depend on the on-chip PS implementation and the type of GWG QO configurations. The resulting system gain loss is computed at each angle and frequency for $|\theta_s| \leq 50°$ in the 85–105 GHz range, assuming that the array amplitude distribution is uniform. For a more realistic scenario, the measured results of on-chip GaAs PSs (see Fig. 4.9) are used in the computation: for the 1-bit PS, the realized phase shift is $190 \pm 8°$ with an insertion loss of 3 ± 1 dB.

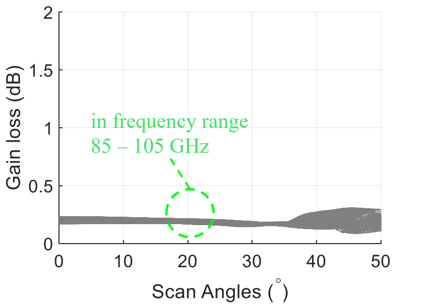

(a) numerical QO model, amplitude taper 6 dB

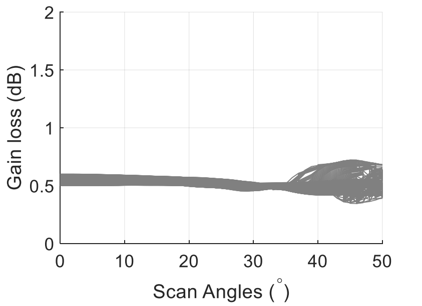

(b) numerical QO model, amplitude taper 10 dB

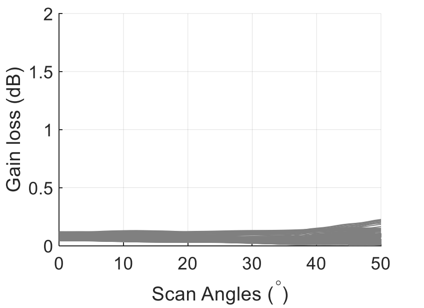

(c) QO configuration *Output* 1 & *Input* 3

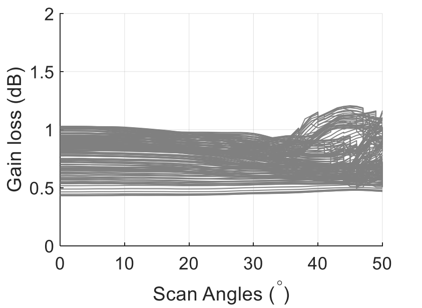

(d) QO configuration *Output* 1 & *Input* 1

Figure 4.11: The gain loss contribution due to the output amplitude taper of the QO feed over the operational frequency band 85–105 GHz. Each frequency range plot show 81 gain loss curves from 85–105 GHz.

The gain loss from *Output* 1 & *Input* 3 and *Output* 1 & *Input* 1 implementations are presented in Fig. 4.10(c), 4.10(d). For comparison, the gain loss computed from numerical QO models with $F/D = 1.2, 1.4$ are also presented in Fig. 4.10(a), 4.10(b). We can observe that the GWG QOs (see Fig. 4.10(c), 4.10(d)) reproduce the gain loss curves from the corresponding numerical models for $F/D = 1.2, 1.4$ QO phase fronts shown in Fig. 4.10(a), 4.10(b). Although the GWG *Output* 1 configurations all implement $F/D = 1$ radial GWG walls, their $17P_{EBG}$-long elongated outputs increase the equivalent F/D around 1.2-1.4. The gain loss is comparable within 2.2-3.7 dB over the scan range. However, the differences become more visible in the results of the *Output* 1 & *Input* 3 configuration, where the gain loss fluctuates more. This is primarily due to the existence of high-order modes.

The system gain reduction due to the amplitude taper is analyzed using the output amplitude tapers of the ideal numerical QO and GWG QO models, assuming that the phase excitation for the array elements is ideally equal to Eq. (4.2). As depicted in Fig. 4.11(a), 4.11(b), the amplitude taper has a minor impact on the system gain. With a 6 dB taper, the related system gain degrades only by 0.2-0.4 dB; while a 10 dB taper results in a relatively larger loss of 0.4-0.7 dB. Since the QO configurations *Output* 1 & *Input* 3 and *Output* 1 & *Input* 1 have similar phase distributions but very different amplitude tapers (see Fig. 4.7(a), 4.7(c)), their resultant gains are different.

The QO configuration *Output* 1 & *Input* 3 creates an amplitude taper of only 4 dB, resulting in ≤ 0.2dB gain loss, thanks to the over-moded illumination. In contrast, the *Output* 1 & *Input* 1 configuration with a large amplitude taper leads to a more severe gain loss ranging from 0.4 to 1.2 dB. Therefore, QO configuration *Output* 1 & *Input* 3 is considered the most effective solution.

Finally, the total system gain can be predicted by considering the array amplitude taper, phase errors, and all components' insertion loss. While the available active PS states can provide finer phase resolution and reduce phase quantization errors, they may introduce larger insertion losses.

This trade-off is analyzed by comparing the total system available realized gain and relative SLLs. As illustrated in Fig. 4.9, the 1-bit PS demonstrates an average insertion loss of 2.2 and 4.6 dB in its two states. For the 2-bit PS case, the insertion loss values observed are 4.6, 5.8, 6.8, and 7.9 dB respectively. Simultaneously, the resulting system phase errors for the 2-bit PS case are much smaller (≤ 0.7 dB) over frequencies and scan angles. A comparison of their system available gains is made in Fig. 4.12 at selected frequencies over the $|\theta_s| \leq 50°$ range.

The maximum system gain is computed by Eq. (4.1) with the ideal conjugate matching conditions for all array elements. If PS insertion loss is not considered, it is clear in all cases that the 2-bit PS case has the largest system available gain: around 1 dB lower than the ideal case and 2 dB higher than for the 1-bit PS case. This is expected based on the results in Fig. 4.2(b). However, when all the insertion loss contributions from the individual compo-

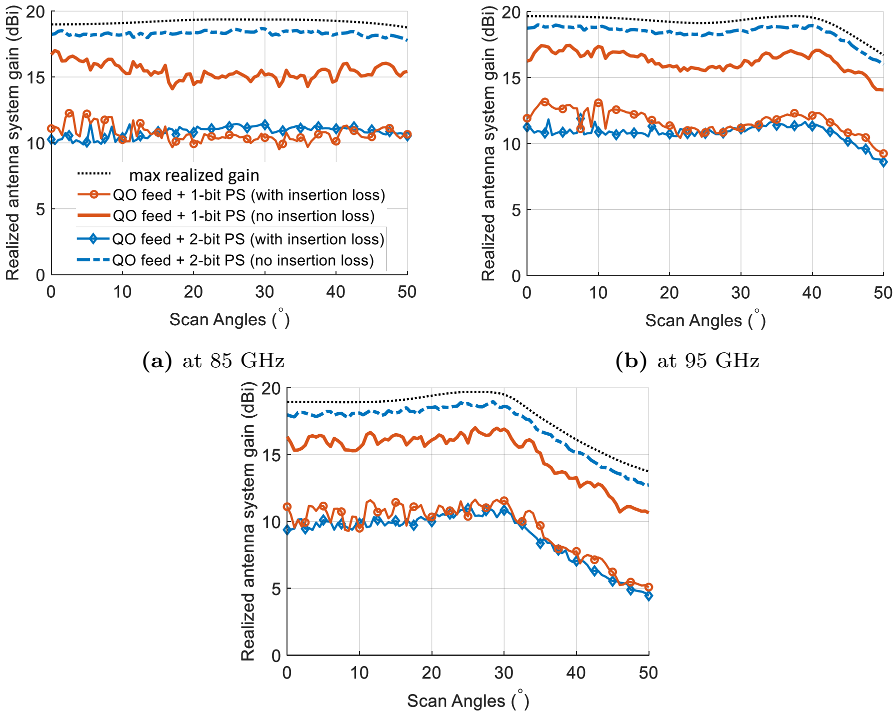

(a) at 85 GHz

(b) at 95 GHz

(c) at 105 GHz

Figure 4.12: Realized system available gain of the linear array system by cascading all components and controlling active 1-/2-bit PS states.

nents are included, the average available gains for both cases drop to similar levels, introducing around 9 dB gain degradation over all scan angles.

The relative SLL levels depicted in Fig. 4.13 underline the advantage of the 2-bit PS case. The relative mean SLL levels of 2-bit case are around -(15–20) dB for all angles at the selected frequencies, while the 1-bit case always show higher SLL levels, by more than -15 dB. The maximum relative SLL level for the 1-bit case can be higher than -5 dB for some scan angles, but only around -10 dB for 2-bit cases.

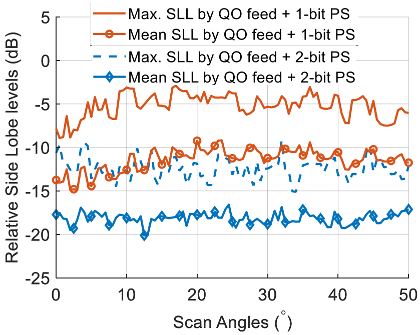

(a) at 85 GHz

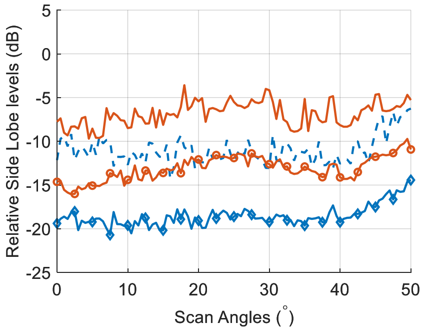

(b) at 95 GHz

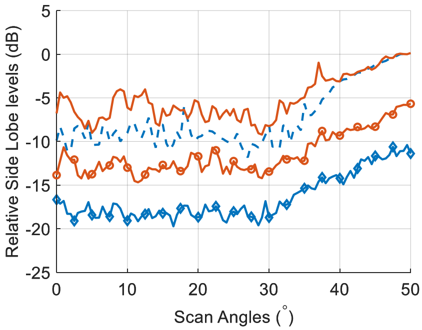

(c) at 105 GHz

Figure 4.13: Relative maximum and mean side lobe levels (SLL) of the linear array system obtained by cascading all components and controlling active 1-/2-bit PS states.

CHAPTER 5

Summary of included papers

This chapter provides a summary of the included papers.

5.1 Paper A

Y. Zhang, A. R. Vilenskiy, M. V. Ivashina
W-band Waveguide Antenna Elements for Wideband and Wide-Scan Array Antenna Applications For Beyond 5G
2021 15th European Conference on Antennas and Propagation (EuCAP)
Dusseldorf, Germany, Mar. 2021
©IEEE DOI: 10.23919/EuCAP51087.2021.9411184.

This paper investigated various types of antenna elements as potential candidates for wide-band and wide-scan arrays at W-band. We consider open-ended ridge and ridge gap waveguide radiating elements that could overcome the physical complexities associated with the integration of elements in large-scale electronically scanned arrays. Cross-comparison of several simulated array designs leads to the final array elements with 25% impedance bandwidth over the scan range of $\pm 40°$ in both the E- and H-planes.

5.2 Paper B

Y. Zhang, A. R. Vilenskiy, M. V. Ivashina
Wideband Open-Ended Ridge Gap Waveguide Antenna Elements for 1-D and 2-D Wide-Angle Scanning Phased Arrays at 100 GHz
IEEE Antennas and Wireless Propagation Letters
vol. 21, no: 5, pp. 883 - 887, 2022
©IEEE DOI: 10.1109/LAWP.2022.3150595.

This paper proposes a new antenna element type based on the open-ended ridge gap waveguide (RGW) at high mm-wave frequencies ($\geq$ 100 GHz). Results demonstrate a wide-angle beam-steering ($\geq 50°$) over $\geq 20\%$ fractional bandwidth at W-band with $\geq 89\%$ radiation efficiency that significantly outperforms existing solutions at these frequencies. An experimental prototype of a 1×19 W-band array validates the proposed design concept through the embedded element pattern measurements.

5.3 Paper C

Y. Zhang, A. R. Vilenskiy, M. V. Ivashina
Mutual Coupling Analysis of Open-Ended Ridge and Ridge Gap Waveguide Radiating Elements in an Infinite Array Environment
2022 52nd European Microwave Conference (EuMC)
Milan, Italy, Sept. 2022
©IEEE DOI: 10.23919/EuMC54642.2022.9924388.

In this paper, we discuss mutual coupling effects in 2-D beam-steerable antenna arrays based on open-ended ridge and ridge gap waveguide radiating elements. Various decoupling structures based on electromagnetic soft surfaces are applied to suppress the surface waves over the array apertures. The analysis demonstrates the effect of decoupling structures realizing a steep drop of the mutual coupling magnitude (≤ -20 dB) for closely-spaced array elements.

5.4 Paper D

A. R. Vilenskiy, **Y. Zhang**, M. V. Ivashina
Methods for Attenuating and Terminating Waves in Ridge Gap Waveguide at W-Band: Carbon-Loaded Foam, Carbonyl Iron Paint, and Nickel Plating
2021 51st European Microwave Conference (EuMC)
London, United Kingdom, Apr. 2022
©IEEE DOI: 10.23919/EuMC50147.2022.9784367.

Several methods for electromagnetic waves matched termination and attenuation in a ridge gap waveguide (RGW) are experimentally investigated at W-band. The following three techniques are considered: (i) filling an RGW gap with a carbon-loaded foam; (ii) covering a ridge (and pins) with a carbonyl iron paint; (iii) selective nickel plating of an RGW line segment.

5.5 Paper E

A. R. Vilenskiy, **Y. Zhang**, E. Galesloot, A. B. Smolders, M. V. Ivashina
Millimeter-Wave Quasi-Optical Feeds for Linear Array Antennas in Gap Waveguide Technology
2022 16th European Conference on Antennas and Propagation (EuCAP)
Madrid, Spain, Apr. 2022
©IEEE DOI: 10.23919/EuCAP53622.2022.9769175.

A realization of the quasi-optical (QO) feed concept for linear millimeter-wave (sub-)array antennas is demonstrated in gap waveguide technology. Various QO feed implementations are investigated at W-band demonstrating a 20% relative bandwidth (85–105 GHz), 0.5 dB insertion loss, and a capability of an amplitude taper control within the 10–20 dB range.

5.6 Paper F

A. R. Vilenskiy, E. Galesloot, **Y. Zhang**, A. B. Smolders, M. V. Ivashina
Quasi-Optical Beamforming Network for Millimeter-Wave Electronically Scanned Array Antennas with 1-Bit Phase Resolution
2021 15th European Conference on Antennas and Propagation (EuCAP)

Dusseldorf, Germany, Mar. 2021
©IEEE DOI: 10.23919/EuCAP51087.2021.9410922.

We present a new linear array antenna architecture as a building block of 2D arrays that can enable efficient beam steering and a simplified array design. This concept is based on the combination of a low-loss quasi-optical (QO) feed, providing predefined antenna port excitation, with 1-bit phase-shifters which are co-integrated with the array antenna elements. The array model is validated through numerical simulations revealing that the optimum focal ratio leads to the minimum SLL.

CHAPTER 6

Concluding Remarks and Future Work

This research contributes to the ongoing advancements in wireless communication technologies beyond 5G, by introducing a new array antenna type based on the open-ended ridge gap waveguide (RGW). The array antenna is specifically designed for the upper millimeter-wave bands (100+ GHz), providing potential solutions to the challenges of high dissipation losses, high component costs, and stringent manufacturing tolerances that conventional phased antenna array solutions often encounter. The proposed antenna design has shown promising results in terms of wide-angle beam-steering range and radiation efficiency, offering potential improvements over existing solutions at these frequencies.

This RGW element can be manufactured with relative ease, using two split blocks assembled contactlessly. This unique feature allows for the integration of active electronics within its structure, potentially enabling hybrid electronic beam-steering at high mm-wave frequencies. The 2-D array element exhibits wideband ($\geq 20\%$) and wide-angle ($\geq 50°$) beam-steering performance with high radiation efficiency ($\geq 89\%$) at W-band, thereby demonstrating its robust performance capabilities.An experimental study of the 1-D array verifies the results of the infinite array simulation model.

Furthermore, this study proposes a linear (sub-)array architecture that possesses 1-D beam-steering capability, serving as a building block for 2D arrays. A low-loss gap waveguide (GWG)-based quasi-optical (QO) feed is designed for feeding the array, and such array architecture potentially allows for co-integration of 1-/2-bit phase-shifters within each array element. This innovative approach optimizes the quasi-randomization of phase errors through the QO feed, achieving design goals of maximum available gain and minimum sidelobe levels. Both the GWG QO feed and the on-chip phase-shifters (collaborated work) have been designed and validated independently through measurements. A system-level numerical analysis of the beam-forming linear (sub-)array antenna, which includes the spatial QO beam-forming network, has been conducted. This analysis involved cascading the scattering parameters of individual system components and applying optimal beam-forming coefficients to the array elements to produce beam-steered radiation patterns.

In conclusion, this work explores innovative designs and methods that have the potential to improve the performance and efficiency of future wireless communication systems, especially in scenarios where high data throughput over long distances is desired.

The final goal of the PhD thesis is to develop a 2-D array prototype with hybrid beam-forming including the integration of phase-shifting and PA circuitry into the element's RGW (collaborated work).

References

[1] *European vision for the 6G network ecosystem*, White Paper, The 5G Infrastructure Association, Jun. 2021.

[2] T. S. Rappaport, Y. Xing, O. Kanhere, *et al.*, "Wireless communications and applications above 100 GHz: Opportunities and challenges for 6G and beyond," *IEEE Access*, no. 7, pp. 78 729–78 757, 2019.

[3] Y. Xing and T. S. Rappaport, "Propagation measurement system and approach at 140 ghz-moving to 6g and above 100 ghz," in *2018 IEEE global communications Conference (GLOBECOM)*, IEEE, 2018, pp. 1–6.

[4] T. S. Rappaport, R. W. Heath Jr, R. C. Daniels, and J. N. Murdock, *Millimeter wave wireless communications*. Pearson Education, 2015.

[5] M. V. Ivashina, A. R. Vilenskiy, H.-T. Chou, J. Oberhammer, and M. Ng Mou Kehn, " Antenna technologies for beyond-5G wireless communication: Challenges and opportunities," in *Proc. 2021 International Symposium on Antennas and Propagation (ISAP)*, Taipei, Taiwan, 2021, pp. 1–2.

[6] R. J. Mailloux, *Phased array antenna handbook*. Artech house, 2017.

[7] B. Sadhu, X. Gu, and A. Valdes-Garcia, "The more (antennas), the merrier: A survey of silicon-based mm-wave phased arrays using multi-ic scaling," *IEEE Microwave Magazine*, vol. 20, no. 12, pp. 32–50, 2019.

[8] X. Gu, A. Valdes-Garcia, A. Natarajan, B. Sadhu, D. Liu, and S. K. Reynolds, “W-band scalable phased arrays for imaging and communications,” *IEEE communications magazine*, vol. 53, no. 4, pp. 196–204, 2015.

[9] A. Valdes-Garcia, B. Sadhu, X. Gu, J.-O. Plouchart, M. Yeck, and D. Friedman, “Scaling millimeter-wave phased arrays: Challenges and solutions,” in *2018 IEEE BiCMOS and Compound Semiconductor Integrated Circuits and Technology Symposium (BCICTS)*, IEEE, 2018, pp. 80–84.

[10] Y. Zhang and J. Mao, “An overview of the development of antenna-in-package technology for highly integrated wireless devices,” *Proceedings of the IEEE*, vol. 107, no. 11, pp. 2265–2280, 2019.

[11] W. Shin, B.-H. Ku, O. Inac, Y.-C. Ou, and G. M. Rebeiz, “A 108–114 GHz 4× 4 wafer-scale phased array transmitter with high-efficiency on-chip antennas,” *IEEE Journal of Solid-State Circuits*, vol. 48, no. 9, pp. 2041–2055, 2013.

[12] *Power amplifiers performance survey 2000-present*, Online Available: https://gems.ece.gatech.edu/PA$_{s}$*urvey.html*, 2020.

[13] U. K. Mishra, L. Shen, T. E. Kazior, and Y.-F. Wu, “Gan-based rf power devices and amplifiers,” *Proceedings of the IEEE*, vol. 96, no. 2, pp. 287–305, 2008.

[14] X. Gu, D. Liu, and B. Sadhu, “Packaging and antenna integration for silicon-based millimeter-wave phased arrays: 5g and beyond,” *IEEE Journal of Microwaves*, vol. 1, no. 1, pp. 123–134, 2021.

[15] W.-C. Liao, A. R. Vilenskiy, R. Maaskant, T. Emanuelsson, V. Vassilev, and M. V. Ivashina, “Mmwave metal bowtie slot array element integrating power amplifier mmic via on-chip probe to enhance efficiency and bandwidth,” *IEEE Transactions on Antennas and Propagation*, vol. 70, no. 9, pp. 8110–8121, 2022.

[16] M. de Kok, A. B. Smolders, and U. Johannsen, “A review of design and integration technologies for d-band antennas,” *IEEE Open Journal of Antennas and Propagation*, vol. 2, pp. 746–758, 2021.

[17] S. Shahramian, M. J. Holyoak, A. Singh, and Y. Baeyens, "A fully integrated 384-element, 16-tile, W-band phased array with self-alignment and self-test," *IEEE Journal of Solid-state Circuits*, vol. 54, no. 9, pp. 2419–2434, 2019.

[18] X. Gu, D. Liu, C. Baks, J.-O. Plouchart, W. Lee, and A. Valdes-Garcia, "An enhanced 64-element dual-polarization antenna array package for W-band communication and imaging applications," in *Proc. 2018 IEEE 68th Electronic Components and Technology Conference (ECTC)*, 2018, pp. 197–201.

[19] Z. W. Miao, Z. C. Hao, G. Q. Luo, *et al.*, "140 GHz high-gain ltcc-integrated transmit-array antenna using a wideband siw aperture-coupling phase delay structure," vol. 66, no. 1, pp. 182–190, 2018, ISSN: 0018926X.

[20] X. Gu, D. Liu, C. Baks, *et al.*, "A compact 4-chip package with 64 embedded dual-polarization antennas for w-band phased-array transceivers," in *2014 IEEE 64th electronic components and technology conference (ECTC)*, IEEE, 2014, pp. 1272–1277.

[21] X. Pan, S. Wang, G. Li, S. Xu, and F. Yang, "On-chip reconfigurable reflectarray for 2-d beam-steering at W-band," in *Proc. 2018 IEEE MTT-S International Wireless Symposium (IWS)*, 2018, pp. 1–4.

[22] P. Fratilescu, S. Garcıa-Ruano, G. Perez-Palomino, and E. Carrasco, "W-band confocal antenna system based on liquid crystal reflectarray for beam scanning applications," in *Proc. 2021 15th European Conference on Antennas and Propagation (EuCAP)*, 2021, pp. 1–5.

[23] A. B. Numan, J.-F. Frigon, and J.-J. Laurin, "Printed W-band multibeam antenna with luneburg lens-based beamforming network," *IEEE Transactions on Antennas and Propagation*, vol. 66, no. 10, pp. 5614–5619, 2018.

[24] S. Manafi, J. F. González, and D. Filipovic, "Design of a perforated flat luneburg lens antenna array for wideband millimeter-wave applications," in *Proc. 2019 13th European Conference on Antennas and Propagation (EuCAP)*, 2019, pp. 1–5.

[25] R. Reese, E. Polat, H. Tesmer, *et al.*, "Liquid crystal based dielectric waveguide phase shifters for phased arrays at W-band," *IEEE Access*, vol. 7, pp. 127 032–127 041, 2019.

[26] B. L. Cannon, K. J. Vanhille, and G. A. Sadowy, "Microfabricated dual-polarized, W-band antenna architecture for scalable line arrav feed," in *2015 IEEE International Symposium on Antennas and Propagation & USNC/URSI National Radio Science Meeting*, 2015, pp. 615–616.

[27] S. S. Yao and Y. J. Cheng, "W-band high-efficiency wideband planar array antenna based on mems micromachining technology," in *Proc. 2018 48th European Microwave Conference (EuMC)*, 2018, pp. 942–945.

[28] D. Kim, J. Hirokawa, M. Ando, J. Takeuchi, and A. Hirata, "64×64-element and 32×32-element slot array antennas using double-layer hollow-waveguide corporate-feed in the 120 GHz band," vol. 62, no. 3, pp. 1507–1512, 2014.

[29] J. W. Jordan, S. Lynch, M. Clark, *et al.*, "Monolithically fabricated 4096-element, polystrata® broadband d-band array demonstrator," in *Proc. 2019 IEEE MTT-S International Microwave Symposium (IMS)*, 2019, pp. 1060–1063.

[30] A. Gomez-Torrent, M. Garcia-Vigueras, L. Le Coq, *et al.*, "A low-profile and high-gain frequency beam steering subterahertz antenna enabled by silicon micromachining," vol. 68, no. 2, pp. 672–682, 2020.

[31] D. A. Schneider, M. Rösch, A. Tessmann, and T. Zwick, "A low-loss W-band frequency-scanning antenna for wideband multichannel radar applications," *IEEE Antennas and Wireless Propagation Letters*, vol. 18, no. 4, pp. 806–810, 2019.

[32] M. de Kok, A. B. Smolders, C. J. Vertegaal, and U. Johannsen, "Active ka-band open-ended waveguide antenna with built-in ic cooling for use in large arrays," in *2021 18th European Radar Conference (EuRAD)*, IEEE, 2022, pp. 86–89.

[33] A. U. Zaman and P.-S. Kidal, "Gap waveguide in handbook of antenna technologies," in New York, NY: Springer Science+ Business Media Singapore, 2015, p. 464.

[34] P.-S. Kildal, E. Alfonso, A. Valero-Nogueira, and E. Rajo-Iglesias, "Local metamaterial-based waveguides in gaps between parallel metal plates," vol. 8, pp. 84–87, 2009.

[35] Y. Rong and K. A. Zaki, "Characteristics of generalized rectangular and circular ridge waveguides," vol. 48, no. 2, pp. 258–265, 2000.

[36] A. K. Bhattacharyya, *Phased array antennas: Floquet analysis, synthesis, BFNs and active array systems.* John Wiley & Sons, 2006, vol. 179.

[37] J. Montgomery, "Ridged waveguide phased array elements," vol. AP-24, no. 1, pp. 46–53, 1976.

[38] P.-S. Kildal, A. A. Kishk, and S. Maci, "Special issue on artificial magnetic conductors, soft/hard surfaces, and other complex surfaces," vol. 53, no. 1, pp. 2–7, 2005.

[39] E. Adas, F. De Flaviis, and N. G. Alexopoulos, "Realization of scan blindness free finite microstrip phased arrays based on mode-free radiating electromagnetic bandgap materials," *IEEE Transactions on Antennas and Propagation*, vol. 66, no. 7, pp. 3375–3382, 2018.

[40] D. T. McGrath, "Calculation of coupling coefficients for arrays with skewed lattices from infinite array scan reflection data," *IEEE Transactions on Antennas and Propagation*, vol. 55, no. 7, pp. 2116–2119, 2007.

[41] V. I. Litun, H. Rashid, and E. V. Komissarova, "Unit-cell versus finite array approaches for antenna array design," in *2021 Antennas Design and Measurement International Conference (ADMInC)*, 2021, pp. 23–26.

[42] A. Aljarosha, A. U. Zaman, and R. Maaskant, "A wideband contactless and bondwire-free mmic to waveguide transition," *IEEE Microwave and Wireless Components Letters*, vol. 27, no. 5, pp. 437–439, 2017.

[43] P.-S. Kildal, "Definition of artificially soft and hard surfaces for electromagnetic waves," *Electronics Letters*, vol. 24, pp. 168–170, 3 Feb. 1988.

[44] W. Hong, K.-H. Baek, Y. Lee, Y. Kim, and S.-T. Ko, "Study and prototyping of practically large-scale mmWave antenna systems for 5G cellular devices," *IEEE Communications Magazine*, vol. 52, no. 9, pp. 63–69, 2014.

[45] U. Chipengo, A. Sligar, and S. Carpenter, "High fidelity physics simulation of 128 channel mimo sensor for 77 GHz automotive radar," *IEEE Access*, vol. 8, pp. 160 643–160 652, 2020.

[46] N. Amitay, V. Galindo, and C. P. Wu, *Theory and Analysis of Phased Array Antennas.* New York: Wiley Interscience, 1972.

[47] X. Liang, Z. Zhang, J. Zeng, F. Guan, X. Liu, and J. Zi, "Scan blindness free design of wideband wide-scanning open-ended waveguide phased array," *IEEE Access*, vol. 9, pp. 68 127–68 138, 2021.

[48] M. C. Viganó, D. L. del Río, F. Bongard, and S. Vaccaro, "Sparse array antenna for Ku-band mobile terminals using 1 bit phase controls," vol. 62, no. 4, pp. 1723–1730, Apr. 2014.

[49] A. Clemente, L. Dussopt, R. Sauleau, P. Potier, and P. Pouliguen, "Wideband 400-element electronically reconfigurable transmitarray in X band," vol. 61, no. 10, pp. 5017–5027, Oct. 2013.

[50] A. R. Vilenskiy, M. N. Makurin, C. Lee, and M. V. Ivashina, "Reconfigurable transmitarray with near-field coupling to gap waveguide array antenna for efficient 2D beam steering," vol. 68, no. 12, pp. 7854–7865, Dec. 2020.

[51] A. Clemente, F. Diaby, L. D. Palma, L. Dussopt, and R. Sauleau, "Experimental validation of a 2-bit reconfigurable unit-cell for transmitarrays at Ka-band," *IEEE Access*, vol. 8, pp. 114 991–114 997, 2020.

[52] J. G. Yang, J. Lee, and K. Yang, "A w-band ingaas pin-mmic digital phase-shifter using a switched transmission-line structure," in *2012 International Conference on Indium Phosphide and Related Materials*, IEEE, 2012, pp. 99–101.

[53] M. S. Smith and Y. C. Guo, "A comparison of methods for randomizing phase quantization errors in phased arrays," vol. 31, no. 6, pp. 821–828, Nov. 1983.

[54] R. Maaskant, W. A. Shah, A. U. Zaman, M. Ivashina, and P.-S. Kildal, "Spatial power combining and splitting in gap waveguide technology," *IEEE Microw. Wireless Compon. Lett.*, vol. 26, no. 7, pp. 472–474, Jul. 2016.

[55] A. R. Vilenskiy, M. N. Makurin, E. I. Poshisholina, and C. Lee, "Design technique for varactor analog phase shifters with equalized losses," *Progress In Electromagnetics Research C*, vol. 86, pp. 1–16, 2018.

[56] R. J. Mailloux, *Phased array antenna handbook*, Second. Norwood, MA: Artech House, 2018.

[57] A. R. Vilenskiy, M. N. Makurin, and C. Lee, “Phase distribution optimization for 1-bit transmitarrays with near-field coupling feeding technique,” in *Proc. 14th European Conference on Antennas and Propagation, (EuCAP 2020)*, Copenhagen, Denmark, Mar. 2020, pp. 1–5.

Part II

Papers

PAPER A

W-band Waveguide Antenna Elements for Wideband and Wide-Scan Array Antenna Applications For Beyond 5G

Y. Zhang, A. R. Vilenskiy, M. V. Ivashina

2021 15th European Conference on Antennas and Propagation (EuCAP)
Dusseldorf, Germany, Mar. 2021
 DOI: 10.23919/EuCAP51087.2021.9411184

The layout has been revised.

Abstract

Energy-efficient and highly-compact beam-steering array antennas at W- and D-band frequencies are considered as future enabling technologies for beyond-5G applications. However, most existing solutions at these frequencies are limited to the fixed-beam and frequency-dependent beam-steering scenarios. This paper aims to fill in this knowledge gap by investigating various types of antenna elements as potential candidates for wideband and wide-scan arrays at W-band. We consider open-ended ridge and ridge gap waveguide radiating elements that could overcome the physical complexities associated with the integration of elements in large-scale electronically scanned arrays. An infinite array approach is used, where we have adopted a triangular array grid and introduced E- and H-plane grooves to the element design to enhance the scan and bandwidth performance. Cross-comparison of several simulated array designs leads to the final array elements with 25% impedance bandwidth over the scan range of ±40° in both the E- and H-planes.

1 Introduction

The development of future beyond-5G (B5G) wireless communication applications, products, and services strongly relay on innovative antenna technologies that can operate at higher bands of the mm-wave frequency spectrum (i.e. 100+GHz). The W-band (75–110 GHz) and D-band (110–170 GHz) are considered among most promising directions of development owing to the wide available bandwidth and relatively low atmospheric absorption loss, and have already been employed in the automotive radar applications as well as in backhauling and multi-user wireless communications.

Antenna systems for these future applications are required to have a much higher effective radiated power, as compared to the presently deployed 5G systems, in order to compensate for the increased material losses and reduced power generation ability of active electronic devices at higher frequencies. Other challenges include significantly smaller antenna dimensions, and, hence, tighter manufacturing tolerances and extra difficulties of integrating active integrated circuits (IC) (that become comparable in size with antenna elements) and signal routing, especially in large-scale arrays.

Due to the above-mentioned physical and manufacturing challenges, to date, most reported designs of high-gain, high-efficiency W-/D-band array antennas are for fixed-beam applications (often referred to as fixed wireless access). One example of such antenna technologies is LTCC on-package array antennas that have obvious integration advantages, but suffer from poor efficiency (typically, $< 35\%$) [1]. In contrast, hollow waveguide (WG) type antennas have much higher efficiency ($> 50\%$) [2], while benefiting from high-precision CNC-milling manufacturing techniques, but are less versatile in terms of beamforming capabilities as these require dedicated WG-to-IC transitions which are typically lossy and occupy much space. Recent developments in silicon micro-machining have demonstrated even higher efficiencies (>70%) [3] thanks to their nanometer surface roughness. However, these are still at the research development stage. It is worth mentioning that there are available published beam-steering solutions for large-scale array antennas at W-/D-bands and higher frequencies, but these are limited to traveling-wave antennas with frequency dependent beam steering [4], [5], which are not practical for our targeted applications. Other 2D beam-steering solutions that are based on AoC (Antenna-On-Chip) and SiP (System-In-Package) implementations, as realized today at 60 GHz bands [6], have limited potential to simultaneously achieve the required wideband and wide-angle beam-steering performance with high radiation efficiency.

In the present work, we investigate and cross-compare various types of antenna elements as potential candidates for wideband and wide-scan 2D electronically scanned arrays at W/D-band. The considered designs include open-ended ridge waveguide and ridge gap waveguide radiating elements (this choice is motivated by the expected high efficiency), where we have introduced several modifications with respect to standard implementations in the form of E- and H-plane grooves. Furthermore, a triangular uniform array grid is chosen to enhance the grating lobe-free scan and bandwidth performance of the arrays of such antenna elements. The antenna array element is optimized to achieve the best bandwidth vs. scan range trade-off, subject to practical implementation constraints in terms of the size and complexities of the element geometrical features as well as the spacing needed to accommodate WG-to-IC transitions [7].

The structure of the paper is the following: Section 2 presents the designs of the considered array antenna elements in the infinite array setup; Section 3 illustrates the simulated results of different array antenna elements; Section 4 analyzes the results of design optimization and trade-off studies between the impedance bandwidth and beam-steering range. Finally, key observations and future directions of this work are summarized in Section 5.

2 Array antenna element designs

We consider the open-ended WG antenna element as the starting point of the array antenna design in this work, where such elements can be cascaded with active electronics to form independent beam-steering channels [8]. In this section, a set of open-ended WG elements are designed for the operation in the infinite array scenario.

2.1 Open-ended ridge waveguide antenna element

The initial design of the open-ended WG antenna array element is shown in Fig.1(a). A single ridge is adopted inside the WG structure to lower the cut-off frequency of its fundamental mode, thus providing a wideband low-dispersive operation [9] with transverse element size close to $0.5\lambda_0$ (λ_0 is the free-space wavelength corresponding to the central design frequency f_0). Various open-ended ridge WG elements have been studied previously including dual- and quad-ridge element designs [10], [11]. However, the reported wideband beam-steering performance was limited due to impedance mismatch (e.g., VSWR $<$ 4 in the 11% bandwidth and 60° scan range for the X-band array element with half-wavelength E-plane size at central frequency in [10]). In this study, we employ several wideband techniques to improve the element's active reflection coefficient during beam steering.

The WG elements are arranged in a triangular array grid [see Fig. 2(a)] that has been chosen to relax the requirements on the array inter-element spacing in the H-plane [12]. This allows for $> 0.5\lambda_0$ inter-element-spacing for grating lobe-free wide-angle beam steering. The increased H-plane spacing is also beneficial for lowering the WG cut-off frequency and increasing the available physical space for active electronics integration behind the array aperture. As Fig. 2(a) shows, the inter-element spacing values were chosen as $0.5\lambda_0$ and

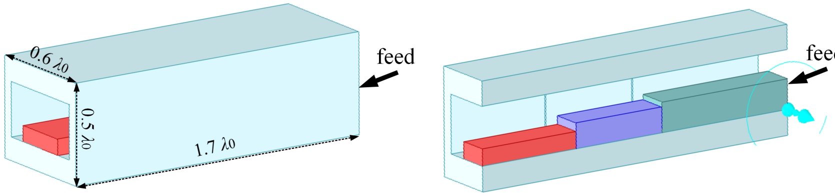

(a) Initial configuration of the open-ended ridge WG array element.

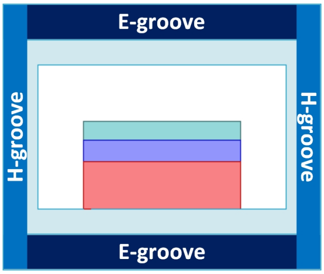

(b) Front view of the ridge WG element aperture with optional E- and H-plane grooves.

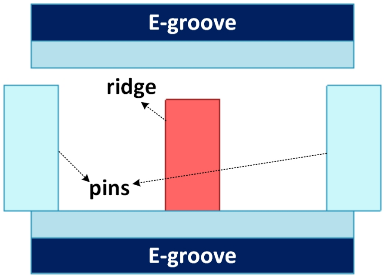

(c) Front view of the ridge gap WG (RGW) element aperture with optional E-plane grooves.

Figure 1: Various types of array antenna elements

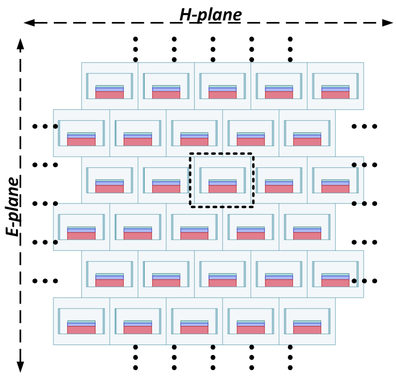

(a) Array grid

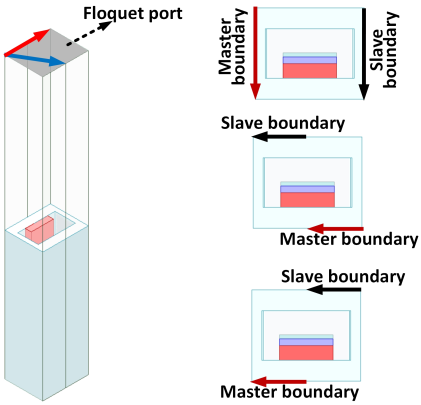

(b) Floquet port and boundary conditions

Figure 2: Infinite array model

$0.6\lambda_0$ in the E- and H-plane, respectively.

It is well know that open-ended WG array antennas have relatively strong antenna element mutual coupling effects [10], [12]. This can be a limiting factor of the bandwidth and scan range, where the latter often results in scan-blindness. This problem can be successfully overcome by adding grooves between the radiating WG elements [13]. These grooves operate as a soft surface, and hence, stop the electromagnetic waves propagation above the array aperture, thus effectively decoupling the array elements. To study this approach, we consider two additional ridge WG array elements: the element with only E-plane grooves, and the element with E- and H-plane grooves [Fig.1(b)]. In all cases, the two-step transformer is used to improve a wideband impedance matching with the free space: the ridge height is reduced in a stepped manner while the WG widens accordingly in the H-plane [see Fig. 1(a)].

2.2 Open-ended ridge gap waveguide (RGW) antenna element

The ridge WG element requires good electrical contacts between its sidewalls and is very sensitive to manufacturing errors and assembling misalignment. Such closed WG structures create additional implementation challenges when attempting the integration with active electronics and control lines tracing [8]. To address these problems, we propose a novel array element design based on an open-ended ridge gap waveguide (RGW) [14]. Its front view is shown in Fig. 1(c). The main advantage of the RGW design is its intrinsically contactless structure, which thereby allows for low-cost manufacturing, especially at high millimeter wave frequencies [14]. Also, the gap provides the desired extra space for ICs and WG-IC transition structures. The RGW unit cell sizes are the same as for the ridge WG element. We will consider two RGW element configurations: the initial design and the design loaded with E-plane grooves. The ridge height is again reduced at the aperture area to improve the impedance matching.

3 Simulation Results

To characterize the array antenna element beam-steering performance in large finite array configurations, we have employed a full-wave simulation model

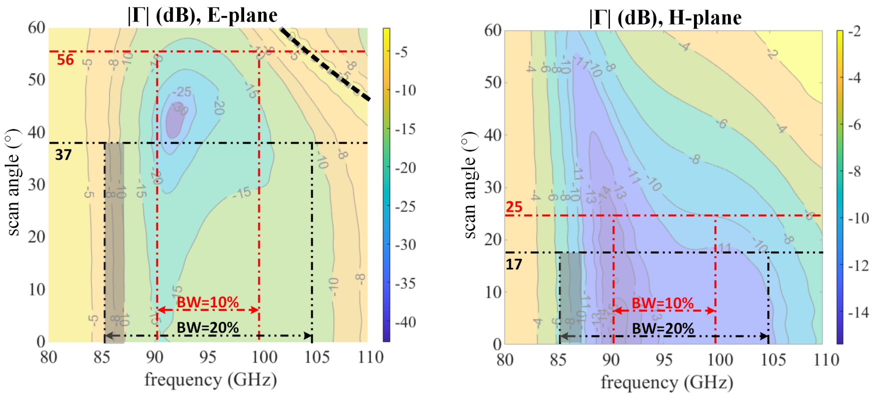

(a) Ridge WG array antenna element

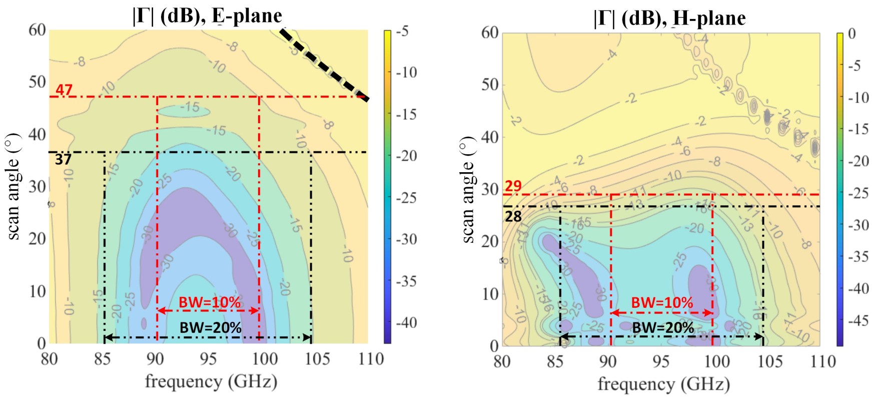

(b) Ridge WG array antenna element with E-plane grooves

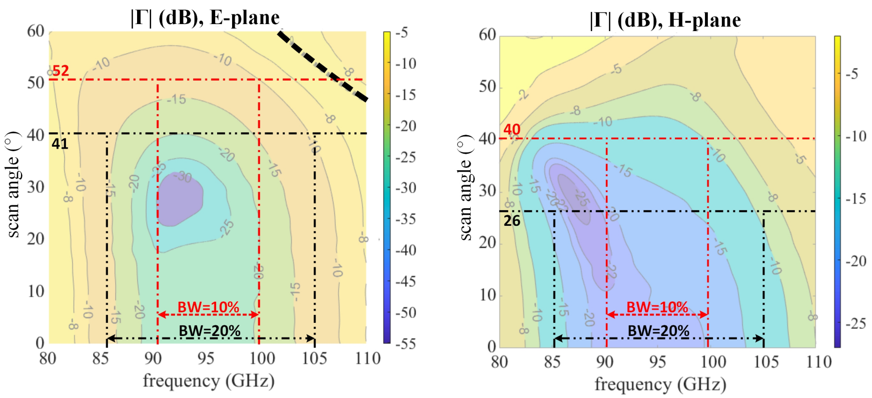

(c) Ridge WG array antenna element with the E- and H-plane grooves

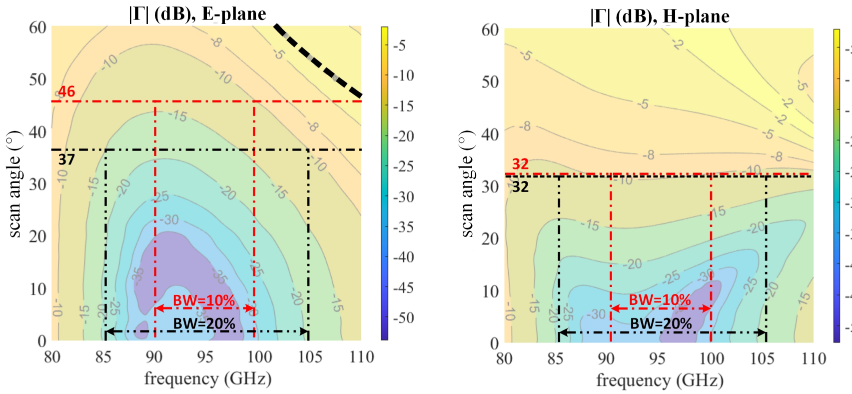

(d) RGW array antenna element

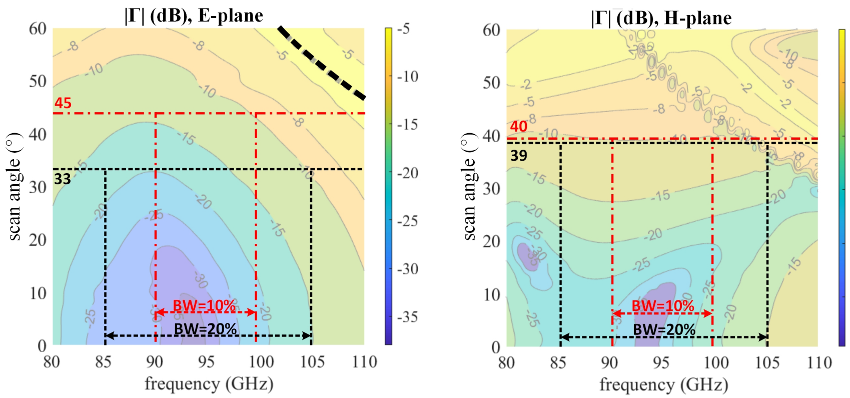

(e) RGW array antenna element with E-plane grooves

Figure 3: Active reflection coefficient (in dB) for various ridge WG and RGW array elements. The black dashed line indicates the grating lobe-free border.

of the array unit cell. This unit cell model has sidewall periodic boundary conditions and Floquet port above the element aperture. The analysis was performed in the Ansys HFSS environment with the simulation setup as shown in Fig.2(b). The central design frequency is $f_0 = 95$ GHz. All the considered element designs have been optimized to maximize the impedance matching bandwidth for the broadside radiation. The magnitude of the active reflection coefficient ($|\Gamma|$) for the beam steering in the E- and H-planes is shown in Fig. 3.

First, the results for the initial ridge WG element configuration are presented [Fig.3(a)]. The black dashed line indicates the grating lobe-free border in the E-plane, where no grating lobes can exist in the H-plane inside the studied frequency-scan angle range. As seen, the impedance matching degrades when both the scanning angle and bandwidth increase. The exemplified targeted impedance bandwidth (BW) goals of 10% and 20% ($|\Gamma| \leq -10$ dB) are depicted by the pairs of dash-dotted lines. In the E-plane, the maximum scan angle (θ_{max}) reaches 56° for the 10% BW and 37° for the 20% BW at higher BW edge. However, $|\Gamma| > -10$ dB at lower frequencies (shaded area), hence the BW is always less than 20%. At the same time, in the H-plane, the 10% and 20% bandwidth goals are achieved at the higher BW edge for beam steering up to 25°, and 17°, respectively; on the other hand, the required matching at the lower BW edge can only be achieved for frequencies above 87 GHz. The scan-blindness can be observed nearby the grating lobe entering the visible region in the E-plane (upper right area of the plot).

The beam-steering performance of the ridge WG element with only E-plane grooves and with both E- and H-plane grooves is demonstrated in Fig. 3(b) and Fig. 3(c), respectively. The width and depth values of the grooves were optimized to improve the active reflection coefficient. When the E-plane grooves are added, the array demonstrates a significantly larger bandwidth for the broadside beam in both E- and H-planes. In the E-plane, θ_{max} reaches 47° and 37° for the 10% and 20% BW goals, respectively [Fig.3(b)]. In the H-plane, θ_{max} has been increased to 29° and 28° within the 10% and 20% BW, respectively. The E-plane scan-blindness has been fully mitigated. On the other hand, we can observe the appearing scan-blindness phenomena in the H-plane (upper right area of the plot) that is associated with the mutual coupling effects in the triangular grid as caused by the E-plane grooves.

Next, we analyze the results of the array antenna element design with E- and H-pane grooves. As observed in Fig.3(c), the beam-steering performances has been improved further, as compared to the above-described configurations. In the E-plane, θ_{max} reaches 52° and 41° for the 10% and 20% BW goals, respectively. In the H-plane, the improvement is most pronounced with θ_{max} increase to 40° and 26° for the 10%, 20% BW cases. No scan-blindness effects are observed in both planes. Compared to the initial ridge WG element design, this design has the largest BW and the widest beam-steering sector.

Finally, Fig. 3(d) shows $|\Gamma|$ of the proposed RGW array antenna element. In this case, θ_{max} is 46° and 37° for the 10% and 20% BW requirements in the E-plane; and 32° for both 10%, 20% BW requirements in the H-plane. The overall performance is better than that of the initial ridge WG element design. However, the scan-blindness exists in both beam-steering planes for large scan angles.

When the pair of E-plane grooves is added, we can observe an unexpected beam-steering performance improvement. Fig.3(e) shows that instead of the expected improvement in the E-plane, the grooves have a major impact on the H-plane beamsteering performance: θ_{max} in the H-plane has been increased to 40° and 39° for the 10% and 20% BW cases. This interesting phenomenon is accompanied by additional H-plane $|\Gamma|$ resonances associated with the scan-blindness. This affects the element's beam-steering performance at $\leq$40° around 105 GHz. The nature of this effect is the same as for the case in Fig. 3(b) (H-plane). We believe that it is related to the surface wave propagation *along* the E-plane grooves and will be explored during future studies.

4 Bandwidth vs. Scan Range Trade-Offs

In the above analysis, we have defined the operation bandwidth by the $|\Gamma| \leq -10$ dB impedance matching criterion. In practice, this criterion can be relaxed, depending on application. Our results for the proposed RGW design with grooves [see Fig.3(e)] show that the impedance bandwidth starts to shrink when the scan angle reaches 40° in the E-plane, and 30° in the H-plane, which denotes the region of interest for the trade-off analysis. We analyzed $|\Gamma|$ by sweeping the scanning angles in both planes with the bandwidth varying from 5% to 25%. A set of cumulative distribution functions (CDFs) are plotted, as shown in Fig. 4. The CDF is defined as $CDF(x) = P(|\Gamma| \leq x)$, where P denotes the probability function. Simulated results of ridge WG array element with E- and H-plane grooves are introduced here for a more complete

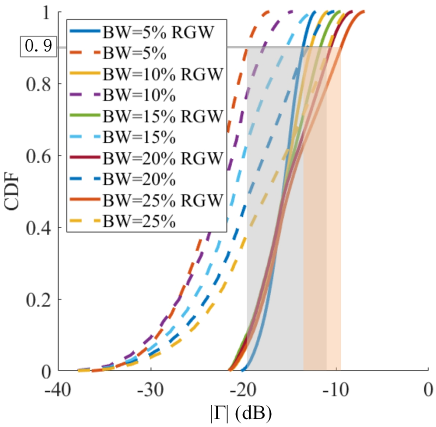

(a) 30–40° scan range, E-plane

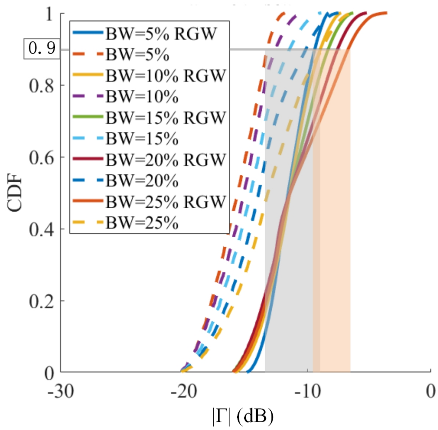

(b) 40–50° scan range, E-plane

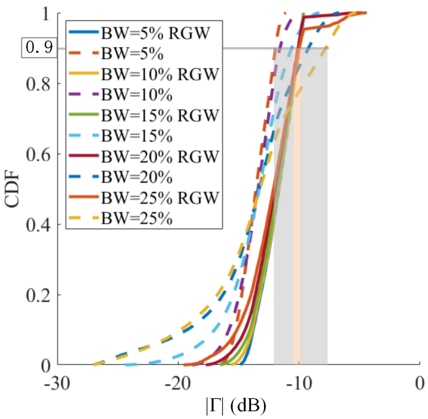

(c) 30–40° scan range, H-plane

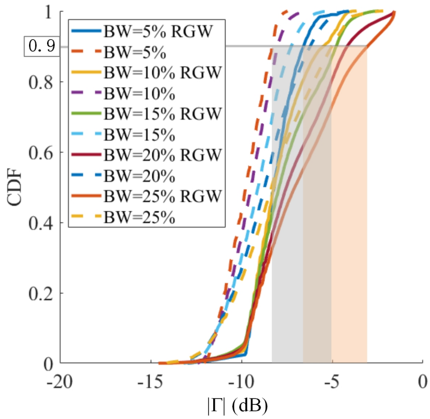

(d) 40–50° scan range, H-plane

Figure 4: Bandwidth vs. scan range trade-off study results for the following design cases: (i) the RGW antenna element with E-plane grooves (solid lines) and (ii) the ridge WG antenna element with the E- and H-plane grooves (dash lines). CDF is cumulative distribution function.

comparison.

In the E-plane, both array elements have $\geq$ 90% of $|\Gamma|$ points (CDF $\geq$ 90%) below -10 dB for the 25% BW and 30–40° scan range. When the scan angle increases to 40–50°, the ridge WG array element with the E- and H-plane grooves exhibits better impedance matching with CDF = 90% within 25% BW, as compared to 10% bandwidth of the RGW element. If a $|\Gamma| \leq -7$ dB requirement is acceptable, the bandwidth of the RGW element can be increased to 25%. In the H-plane, the RGW configuration has a wider bandwidth for 30–40° scan range: 90% RGW element's $|\Gamma|$ points fulfill $|\Gamma| \leq -10$ dB reaching 25% BW, and the ridge WG array bandwidth is only 15%. For the scan range of 40–50°, if we select the $|\Gamma| \leq -7$ dB criterion for CDF = 90%, the RGW and WG element designs have 5% and 20% BW, respectively.

In summary, the RGW array element has demonstrated promising beam-steering performance, where up to 25% impedance bandwidth (which is defined for the 90% CDF level for $|\Gamma| \leq -10$ dB) is achieved over the scan range of $\pm 40°$ in both E- and H-planes. A wider scan range of $\pm 50°$ is possible for a relaxed criterion of $|\Gamma| \leq -7$ dB. The RGW element with the grooves outperforms the initial ridge WG array element design with the E- and H- plane grooves for the H-plane scanning scenario, though at the cost of the reduced performance in the E-plane. Nonetheless, in overall, the RGW structure has an important advantage of enabling contactless transition to active electronics while being also less prone to manufacturing and assembling errors that are critical at W-band or higher frequencies.

5 Conclusion

We have considered several possible implementations of array antenna elements for future B5G communication systems at W- and D-band frequencies. These designs are based on the open-ended ridge or ridge gap WG elements, which are capable of simultaneously providing wideband and wide-angle array beam-steering performance with high radiation efficiency. The full-wave simulation results reveal two best element configurations, among the considered ones, where we have introduced decoupling grooves in the WG aperture (namely, the ridge WG element with the E- and H-plane grooves and the RGW element with the E-plane grooves). The best RGW element design is capable of realizing $\pm 40°$ scan range in both E- and H-planes within the 25%

bandwidth ($|\Gamma| \leq -10$ dB). This promising beam-steering capability, along with possible contactless RGW interface towards active electronics, makes this RGW array element a suitable candidate for future 100+GHz electronically scanned array antennas. The experimental study of the proposed antenna concepts is on-going and will be demonstrated through a finite array fragment characterization.

A further improvement of beam-steering performance could be achieved applying more effective elements decoupling techniques, especially in the H-plane. This is a subject of the future research.

Acknowledgment

This work has received funding from the European Union's Horizon 2020 research and innovation programme under the Marie Skłodowska-Curie grant agreement No 860023 (for the contributions by Y. Zhang and A.R. Vilenskiy) and the Sweden-Taiwan Collaborative Research Framework Project "Antenna Technologies for Beyond-5G Wireless Communication" from the Swedish Foundation for Strategic Research's (for the contribution by M. Ivashina).

References

[1] Z. W. Miao, Z. C. Hao, G. Q. Luo, *et al.*, "140 GHz high-gain ltcc-integrated transmit-array antenna using a wideband siw aperture-coupling phase delay structure," vol. 66, no. 1, pp. 182–190, 2018, ISSN: 0018926X.

[2] D. Kim, J. Hirokawa, M. Ando, J. Takeuchi, and A. Hirata, "64×64-element and 32×32-element slot array antennas using double-layer hollow-waveguide corporate-feed in the 120 GHz band," vol. 62, no. 3, pp. 1507–1512, 2014.

[3] S. S. Yao and Y. J. Cheng, "W-band high-efficiency wideband planar array antenna based on mems micromachining technology," in *2018 48th European Microwave Conference (EuMC)*, IEEE, 2018, pp. 942–945.

[4] A. Gomez-Torrent, M. Garcia-Vigueras, L. Le Coq, *et al.*, "A low-profile and high-gain frequency beam steering subterahertz antenna enabled by silicon micromachining," vol. 68, no. 2, pp. 672–682, 2020.

[5] A. B. Numan, J.-F. Frigon, and J.-J. Laurin, "Printed W-band multi-beam antenna with luneburg lens-based beamforming network," vol. 66, no. 10, pp. 5614–5619, 2018.

[6] U. Kodak, B. Rupakula, S. Zihir, and G. M. Rebeiz, "60- GHz 64-and 256-element dual-polarized dual-beam wafer-scale phased-array transceivers with reticle-to-reticle stitching," 2020.

[7] A. Aljarosha, A. U. Zaman, and R. Maaskant, "A wideband contactless and bondwire-free mmic to waveguide transition," vol. 27, no. 5, pp. 437–439, 2017.

[8] M. K. Leino, R. Montoya Moreno, J. Ala-Laurinaho, R. Valkonen, and V. Viikari, "Waveguide-based phased array with integrated element-specific electronics for 28 GHz," *IEEE Access*, vol. 7, pp. 90 045–90 054, 2019, ISSN: 21693536.

[9] Y. Rong and K. A. Zaki, "Characteristics of generalized rectangular and circular ridge waveguides," vol. 48, no. 2, pp. 258–265, 2000.

[10] J. Montgomery, "Ridged waveguide phased array elements," vol. AP-24, no. 1, pp. 46–53, 1976.

[11] S. Wand and A. Hessel, "Aperture performance of a double-ridge rectangular waveguide in a phased array," vol. AP-26, no. 2, pp. 204–214, 1978.

[12] A. K. Bhattacharyya, *Phased array antennas: Floquet analysis, synthesis, BFNs and active array systems.* John Wiley & Sons, 2006, vol. 179.

[13] P.-S. Kildal, A. A. Kishk, and S. Maci, "Special issue on artificial magnetic conductors, soft/hard surfaces, and other complex surfaces," vol. 53, no. 1, pp. 2–7, 2005.

[14] A. U. Zaman and P.-S. Kidal, "Gap waveguide in handbook of antenna technologies," in New York, NY: Springer Science+ Business Media Singapore, 2015, p. 464.

PAPER B

Wideband Open-Ended Ridge Gap Waveguide Antenna Elements for 1-D and 2-D Wide-Angle Scanning Phased Arrays at 100 GHz

Y. Zhang, A. R. Vilenskiy, M. V. Ivashina

IEEE Antennas and Wireless Propagation Letters
vol. 21, no: 5, pp. 883 - 887, 2022
©IEEE DOI: 10.1109/LAWP.2022.3150595

The layout has been revised.

Abstract

A new antenna element type based on the open-ended ridge gap waveguide (RGW) is proposed for phased array applications. This element type is of a particular interest at high mm-wave frequencies (≥ 100 GHz) owing to a contactless design alleviating active beam-steering electronics integration. The key challenge addressed here is a realization of a wide fractional bandwidth and scan range with high radiation efficiency. We demonstrate a relatively simple wideband impedance matching network comprised of an aperture stepped ridge segment and a single-pin RGW section. Furthermore, the E- and H-plane grooves are added that effectively suppress antenna elements mutual coupling. Results demonstrate a wide-angle beam steering ($\geq 50°$) over $\geq 20\%$ fractional bandwidth at W-band with $\geq 89\%$ radiation efficiency that significantly outperforms existing solutions at these frequencies. An experimental prototype of a 1×19 W-band array validates the proposed design concept through the embedded element pattern measurements.

1 Introduction

The future wireless communication beyond 5G holds the promise to reach Tbps level throughput at distances ≥ 1 km with flexible user mobility [1]. The upper millimeter-wave (mm-wave) bands (100+ GHz), especially W- and D-band, are being widely considered for these applications, owing to the wide available bandwidth, a relatively low atmospheric attenuation, and cm-level positioning accuracy [2]. In this context, high-gain mm-wave antenna systems with intelligent beamforming are seen as the key technological enablers, capable to compensate the considerable free-space path loss at these frequencies, while supporting spatial multiplexing, and users tracking. This drives the research in 100+ GHz phased array antennas with electronic beam steering that can provide a broad coverage and high energy efficiency [3].

A popular choice of W/D-band array antennas employs Antenna-on-Chip (AoC) and Antenna-in-Package (AiP) technologies which have been realized

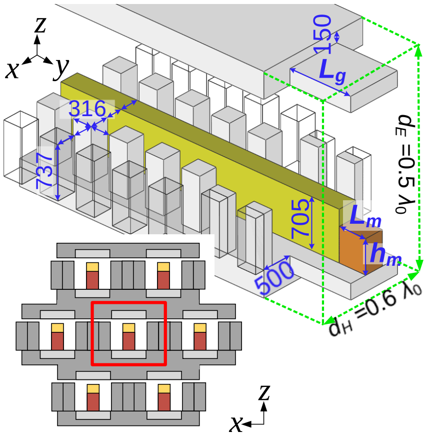

(a)

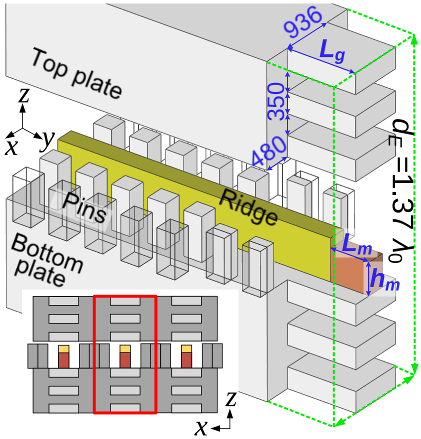

(b)

Figure 1: The proposed open-ended RGW element designs for (a) 2-D array (isosceles triangular grid) and (b) 1-D array. The components of the adjacent elements in the H-plane are shown semi-transparent (unit: μm).

using quartz substrates [4] or multilayer packages [5], [6]. However, these designs exhibit a relatively narrow bandwidth ($\leq$ 10%) and low radiation efficiency ($\leq$ 40%), along with a limited beam-steering range ($\leq 30°$), mainly due to high material loss and surface wave effects. An alternative approach is 3-D antenna configurations, using quasi-optical structures (e.g., Luneburg lens [7]) to extend the coverage, at the cost of a bulky design. Another wideband solution is dielectric rod arrays with liquid crystal-based phase control [8]; its drawback is a relatively small beam-steering range and complicated assembly.

More recently, full-metal planar array antenna designs have been investigated at W- and D-band [9]–[14]. Realization of electronic beam steering in this case is considerably more challenging than for AoC, AiP, and lens arrays. The reason is too small physical space available to integrate phase-shifting circuitry in each array element at such high frequencies. As the result, most reported arrays have been designed for fixed-beam scenarios, or as frequency beam-steering arrays [13], [14].

Therefore, we propose a new antenna element type based on the open-ended ridge gap waveguide (RGW) that aims to overcome the above-mentioned limitations. The starting point of this design is a traditional ridge waveguide (WG) element which has been widely used in arrays at microwave frequencies [15],

[16]. However, at high mm-wave frequencies, these hollow metal designs are rare due to the increased manufacturing complexity and the above-explained difficulties of electronics integration. On the other hand, the relatively new gap waveguide technology [17], realizing contactless WGs in a bed of nails, can be effectively utilized to resolve these problems. The concept of such an element has been introduced in [18], albeit without a design optimization strategy and no practical implementation considerations. The present work fills in this knowledge gap by providing a detailed element design and its experimental demonstration. This results in two W-band element examples, one of which can be used in 1-D linear arrays and another in 2-D arrays (Fig. 1), both with competitive performance characteristics in terms of high efficiency over a wide scan range and wide bandwidth.

2 Open-Ended RGW Array Elements: Design and Beam-Steering Performance

In this research, all array elements are based on a regular RGW [19] as depicted in Fig. 1. The RGW employs a single ridge with two rows of pins on each side. The following main design dimension are used: ridge height 705 μm, width 316 μm; pins height 737 μm, width 316 μm; the gap between the pins and the separation between the pins and the ridge is 316 μm; the air gap between the ridge and the top metal plate is 137 μm. Thus, the element H-plane (xy-plane, Fig. 1) size $d_H = 0.6\lambda_0 = 1896$ μm, where λ_0 is the free-space wavelength at the central design frequency $f_0 = 95$ GHz. A single quasi-TEM mode operation regime spans the $80 - 160$ GHz band. Design material is aluminum. In all simulations, the 0.5-μm Groisse surface roughness model is used. A detailed characterization of this RGW can be found in [20].

2.1 2-D Array RGW Element

A design of the proposed RGW element for a 2-D array is detailed in Fig. 1(a). As seen, the basic RGW is terminated in the open-ended manner that couples the propagating RGW wave to free space. A structure comprised of a stepped ridge segment (length L_m and height h_m) and a single-pin RGW section realizes a broadband impedance match and is discussed below. In the H-plane, multiple array elements are manufactured on a common metal plate being

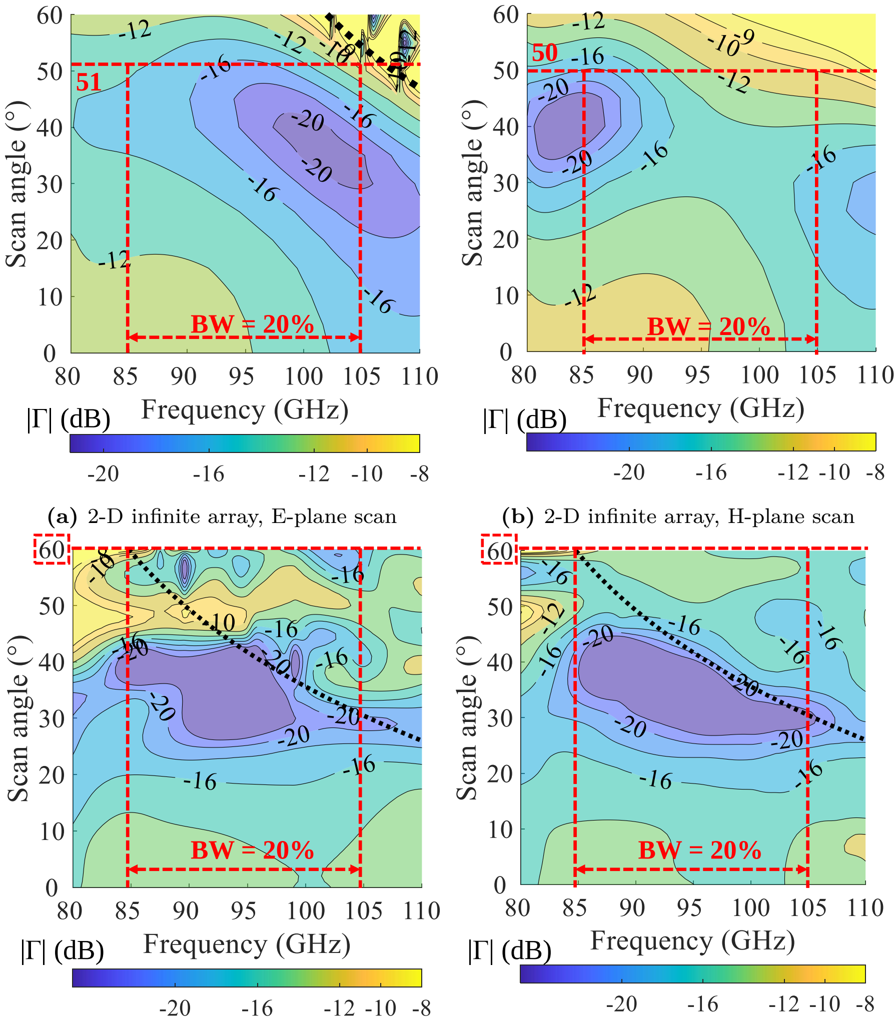

(a) 2-D infinite array, E-plane scan

(b) 2-D infinite array, H-plane scan

(c) 1-D infinite array, H-plane scan

(d) 1-D 1×19 array, H-plane scan

Figure 2: Simulated active reflection coefficient (Γ) maps for the RGW element of the 2-D infinite, 1-D infinite, and 1-D finite (1×19) arrays.

separated by the pins. By stacking such sub-arrays in the E-plane (yz-plane) the full 2-D array is constructed. Active beam-steering electronics can be integrated in a top metal plate of each RGW and contactlessly coupled to the ridge employing an E-plane WG bifurcation [21]. That creates an important design advantage of such element at high mm-wave frequencies. The considered 2-D array elements are arranged in an isosceles triangular lattice. The E-plane element size is $d_E = 0.5\lambda_0 = 1576$ μm.

The full-wave element model was built in Ansys HFSS using the 2-D infinite array approach with sidewalls periodic boundary conditions (PBC) and a Floquet port at 10-mm distance above the aperture. Compared with the initial design presented in [18], the RGW element has been further modified in this study. Apart from E-plane grooves used above and below the ridge [Fig.1(a)], H-plane grooves have been formed by removing the metal on both sides of the ridge. The resulting width of the E- and H-plane grooves is 300 μm and 1000 μm, respectively, while the depth is L_g. This way, the output RGW section transforms into the ridge WG without sidewalls. As shown below, this measure further reduced the H-plane elements mutual coupling.

The element's design parameters L_m, h_m, and L_g have been optimized to achieve a maximum scanning range in the 20% relative bandwidth (85–105 GHz), as defined by the active reflection coefficient $|\Gamma| \leq -10$ dB criterion. Fig. 3 consistently explains the impedance matching mechanism utilizing a simplified equivalent circuit representation:

1. As seen in Fig. 3(a), the open-ended ridge WG fails to achieve a good impedance match. This is largely due to an excessive shunting edge capacitance of the ridge C_{OE}.

2. The high-impedance (Z_{m1}) stepped ridge segment [Fig. 3(b)] realizes (i) a C_{OE} reduction to C^*_{OE} and (ii) an impedance transformation, while adding an equivalent E-plane ridge step capacitance C_E. As a result, Γ curves are effectively shifted to the center of the Smith chart.

3. Finally, the low-impedance (Z_{m2}) single-pin section [Fig. 3(c)] locates all Γ curves well inside the -10-dB circle by providing a fine impedance transformation and adding an inductance L_{H2} of the H-plane sidewalls step.

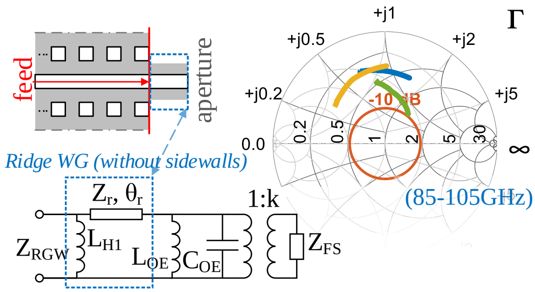

(a) No matching circuit

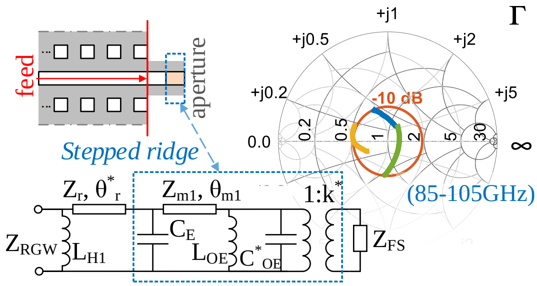

(b) Stepped ridge segment

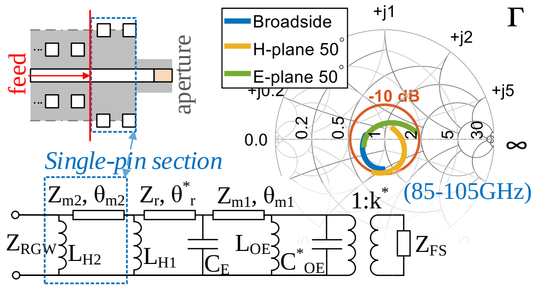

(c) Stepped ridge + single-pin section

Figure 3: Impedance matching mechanism of the RGW element, represented by equivalent circuits. Open-ended RGW aperture parameters (beam steering-dependent): Z_{FS} is the free-space impedance, $k^{(*)}$, $C_{OE}^{(*)}$, and L_{OE} are the equivalent transformer turn ratio, capacitance, and inductance with (*) and without the stepped ridge, respectively. Matching circuit parameters: $(Z_r, \theta_r^{(*)})$, (Z_{m1}, θ_{m1}), and (Z_{m2}, θ_{m2}) are the characteristic impedance and electrical length of the output ridge WG, stepped ridge, and single-pin segments; C_E and $L_{H1,2}$ are the equivalent capacitance and inductance of the E-plane ridge and H-plane pin sidewalls steps.

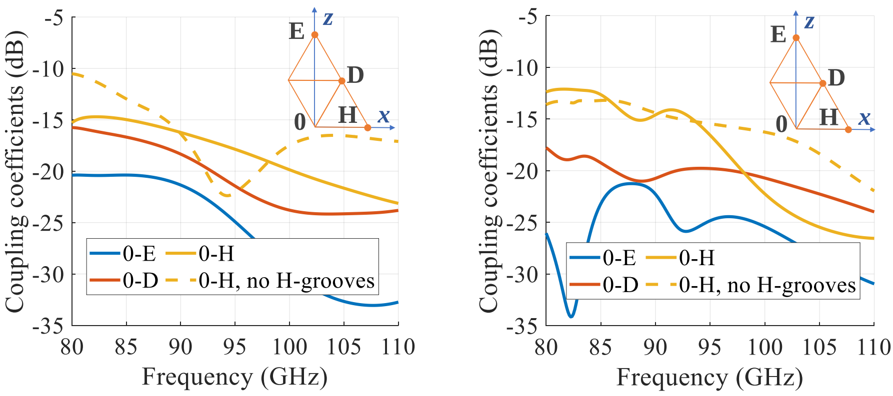

(a) (b)

Figure 4: Mutual coupling levels between the central ("0") and adjacent elements in E-/D-/H-planes in (a) RGW array; (b) ridge WG array .

The final optimized design parameters are $L_m = 466$ μm, $h_m = 480$ μm, $L_g = 1060$ μm. The resulting beam-steering performance is demonstrated in Figs. 2(a), 2(b). For the 20% bandwidth the beam-steering range is $\pm 51°$ and $\pm 50°$ in the E-and H-plane, respectively. In the E-plane, at higher-frequencies, the scan range is limited by the grating-lobe border (black dashed curves in Fig. 2). Here, the element also experiences the scan blindness. On the other hand, in the H-plane, we observe no scan blindness in contrast to the RGW element design from [18]. The elimination of this phenomenon is attributed to the E- and H-plane grooves that effectively create an aperture quasi-periodic electromagnetic soft surface [22] [see the inset in Fig. 1(a)]. Fig. 4 demonstrates realized mutual coupling levels between the central and three adjacent elements for the proposed and ridge WG array from [18]. Both arrays show quite similar coupling performance that proves the similarity of electromagnetic processes in the open-ended elements. For comparison, simulated results in the H-plane are also given for the elements without H-plane grooves (dashed curves). For the grooved designs, we observe the expected high-frequency H-plane mutual coupling suppression by up to 7 dB, which greatly improves the scan range. Inside the beam-steering range, the simulated element radiation efficiency is $> 95\%$; the relative cross-polarization level is below -60 dB and -17 dB in the E- and H-plane, respectively.

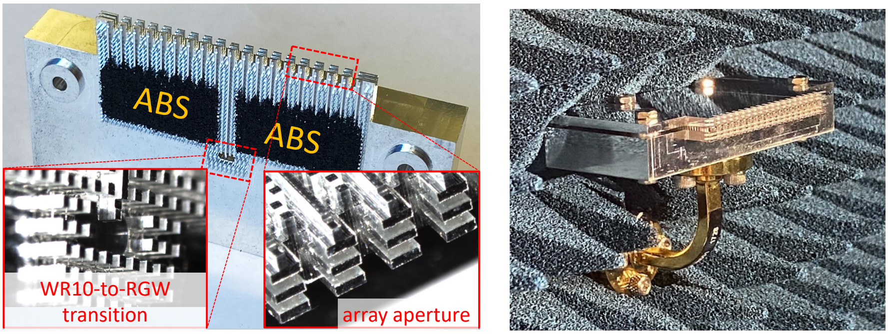

(a) (b)

Figure 5: (a) Photograph of the manufactured 1-D open-ended RGW array (top plate removed) and (b) the antenna in the CATR measurement setup.

2.2 1-D Array RGW Element

A linear array design is of practical interest as a building block (sub-array) of the 2-D array antenna. Furthermore, mm-wave 1-D beam-steering arrays have found their application for the indoor communication [23] and automotive radar systems [24]. In these cases, the proposed open-ended RGW element concept can be readily utilized. The 1-D element structure is detailed in Fig. 1(b). As seen, the design has been, in general, inherited from the 2-D array element. The main discrepancy is the two-groove structure formed in the E-plane. The resulting aperture electromagnetic soft surface [see the inset in Fig. 1(b)] allows to predictably terminate and stop the leakage of electrical currents to the outer surfaces of the top and bottom metal plates. To be consistent with the previous 2-D array element design, we have used $d_H = 0.6\lambda_0$.

Again, the 1-D element design has been optimized with the maximum scan range criterion (Section 2.1). A full-wave HFSS simulation model with the H-plane PBC and perfect matched layers (along y- and z-axis) has been employed for this purpose. The final design parameters are $L_m = 676$ μm, $h_m = 539$ μm, $L_g = 1200$ μm. The simulated $|\Gamma|$ map is presented in Fig. 2(c). The 1-D element demonstrates a wideband impedance matching performance with $|\Gamma| \leq -10$ dB. The grating-lobe border limits the scan range for some applications. However, this can be easily compensated by decreasing d_H.

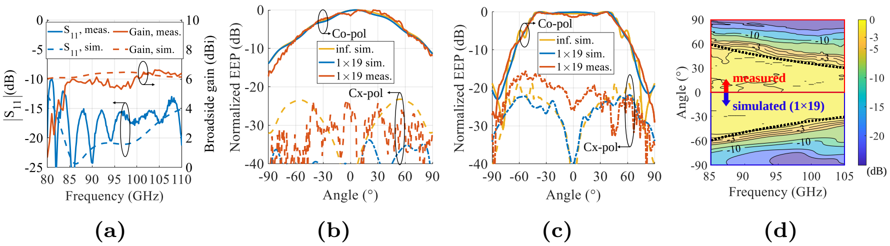

Figure 6: Simulated and measured performance of the 1-D array RGW element: (a) reflection coefficient (S_{11}) and broadside realized gain; (b) E-plane and (c) H-plane normalized embedded element patterns (EEPs) at 95 GHz; (d) H-plane co-polarized frequency-angle 2-D EEP maps (the dashed black lines indicate the grating-lobe border).

3 Experimental Study of the 1-D Array Element

At this research stage, the first prototype of the 1-D array has been designed for the experimental characterization to verify the predicted RGW element scan performance, as well as to test a manufacturing technology and assembling tolerances. The 1×19 1-D array (Fig. 5) has been fabricated using a CNC milling process. This array size was found sufficient to reconstruct the infinite array environment as supported by results in Fig. 2(d) demonstrating simulated $|\Gamma|$ of the central array element [*cf.* Fig. 2(c)]. Since the standard WR-10 interface flange is much larger than d_H, measuring the full array S-matrix (to compute Γ) is practically not possible. Therefore, the beam-steering performance of the element was characterized through embedded element pattern (EEP) measurements [25]. To realize this, the central array element was excited using a WR10-to-RGW orthogonal transition [17] [Fig. 5(a)], while all neighboring elements were terminated with matched loads. The loads were made of carbon-loaded absorbing foam (ABS) WAVASORB FS from Emerson & Cuming [20].

Table 1: Performance comparison of reported array elements at high mm-wave frequency bands.

Array element type		**Implementation technology**	**Freq. range (GHz)** ($\|\Gamma\| \leq$-10 dB)	**Element size (λ_0^2)**	**Radiation efficiency (%)**	**Scan range / scan loss**
[6]	Planar stacked patch	AiP	88-94, 7%	0.49×0.49	N/A	±32° (E/H-plane) / NA
[4]	Planar dif.-fed dipole	AoC (quartz)	108-114, 5%	0.5×0.5	45	±30° (E/H-plane) / ≤ 2.5 dB
[13]	Leaky-wave slot WG	Si micromachining (gold)	220-300, 30%	0.49×0.35	79 (full antenna)	–75° to –30° (E-plane) / NA
[8]	Dielectric rod	Milled Rexolite assembly	75-110, 38%	0.86×0.86	N/A	–25° to 15° (E-plane, 85 GHz) / ≤2.5 dB
This work	Open-ended RGW: **1-D**	Full-metal (aluminum), contactless	85-105, 21%	1.37×0.6	≥ 91	±40° (H-plane) / ≤ 3 dB
	2-D		85-105, 21%	0.5×0.6	≥ 89	±51°/±50° (E/H-plane) / ≤2.5 dB

Element performance was measured at the WR-10 input flange in the compact antenna test range (CATR) setup of Chalmers THz antenna chamber [Fig. 5(b)]. The measured central element passive reflection coefficient (S_{11}) and the broadside realized element gain are given in Fig. 6(a) in comparison with the simulated curves. An additional insertion loss ($\sim$0.7 dB) of the WR10-to-RGW transition and an RGW feed line has been extracted from back-to-back structure measurements and excluded from the measured gain results. Some frequency ripples are observed for both S_{11} and gain measured curves. The ripples are attributed to relatively high manufacturing errors ($\leq 20\ \mu$m) of the stepped ridge height in the transition and aperture areas. Moreover, the realized gain is affected by imperfect ABS loads performance (average reflection coefficient $\sim$17 dB [20]). The experimental embedded element radiation efficiency was estimated to be $\geq 91\%$, considering simulated values of $\geq 97\%$ and an average measured gain loss of 0.3 dB. Simulated (for both the 1×19 array and the 1-D infinite array model) and measured normalized EEPs at 95 GHz are compared in Figs. 6(b), 6(c) for the E- and H-plane, respectively. A small ($\sim$1 dB) H-plane broadside dip, observed for the measured pattern, is due to the above-mentioned non-zero reflections in the ABS-terminated channels. The measured cross-polarized EEP is slightly asymmetrical that is, likely, attributed to the measurement setup. Fig. 6(d) depicts the frequency-angle 2-D co-polarized EEP maps in the H-plane revealing a wide-angle flat-top EEP shape. Array edge effects have been studied in simulations, from which we can conclude that already for the second edge element the EEP shape in the $\pm50°$ range deviates by less than 2 dB from the results in Fig. 6. Overall, simulated and measured results in the 85 – 105 GHz range are in a very good agreement, verifying the expected wideband and wide-angle RGW element beam-steering performance with low sensitivity to manufacturing and assembling tolerances.

Table 1 summarizes the beam-steering performance of the previously reported mm-wave (100+ GHz) array elements implemented in different technologies. The proposed designs outperform the state-of-the-art W- and D-band antenna solutions based on AoC, AiP, and dielectric rod arrays [4]–[6], [8], as well as leaky-wave metal antennas [13], [14] in terms of wide-angle, wideband beam-steering capabilities with high radiation efficiency. The demonstrated 2-D array element performance has been, thus far, achieved for the open-ended ridge WG elements [15] and rectangular WG elements[26] only at much lower frequency bands (L- and X-band), employing impedance-matching dielectric sheets and WG insets.

4 Conclusions and Future Work

In this letter, we have proposed the open-ended ridge gap waveguide (RGW) antenna element concept for 1- and 2-D array configurations. This RGW element is easily manufacturable from two split blocks which can be thereafter assembled contactlessly. The latter provides that the element is suitable for the integration of active electronics inside its structure to enable electronic beam steering at high mm-wave frequencies. The results of the infinite array simulation model have been verified through the experimental study of the 1-D array element. At W-band, the 2-D array element demonstrates a wide-band ($\geq 20\%$) and wide-angle ($\geq 50°$) beam-steering performance with high radiation efficiency ($\geq 89\%$, with 0.3 dB additional loss included). The future work aims at the development of a 2-D array prototype as well as at integration of phase-shifting circuitry into the element's RGW. A quasi-optical feed architecture [27] is being considered for efficient array elements excitation.

References

[1] *European vision for the 6G network ecosystem*, White Paper, The 5G Infrastructure Association, Jun. 2021.

[2] T. S. Rappaport, Y. Xing, O. Kanhere, *et al.*, "Wireless communications and applications above 100 GHz: Opportunities and challenges for 6G and beyond," *IEEE Access*, no. 7, pp. 78 729–78 757, 2019.

[3] M. V. Ivashina, A. R. Vilenskiy, H.-T. Chou, J. Oberhammer, and M. Ng Mou Kehn, " Antenna technologies for beyond-5G wireless communication: Challenges and opportunities," in *Proc. 2021 International Symposium on Antennas and Propagation (ISAP)*, Taipei, Taiwan, 2021, pp. 1–2.

[4] W. Shin, B.-H. Ku, O. Inac, Y.-C. Ou, and G. M. Rebeiz, “A 108–114 GHz 4× 4 wafer-scale phased array transmitter with high-efficiency on-chip antennas,” *IEEE Journal of Solid-State Circuits*, vol. 48, no. 9, pp. 2041–2055, 2013.

[5] S. Shahramian, M. J. Holyoak, A. Singh, and Y. Baeyens, “A fully integrated 384-element, 16-tile, W-band phased array with self-alignment and self-test,” *IEEE Journal of Solid-state Circuits*, vol. 54, no. 9, pp. 2419–2434, 2019.

[6] X. Gu, D. Liu, C. Baks, J.-O. Plouchart, W. Lee, and A. Valdes-Garcia, “An enhanced 64-element dual-polarization antenna array package for W-band communication and imaging applications,” in *Proc. 2018 IEEE 68th Electronic Components and Technology Conference (ECTC)*, 2018, pp. 197–201.

[7] S. Manafi, J. F. González, and D. Filipovic, “Design of a perforated flat luneburg lens antenna array for wideband millimeter-wave applications,” in *Proc. 2019 13th European Conference on Antennas and Propagation (EuCAP)*, 2019, pp. 1–5.

[8] R. Reese, E. Polat, H. Tesmer, *et al.*, “Liquid crystal based dielectric waveguide phase shifters for phased arrays at W-band,” *IEEE Access*, vol. 7, pp. 127 032–127 041, 2019.

[9] B. L. Cannon, K. J. Vanhille, and G. A. Sadowy, “Microfabricated dual-polarized, W-band antenna architecture for scalable line arrav feed,” in *2015 IEEE International Symposium on Antennas and Propagation & USNC/URSI National Radio Science Meeting*, 2015, pp. 615–616.

[10] S. S. Yao and Y. J. Cheng, “W-band high-efficiency wideband planar array antenna based on mems micromachining technology,” in *Proc. 2018 48th European Microwave Conference (EuMC)*, 2018, pp. 942–945.

[11] D. Kim, J. Hirokawa, M. Ando, J. Takeuchi, and A. Hirata, “64×64-element and 32×32-element slot array antennas using double-layer hollow-waveguide corporate-feed in the 120 GHz band,” vol. 62, no. 3, pp. 1507–1512, 2014.

[12] J. W. Jordan, S. Lynch, M. Clark, *et al.*, “Monolithically fabricated 4096-element, polystrata® broadband d-band array demonstrator,” in *Proc. 2019 IEEE MTT-S International Microwave Symposium (IMS)*, 2019, pp. 1060–1063.

[13] A. Gomez-Torrent, M. Garcia-Vigueras, L. Le Coq, *et al.*, "A low-profile and high-gain frequency beam steering subterahertz antenna enabled by silicon micromachining," vol. 68, no. 2, pp. 672–682, 2020.

[14] D. A. Schneider, M. Rösch, A. Tessmann, and T. Zwick, "A low-loss W-band frequency-scanning antenna for wideband multichannel radar applications," *IEEE Antennas and Wireless Propagation Letters*, vol. 18, no. 4, pp. 806–810, 2019.

[15] J. Montgomery, "Ridged waveguide phased array elements," vol. AP-24, no. 1, pp. 46–53, 1976.

[16] A. Agrawal, M. Perry, and N. Landry, "Wideband ridge waveguide radiating element for phased array antennas," in *Proc. IEEE Antennas and Propagation Society International Symposium. 1995 Digest*, vol. 1, 1995, pp. 568–571.

[17] A. U. Zaman and P.-S. Kidal, "Gap waveguide in handbook of antenna technologies," in New York, NY: Springer Science+ Business Media Singapore, 2015, p. 464.

[18] Y. Zhang, A. R. Vilenskiy, and M. V. Ivashina, "W-band waveguide antenna elements for wideband and wide-scan array antenna applications for beyond 5G," in *Proc. 2021 15th European Conference on Antennas and Propagation (EuCAP)*, 2021, pp. 1–5.

[19] P.-S. Kildal, E. Alfonso, A. Valero-Nogueira, and E. Rajo-Iglesias, "Local metamaterial-based waveguides in gaps between parallel metal plates," vol. 8, pp. 84–87, 2009.

[20] A. R. Vilenskiy, Y. Zhang, and M. V. Ivashina, "Methods for attenuating and terminating waves in ridge gap waveguide at W-band: Carbon-loaded foam, carbonyl iron paint, and nickel plating," in *Proc. 51 European Microwave Conference (EuMC)*, accepted, 2021, pp. 1–5.

[21] A. Aljarosha, A. U. Zaman, and R. Maaskant, "A wideband contactless and bondwire-free mmic to waveguide transition," *IEEE Microwave and Wireless Components Letters*, vol. 27, no. 5, pp. 437–439, 2017.

[22] P.-S. Kildal, "Definition of artificially soft and hard surfaces for electromagnetic waves," *Electronics Letters*, vol. 24, pp. 168–170, 3 Feb. 1988.

[23] W. Hong, K.-H. Baek, Y. Lee, Y. Kim, and S.-T. Ko, “Study and prototyping of practically large-scale mmWave antenna systems for 5G cellular devices,” *IEEE Communications Magazine*, vol. 52, no. 9, pp. 63–69, 2014.

[24] U. Chipengo, A. Sligar, and S. Carpenter, “High fidelity physics simulation of 128 channel mimo sensor for 77 GHz automotive radar,” *IEEE Access*, vol. 8, pp. 160 643–160 652, 2020.

[25] N. Amitay, V. Galindo, and C. P. Wu, *Theory and Analysis of Phased Array Antennas*. New York: Wiley Interscience, 1972.

[26] X. Liang, Z. Zhang, J. Zeng, F. Guan, X. Liu, and J. Zi, “Scan blindness free design of wideband wide-scanning open-ended waveguide phased array,” *IEEE Access*, vol. 9, pp. 68 127–68 138, 2021.

[27] A. R. Vilenskiy, E. Galesloot, Y. Zhang, A. Bart Smolders, and M. V. Ivashina, “Quasi-optical beamforming network for millimeter-wave electronically scanned array antennas with 1-bit phase resolution,” in *Proc. 2021 15th European Conference on Antennas and Propagation (EuCAP)*, 2021, pp. 1–5.

PAPER C

Mutual Coupling Analysis of Open-Ended Ridge and Ridge Gap Waveguide Radiating Elements in an Infinite Array Environment

Y. Zhang, A. R. Vilenskiy, M. V. Ivashina

2022 52nd European Microwave Conference (EuMC)
Milan, Italy, Sept. 2022
 DOI: 10.23919/EuMC54642.2022.9924388

The layout has been revised.

Abstract

In this paper, we discuss mutual coupling effects in 2-D beam-steerable antenna arrays based on open-ended ridge and ridge gap waveguide radiating elements. Considering potential applications for beyond-5G systems in W-/D-band, the radiating elements are designed full-metal realizing a high radiation efficiency. Various decoupling structures based on electromagnetic soft surfaces are applied to suppress the surface waves over the array apertures. The infinite array approach is used to analyze antenna unit cells in an isosceles triangular lattice, which results in the active reflection coefficient over a scan and frequency range. The latter is used to extract the values of the mutual coupling coefficients between the elements. The analysis demonstrates the effect of decoupling structures realizing a steep drop of the mutual coupling magnitude (≤ -20 dB) for closely-spaced array elements. This results in a wideband ($\geq 20\%$) and wide-scan ($\geq 50^o$) element beam-steering performance.

1 Introduction

While beyond-5G future wireless communication proposes the W- (75-110 GHz) and D-band (110-170 GHz) as the promising operating frequency range, owing to a relatively low atmospheric absorption loss and centimeter-level positioning accuracy [1], [2], the study in phased array antennas (PAAs) for 100+ GHz is increasing in demand facing various technological challenges. To compensate for an increased material dissipation and free-space path loss at these frequencies, such PAA designs are required to be high-gain and high-efficient with wide-angle scanning capabilities.

State-of-the-art solutions mainly adopted Antenna-On-Chip (AoC) and System-in-Package (SiP) implementations to realize scalable active PAAs [3], [4]. However, at least 30-40% of radiation efficiency is typically lost due to high material loss. On the other hand, W-/D-band full-metal PAAs have been proposed recently demonstrating higher radiation efficiency ($\geq 50\%$) and potential wide-scan ability [5]–[7]. More recently, we have demonstrated several full-metal PAAs based on the open-ended *ridge gap waveguide* (RGW) [8], [9]. In general, open-ended *ridge waveguide* (WG) PAAs have been widely applied for microwave frequency radar applications [10]. However, their hollow metal structure significantly increases manufacturing complexity at 100+ GHz frequencies. At the same time, the RGW-based architectures can resolve this problem owing to the inherently contactless design, with the wideband and wide-angle beam-steering performance being preserved.

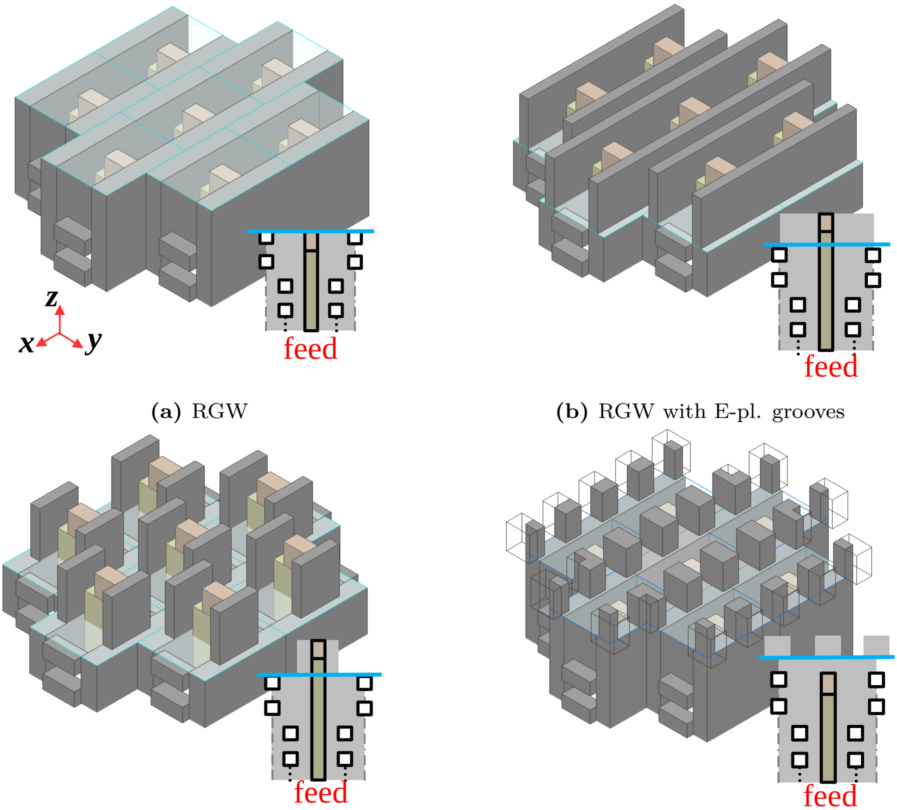

(a) RGW **(b)** RGW with E-pl. grooves

(c) RGW with E- & H-pl. grooves **(d)** RGW with AMC pins

Figure 1: RGW array elements with various decoupling structures.

In this contribution, we further investigate the beam-steering performances of various open-ended WG and RGW array elements focusing on the elements mutual coupling analysis. In particular, we study the effects of adding fragments of electromagnetic soft surfaces (grooves, pins, and their combinations) in the array aperture that facilitates the adjacent elements decoupling and thus extends achievable beam-steering range.

2 Open-Ended WG and RGW Elements in an Infinite Array Environment

To cross-compare beam-steering capabilities and mutual coupling effects of various PAAs, the Ansys HFSS finite element method electromagnetic solver was used to analyze antenna unit cells (UCs) in the isosceles triangular array lattice with periodic boundary conditions (PBC) (details can be found in [8], [9], [11]). At the first study stage, the active reflection coefficient (Γ) was found versus frequency and scan angle for WG and RGW UCs with various decoupling structures; next, the mutual coupling coefficients of the corresponding array elements were calculated from the Γ results, where a post-processing approach is used to avoid a time-consuming simulation of a large-scale finite array fragment [12].

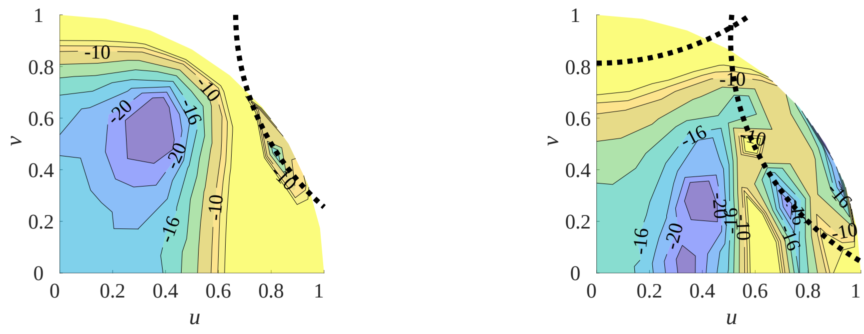

(a) $|\Gamma|$ at 95 GHz, RGW

(b) $|\Gamma|$ at 105 GHz, RGW

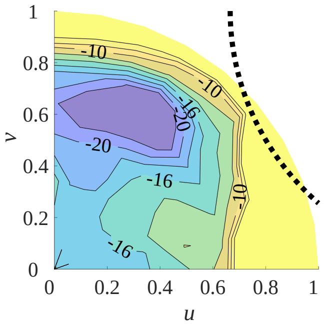

(c) $|\Gamma|$ at 95 GHz, RGW + E-gr.

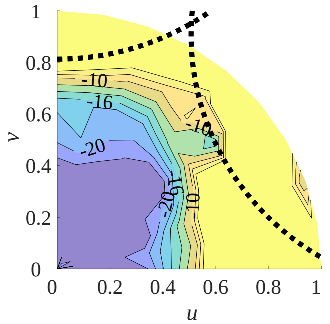

(d) $|\Gamma|$ at 105 GHz, RGW + E-gr.

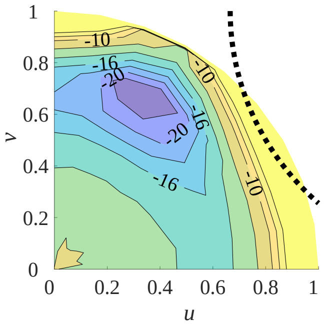

(e) $|\Gamma|$ at 95 GHz, RGW + E-/H-gr.

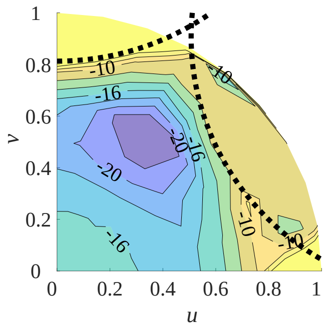

(f) $|\Gamma|$ at 105 GHz, RGW + E-/H-gr.

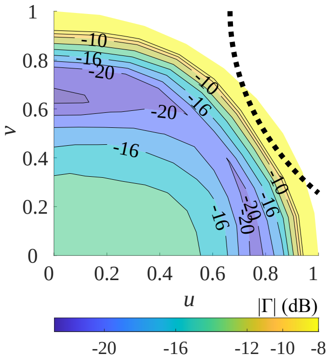

(g) $|\Gamma|$ at 95 GHz, RGW + AMC pins

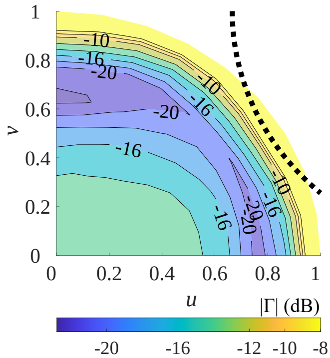

(h) $|\Gamma|$ at 105 GHz, RGW + AMC pins

Figure 2: Simulated active reflection coefficient (Γ) maps for the RGW elements with different decoupling aperture structures. Black dashed lines show grating lobe borders due to Floquet high-order modes ($m = -1, n = -1$ and $m = 0, n = -1$) propagation.

Table 1: Comparison of θ_{max} for various array elements, $|\Gamma| \leq -10$ dB over the 20% relative bandwidth (85–105 GHz) criterion.

	$\pm\theta_{max}$, **E-plane**	$\pm\theta_{max}$, **H-plane**
WG	$\pm 37°$	$\pm 17°$
RGW	$\pm 31°$	$\pm 39°$
WG + E-pl. grooves	$\pm 37°$	$\pm 28°$
RGW + E-pl. grooves	$\pm 47°$	$\pm 33°$
WG + E-/H-pl. grooves	$\pm 41°$	$\pm 26°$
RGW + E-/H-pl. grooves	$\pm 51°$	$\pm 50°$
RGW + AMC pins	$\pm 51°$	$\pm 60°$

2.1 Optimization of the Beam-Steering Performance

The considered UCs include open-ended WG and RGW structures with variations of decoupling structures. The basic design concepts and some results were discussed in [8], [9]. In general, UCs were optimized to reach the largest beam-steering elevation angle (θ_{max}) through the criterion of $|\Gamma| \leq -10$ dB over the 20% relative bandwidth (85–105 GHz). The full-wave simulation results are summarized in Table. 1. Various configurations of the RGW array element are demonstrated in Fig.1, where the decoupling structures include E- and H-plane grooves (E- and H-plane are yz- and xz-plane, respectively) [8],[9] [Fig.1(b),1(c)], and a bed of pins protruding over the UC aperture. The pins parameters are tuned to get the artificial magnetic conductor (AMC) surface response [see Fig.1(d)]. This way, the AMC structure realizes the surface wave bandgap region, i.e., a 2-D electromagnetic soft surface [13]. This technique has been widely used to suppress mutual coupling in wide-angle scanning printed PAAs [14]. The blue reference planes in Fig. 1 show where the decoupling structures start along z-axis. A detailed design description of the WG arrays can be found in [8].

Referring to Table 1, we can see that the standard WG UCs in the H-plane are limited by $\theta_{max} \leq 30°$ even with E-/H-plane grooves in the aperture, while the RGW UCs here typically demonstrate larger θ_{max} ($\geq 50°$). This is owing to a higher elements decoupling in both D- and H-plane of the RGW arrays (see below).

To further understand how the beam-steering performance is affected by various RGW element aperture modifications, in Fig. 2, we plotted $|\Gamma|$ maps in the full visible scan range for two selected frequencies. These results are

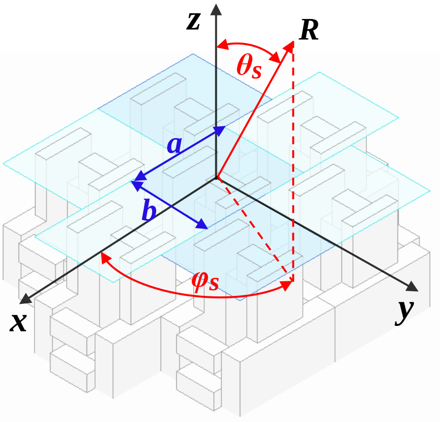

(a)

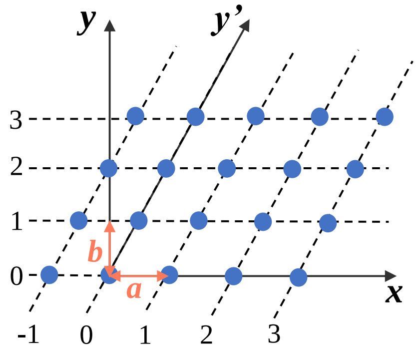

(b)

Figure 3: (a) The open-ended waveguide unit cell (the RGW element with E- [xz-plane] and H-plane [yz-plane] grooves is shown) in the array environment and (b) array isosceles triangular lattice configuration.

discussed in connection with the post-processed mutual coupling coefficients in the following subsection.

2.2 Mutual Coupling Analysis

A general view of the UC inside an infinite isosceles triangular array lattice is depicted in Fig. 3(a). The lattice geometry is shown in Fig. 3(b) with the reference element placed at the (0,0)-position. Here, the distances a and b represent the inter-element spacings in the H- and E-plane ($0.6\lambda_0$ and $0.5\lambda_0$, λ_0 – free-space wavelength at 95 GHz) respectively, which are the common parameters for all above-discussed UC designs. The array mutual coupling coefficients between the reference $(0,0)$- and (i,j)-element (S_{ij}) can be calculated using the 2-D Fourier series expansion of Γ, with S_{ij} representing the (i,j)-th Fourier coefficient in the $(\Psi_x, \Psi_{y'})$ phase space, where Ψ_x and $\Psi_{y'}$ are the phase differences between adjacent elements along x- and y'-axis [Fig. 3(b)], i. e., $\Psi_x = 2\pi au/\lambda$, $\Psi_{y'} = 2\pi bv/\lambda + \Psi_x/2$ [11], [15]. Here, u and v are the scan direction cosines ($u = sin\theta_s cos\phi_s$, $v = sin\theta_s sin\phi_s$). Note that $\Psi_x, \Psi_{y'} \in [-\pi, \pi]$ that in general includes the invisible region of the (u, v)

space.

To consider both accuracy and time-efficiency, the resolution of $\Delta\Psi_x = \Delta\Psi_{y'} = 6°$ was used in numerical integration, the results of which are shown in Fig. 4.

As Fig. 4(a) and 4(b) show, the RGW UC demonstrates lower $|S_{00}|$, but slightly higher coupling with the 3rd and 4th elements in the H-plane compared with the conventional WG. For $i \geq 5$, the $|S_{i0}|$ drops faster at higher frequencies for the RGW element. Overall, this results in the larger H-plane θ_{max} of the RGW element. When E-plane grooves are added to the WG/RGW UCs, coupling magnitudes show a significant reduction in the D-plane [$y'z$-plane, Fig. 3(b)]. This is correlated with the results observed in Fig. 2(a)-2(d) where Γ for the RGW element is significantly improved in the E- and D-planes (nearby the grating lobe borders) after adding the E-plane grooves. At the same time, the coupling level increases in the H-plane for both WG and RGW elements [see Fig. 4(c) and 4(d)]. However, it is surprising that the resulting H-plane θ_{max} has different trends for these elements, as $|\theta_{max}|$ increases from 17° to 28° for the WG element, and decreases from 39° to 33° for the RGW element. This interesting phenomenon is likely the result of a specific mutual coupling destructive superposition and should be investigated further.

When both the E- and H-plane grooves are added, the mutual coupling between elements becomes well-suppressed in both principal planes [Fig. 4(e)-4(f)]. However, the RGW element demonstrates a significantly larger H-plane scan range, which is likely due to a phase relation between S_{00} and S_{i0}. The RGW element performance improves further as the AMC pins are applied over the aperture: despite that the mutual coupling magnitudes are still very close to the grooved RGW element (see Fig. 4(f)-4(g)), its $|\Gamma| \leq -10$ dB range covers almost all possible (u,v) values inside the grating-lobe-free visible region over all operating frequencies [see Fig. 2(h)]. The main improvement here is observed in the H-plane scanning range, which is the most noticeable at the high frequencies. To reveal the reason behind this, Fig. 5 gives a more comprehensive comparison of the mutual coupling magnitudes between several adjacent elements of two RGW arrays. The mutual coupling is, in general, well-suppressed for both arrays. However, we can see that in the H-plane of the AMC-loaded element the high-frequency suppression is more intense, which is the main reason for the extended H-plane scanning range.

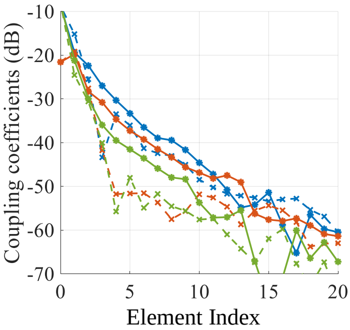

(a) WG

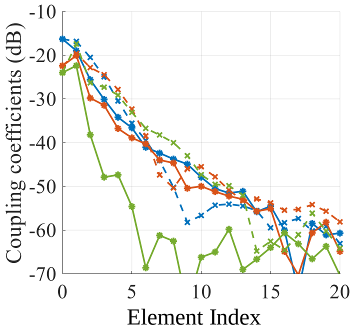

(b) RGW

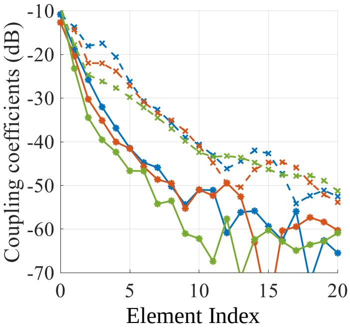

(c) WG with E-pl. grooves

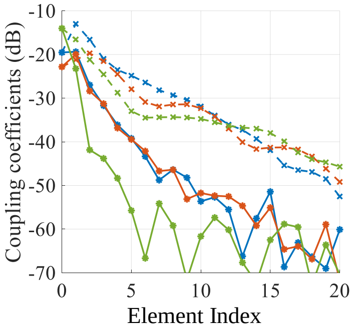

(d) RGW with E-pl. grooves

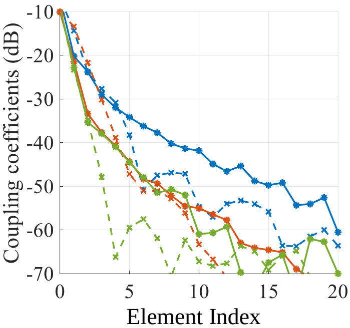

(e) WG with E-/H-pl. grooves

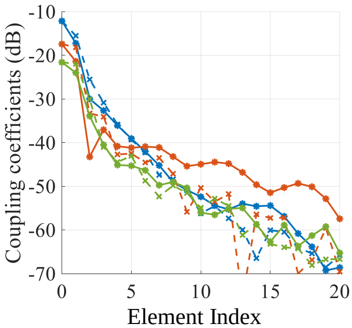

(f) RGW with E-/H-pl. grooves

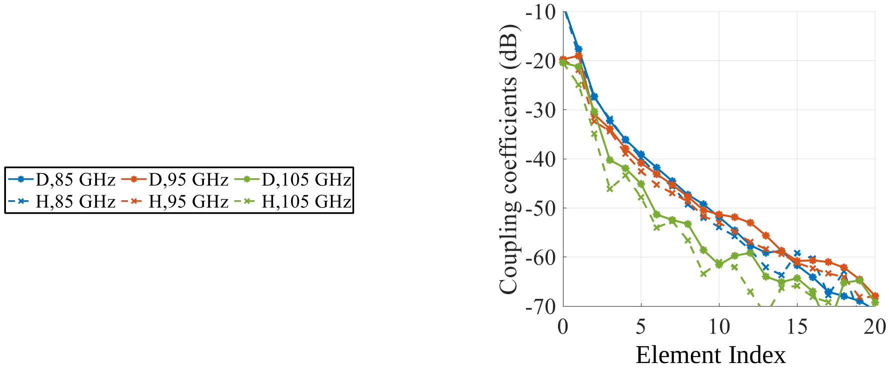

(g) RGW with AMC pins

Figure 4: Extracted coupling coefficient magnitudes in the D- and H-plane for various WG and RGW radiating elements in the infinite array environment. The elements numbering is given in Fig. 3(b).

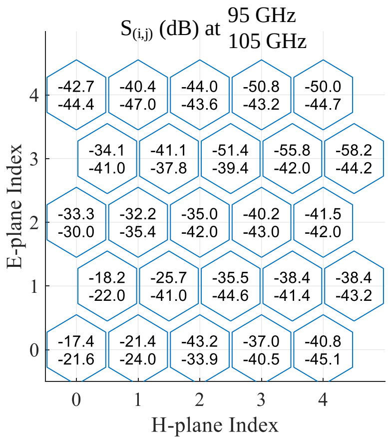

(a) RGW with E-/H-pl. grooves

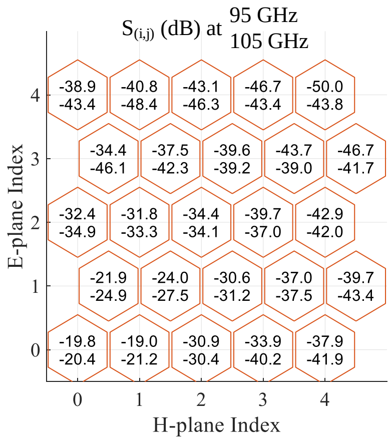

(b) RGW with AMC pins

Figure 5: Extracted coupling coefficient magnitude maps for the central (0,0) and neighboring (i,j) RGW elements in the infinite array environment at 95 and 105 GHz.

3 Conclusion

In this paper, we analyzed the beam-steering performance of the open-ended ridge waveguide (WG) and ridge gap waveguide (RGW) array elements with the thorough investigation of the elements mutual coupling effects. Various decoupling structures were proposed to suppress the mutual coupling magnitude. The results evidence that the RGW elements with the grooved aperture perform larger H-plane scan angles ($\pm 50°$) over a relatively wide band ($\geq 20\%$) as compared with the conventional grooved WG elements. The latter improvement is not obvious since the H-plane coupling magnitudes for both element types are quite close. Therefore, it is believed that coupling phases could significantly contribute to the observed effect. Moreover, by adding the artificial magnetic conductor pins above the RGW element aperture, the further suppression of the mutual coupling level can be achieved that allows for the superior beam-steering range of $\pm 51°$ / $\pm 60°$ in the E- / H-plane over the $\geq 20\%$ (85-105 GHz) frequency bandwidth.

Acknowledgment

This work has received funding from the European Union's Horizon 2020 research and innovation programme under the Marie Skłodowska-Curie grant agreement No 860023 and the Sweden-Taiwan Collaborative Research Framework Project "Antenna Technologies for Beyond-5G Wireless Communication" from the Swedish Foundation for Strategic Research.

References

[1] T. S. Rappaport, Y. Xing, O. Kanhere, *et al.*, "Wireless communications and applications above 100 GHz: Opportunities and challenges for 6G and beyond," *IEEE Access*, no. 7, pp. 78 729–78 757, 2019.

[2] *European vision for the 6G network ecosystem*, White Paper, The 5G Infrastructure Association, Jun. 2021.

[3] W. Shin, B.-H. Ku, O. Inac, Y.-C. Ou, and G. M. Rebeiz, "A 108–114 GHz 4× 4 wafer-scale phased array transmitter with high-efficiency on-chip antennas," *IEEE Journal of Solid-State Circuits*, vol. 48, no. 9, pp. 2041–2055, 2013.

[4] X. Gu, D. Liu, C. Baks, J.-O. Plouchart, W. Lee, and A. Valdes-Garcia, "An enhanced 64-element dual-polarization antenna array package for W-band communication and imaging applications," in *Proc. 2018 IEEE 68th Electronic Components and Technology Conference (ECTC)*, 2018, pp. 197–201.

[5] J. W. Jordan, S. Lynch, M. Clark, *et al.*, "Monolithically fabricated 4096-element, polystrata® broadband d-band array demonstrator," in *Proc. 2019 IEEE MTT-S International Microwave Symposium (IMS)*, 2019, pp. 1060–1063.

[6] B. L. Cannon, K. J. Vanhille, and G. A. Sadowy, "Microfabricated dual-polarized, W-band antenna architecture for scalable line arrav feed," in *2015 IEEE International Symposium on Antennas and Propagation & USNC/URSI National Radio Science Meeting*, 2015, pp. 615–616.

[7] A. Gomez-Torrent, M. Garcia-Vigueras, L. Le Coq, *et al.*, "A low-profile and high-gain frequency beam steering subterahertz antenna enabled by silicon micromachining," vol. 68, no. 2, pp. 672–682, 2020.

[8] Y. Zhang, A. R. Vilenskiy, and M. V. Ivashina, "W-band waveguide antenna elements for wideband and wide-scan array antenna applications for beyond 5G," in *Proc. 2021 15th European Conference on Antennas and Propagation (EuCAP)*, 2021, pp. 1–5.

[9] Y. Zhang, A. Vilenskiy, and M. Ivashina, "Wideband open-ended ridge gap waveguide antenna elements for 1-D and 2-D wide-angle scanning phased arrays at 100 GHz," *IEEE Antennas and Wireless Propagation Letters*, vol. 21, no. 5, pp. 883–887, 2022.

[10] A. Agrawal, M. Perry, and N. Landry, "Wideband ridge waveguide radiating element for phased array antennas," in *Proc. IEEE Antennas and Propagation Society International Symposium. 1995 Digest*, vol. 1, 1995, pp. 568–571.

[11] D. T. McGrath, "Calculation of coupling coefficients for arrays with skewed lattices from infinite array scan reflection data," *IEEE Transactions on Antennas and Propagation*, vol. 55, no. 7, pp. 2116–2119, 2007.

[12] A. K. Bhattacharyya, *Phased Array Antennas: Floquet Analysis, Synthesis, BFNs and active array systems.* Hoboken, NJ: John Wiley & Sons, 2006.

[13] P.-S. Kildal, "Three metamaterial-based gap waveguides between parallel metal plates for mm/submm waves," in *2009 3rd European Conference on Antennas and Propagation*, 2009, pp. 28–32.

[14] E. Adas, F. De Flaviis, and N. G. Alexopoulos, "Realization of scan blindness free finite microstrip phased arrays based on mode-free radiating electromagnetic bandgap materials," *IEEE Transactions on Antennas and Propagation*, vol. 66, no. 7, pp. 3375–3382, 2018.

[15] V. I. Litun, H. Rashid, and E. V. Komissarova, "Unit-cell versus finite array approaches for antenna array design," in *2021 Antennas Design and Measurement International Conference (ADMInC)*, 2021, pp. 23–26.

PAPER D

Methods for Attenuating and Terminating Waves in Ridge Gap Waveguide at W-Band: Carbon-Loaded Foam, Carbonyl Iron Paint, and Nickel Plating

A. R. Vilenskiy, **Y. Zhang**, M. V. Ivashina

2021 51st European Microwave Conference (EuMC)
London, United Kingdom, Apr. 2022
©IEEE DOI: 10.23919/EuMC50147.2022.9784367

The layout has been revised.

Abstract

Several methods for electromagnetic waves matched termination and attenuation in a ridge gap waveguide (RGW) are experimentally investigated at W-band. At these frequencies, the implementation of matched loads and attenuators is especially complicated due to small sizes of RGW design features that limits application of traditional waveguide absorbing structures (e.g., absorbing sheets and finlines, ferrite insets, carbonyl iron walls, etc.). The following three techniques are considered: (i) filling an RGW gap with a carbon-loaded foam; (ii) covering a ridge (and pins) with a carbonyl iron paint; (iii) selective nickel plating of an RGW line segment. It was found that the first method exhibits a great broadband absorbing performance and can be easily implemented in a lab environment, whereas the second method can realize a more accurate and predictable attenuating performance. Finally, nickel plating allows for designing resonant RGW terminations and is more interesting from the industrial perspective.

1 Introduction

Gap waveguide (GWG) technology has attracted a lot of interest recently being applied in the areas of antenna and microwave circuits design [1], [2]. The contactless GWG structure greatly alleviates manufacturing accuracy requirements as compared with classical hollow metal waveguide designs. This advantage is especially important at high millimeter(mm)-wave frequencies (W- and D-band) where existing manufacturing technologies almost reached their accuracy limits [3]. Likely, the ridge gap waveguide (RGW) is the most widely used GWG component owing to its relatively compact transverse sizes and wideband single-mode operation [4]. The RGW has been utilized in various mm-wave devices [1], [2] such as array antennas, power distribution networks, filters, couplers, etc. On another note, many traditional waveguide components are yet to be developed in the RGW technology. This, e.g., is related to RGW attenuators and matched terminations (loads) that, to the authors' knowledge, thus far have not been reported. There is a great practical need

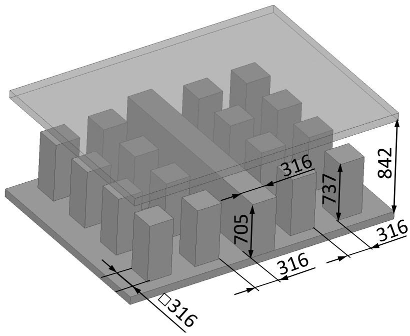

Figure 1: The basic RGW structure with design dimensions (in μm).

in this type of devices for termination of multi-port mm-wave circuits. That includes design of RGW directional couplers and circulators, array antenna laboratorial measurements, and many other applications.

Conventional microwave and mm-wave waveguide loads employ different absorbing insets such as resistive sheets [5], ferrites [6], carbonyl iron blocks [7], etc. In most cases, these elements are precisely located in the waveguide with a proper impedance matching taper. However, at W-band and higher frequencies, a realization of such designs inside a contactless and physically small RGW becomes either very complicated or even impossible. In this contribution, we report on experimental results of RGW waves attenuation and termination at W-band. A regular RGW is considered as a basic structure that has been differently loaded with several absorbing materials: (i) filled with a carbon-loaded foam; (ii) covered by a carbonyl iron paint; (iii) selectively nickel-plated. The presented initial experimental results allow for formulating design guidelines for future industrial and laboratorial mm-wave RGW matched loads and attenuators.

2 Basic RGW and Test Structures

Fig. 1 demonstrates a geometry of the basic RGW used in this study. Two rows of pins are employed at each side of the central ridge, which was found enough to prevent any unwanted mm-wave energy leakage. The RGW dispersion diagram (for a single-period pin structure) is given in Fig. 2 **Kildals:RGW**.

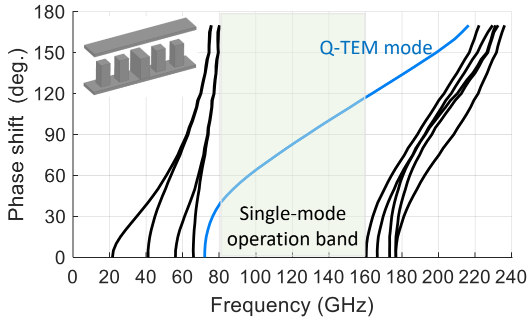

Figure 2: Dispersion diagram of the basic RGW.

It can be found that a single quasi-TEM mode operation regime was realized in the (80 – 160) GHz range. At the same time, the RGW can be practically used approximately above 82 GHz (the weak-dispersion region).

Four test aluminum RGW designs have been fabricated using CNC milling to study different RGW termination methods. These structures are presented in Fig. 3: 10- and 20-pin back-to-back (B2B) and open-ended (OE) RGWs. All structures are interfaced with the measurement equipment through the standard WR10 waveguides that was realized using a wideband orthogonal WR10-to-RGW transition [8]. In Fig. 3, the red lines indicate the measurement reference planes separating the RGW volume being loaded with different absorbing materials in the following section. In order to exclude the influence of the WR10-to-RGW transitions, a dedicated TRL calibration kit was manufactured and used in measurements. First, all test designs were measured without absorbers. The corresponding results are presented in Fig. 4. As seen, for the B2B designs, some S_{11} peaks reach values above –20 dB. This is due to the limited manufacturing accuracy of the TRL calibration standards. The calibration realizes an acceptable measurement performance above 85 GHz (where the LINE standard provides a sufficient phase delay). In Fig. 4, simulated S_{21} (B2B structures) and S_{11} (OE structures) are presented for comparison. These results were computed in Ansys HFSS using Groisse surface roughness model ($R_q = 0.5$ μm). The measured insertion loss of the basic RGW at 95 GHz is estimated as 0.5 dB/cm.

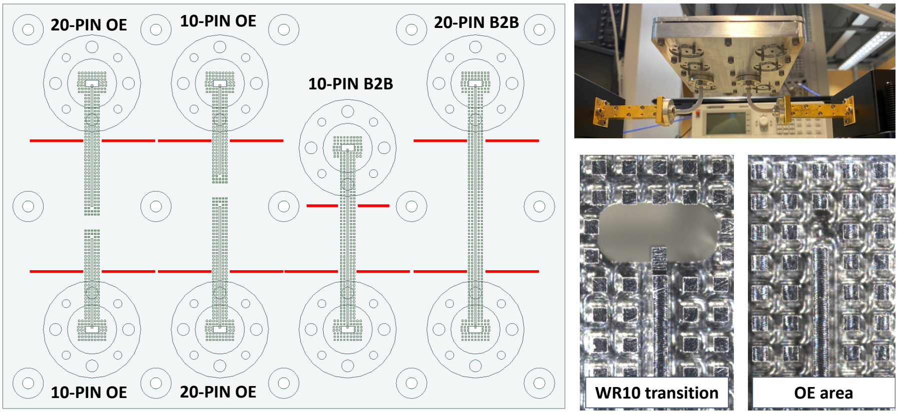

Figure 3: Geometries of the test RGW designs (left), including 10- and 20-pin back-to-back (B2B) and open-ended (OE) structures (red lines depict positions of the measurement reference planes). The manufactured prototype and the measurement setup (top right). Microscope images of the WR10-to-RGW transition and the OE termination (bottom right).

3 RGWs Loaded with Absorbing Materials

3.1 Carbon-Loaded Absorbing Foam

To create the first implementation of the matched RGW termination we used a carbon-loaded absorbing foam WAVASORB® FS from Emerson & Cuming. The foam can be classified as a dielectric loss absorbing material, i.e. the electromagnetic energy loss occurs due to a high dielectric loss tangent [9]. At the time of publication, measurements of absorber electromagnetic properties in W-band are ongoing. We used foam patches of approximately 300-μm thickness that were directly inserted into the air gap of the RGW. To improve the impedance matching, the foam patches were tapered in the H-plane with 60 deg. tapering angle, as shown in Fig. 5(a). Measured results (Fig. 5) evidence a great absorption performance: measured S_{21} for both 10- and 20-pin B2B structures is below –50 dB for the frequencies above 85 GHz. The foam introduces some impedance mismatch, as can be seen by the increased level of S_{11} and S_{22}. The average mismatch level is –15 dB. The

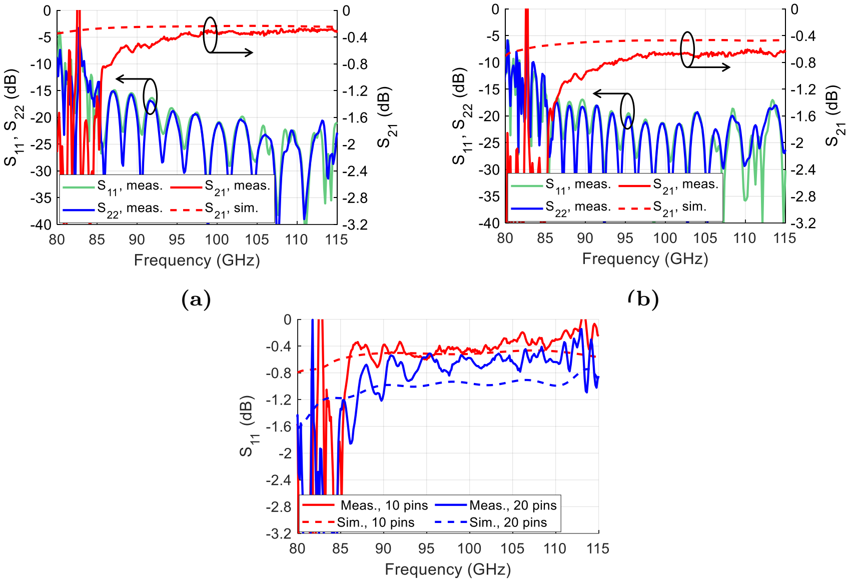

(a) (b)

(c)

Figure 4: Measured and simulated S-parameters of the test RGW designs without absorbers: (a) 10-pin B2B structure; (b) 20-pin B2B structure; (c) OE structures.

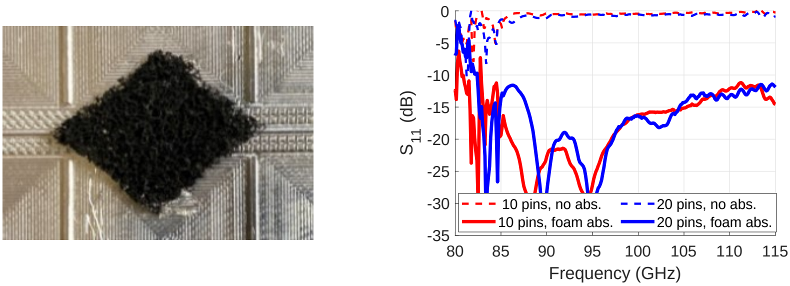

(a) (b)

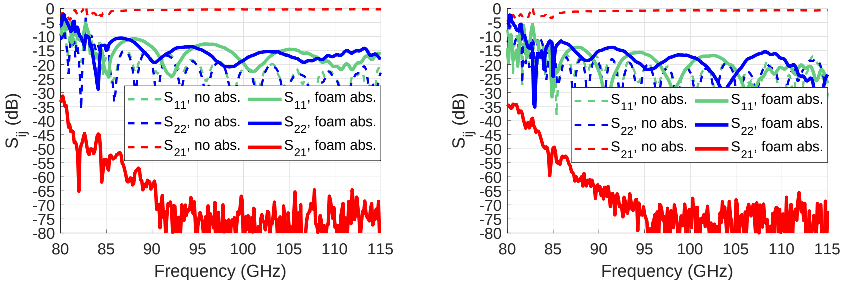

(c) (d)

Figure 5: (a) The H-plane tapered foam absorber inserted into the 10-pin B2B structure. Comparison of measured S-parameters with and without the foam absorber: (b) OE structures; (c) 10-pin B2B structure; (d) 20-pin B2B structure.

authors have found that the mismatch can be further improved by reducing the foam patch thickness to 150-200 μm and using an additional fixture for an accurate foam mounting. On the other hand, employing the foam absorber for a precise attenuation can be tricky due high loss per unit length and difficulty of controlling the foam patch length.

3.2 Carbonyl Iron Paint

Next, the application of the carbonyl iron paint was investigated. We used the off-the-shelf coated carbonyl iron based paint in urethane acrylic resin MF-500 from MWT Materials Inc. The paint has been characterized up to 20 GHz and no data is available for W-band at the time of publication. In general, carbonyl iron paints at microwave and low mm-wave frequencies demonstrate both dielectric and magnetic absorbing properties [10], [11]. However, taking into account typical complex permeability dispersion curves of carbonyl iron, the authors believe that at W-band the dielectric loss should provide the major contribution to the absorption mechanism.

Several methods of the RGW painting have been tested. First, only ridge was painted, as shown in Fig. 6(a). In the second case, both ridge and pins were covered with the paint. The paint thickness is the crucial parameter defining insertion loss per unit length and a quality of impedance matching.

Since, the painting was done manually, it was hard to control the thickness precisely. The estimated paint thickness after curing is in the range of 50-70 μm. We have found that covering the pins provides almost no change in the attenuation performance. It was expected since most of the mm-wave field energy is concentrated between the ridge and the top metal plate. Two test structures (20-pin B2B and OE) were painted and measured. The corresponding results are demonstrated in Fig. 6(b), 6(c). As seen, the paint is capable of realizing a quite strong attenuation – the S_{21} of the B2B structure is below –20 dB. At the same time, it is harder to control impedance matching as compared with the absorbing foam. On the other hand, since the loss per unit length is not as high as for the foam absorber, the paint can also be exploited for a fixed attenuator design. It is believed that using a painting stencil can greatly improve both impedance matching and performance repeatability.

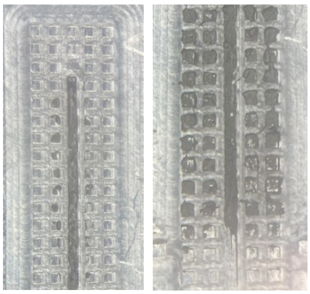

(a)

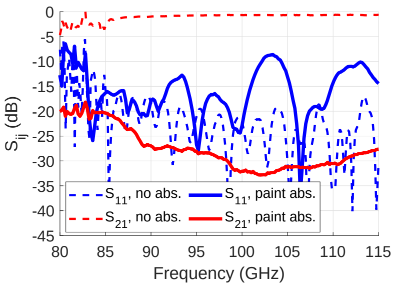

(b)

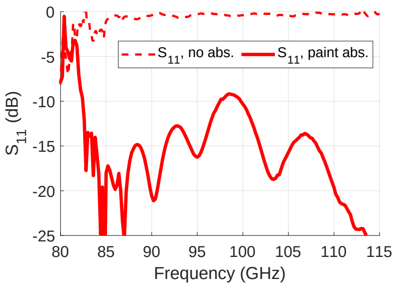

(c)

Figure 6: (a) The RGW with the carbonyl iron paint covering only the ridge or both the ridge and pins. Comparison of measured S-parameters with and without the paint: (b) 20-pin B2B structure; (c) 20-pin OE structure.

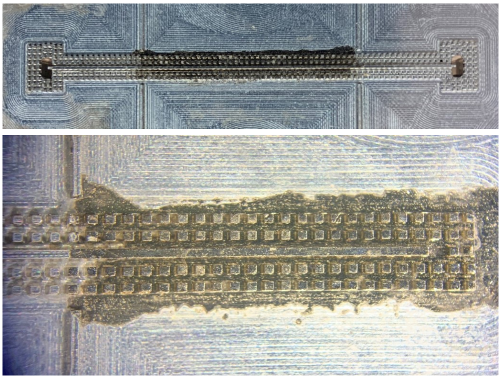

Figure 7: Photographs of the selectively nickel-plated test structures.

3.3 Selective Nickel Plating

Nickel is a conductive ferromagnetic material, whose electromagnetic properties were comprehensively reported at low microwave frequencies [12], [13]. It was shown both theoretically and experimentally that a real part of nickel permeability (μ_r) approaches 1 around 10 GHz. A very limited information is available on nickel characterization at mm-wave and THz frequencies. In [14], the authors studied the effect of surface finish on antenna performance at V-band (60 GHz) reporting the increased dissipation for nickel-based design. This phenomenon was attributed to a moderate electrical conductivity of nickel that is noticeably lower as compared with copper and aluminum.

In this study, we likely for the first time experimentally investigated the effect of nickel plating on the waveguide transmission loss at high mm-wave frequencies. The test structures were selectively nickel-plated using commercial electroplating process (Fig. 7). The top metal plate of the RGWs was also selectively covered with nickel. The estimated nickel thickness is around 5 μm that is sufficiently thicker than the skin depth at W-band. Measured results for all four test structures are presented in Fig. 8. The main observation is the increased insertion (for the B2B structures) and reflection (for the OE structures) loss. The measured insertion loss per unit length is approximately 2.5 dB/cm. An attempt was made to match the simulation model with measurements by tuning the nickel bulk electrical conductivity (σ). It

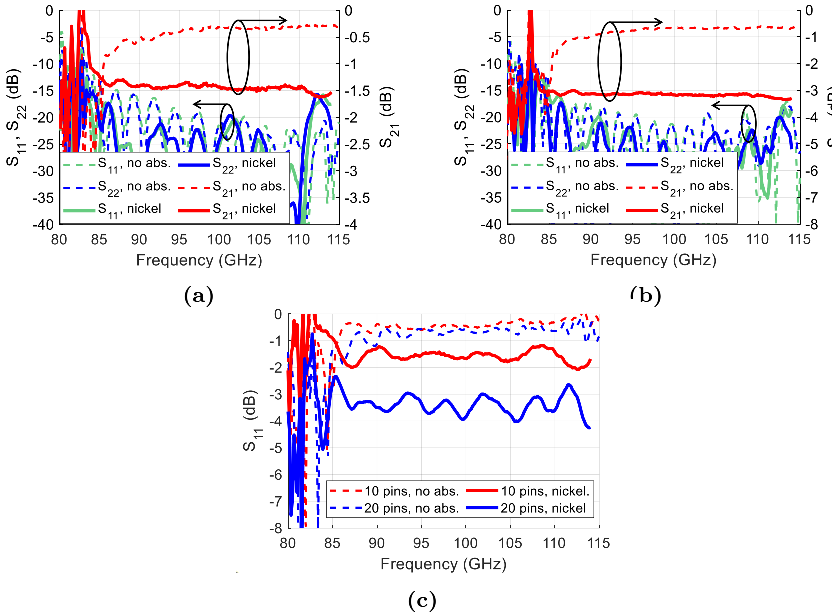

Figure 8: Comparison of measured S-parameters with and without the selective nickel plating: (a) 10-pin B2B structure; (b) 20-pin B2B structure; (c) OE structures.

was found that using $\sigma = 10^7$ S/m (*cf.* [12]), $R_q = 0.5$ μm, and $\mu_r = 1$ gives a noticeably smaller loss (around 1 dB/cm). Therefore, a further study on the nickel performance should be elaborated to reveal an origin of the high insertion loss.

The demonstrated performance of the nickel-plated RGW suggests its possible application for W-band fixed attenuators or narrowband (resonant) matched terminations. The latter implementations can be based on the coupled resonators concept.

4 Conclusions

We have considered several methods of a regular RGW loading at W-band: (i) filling the air gap of the RGW with a carbon-loaded foam; (ii) covering the ridge (and pins) by a carbonyl iron paint; (iii) selective nickel plating of the RGW segment. Absorbing capabilities of the employed materials have been demonstrated experimentally. Summarizing the results, the following main conclusions can be drawn.

- Using the foam absorber is an inexpensive and convenient method for designing wideband well-matched RGW terminations. It is seen as an appropriate solution for creating low- to medium-power loads during laboratorial testing of RGW mm-wave circuits and array antenna measurements (e.g., for the embedded element pattern measurements).

- The carbonyl iron paint can be effectively used to create wideband RGW attenuators and terminations. Controlling the paint thickness is crucial for obtaining the required attenuation and good impedance matching. The method requires using a painting stencil and can be potentially employed for both laboratorial and industrial purposes. The power-handling capabilities of the method are yet to be investigated.

- The nickel-plated RGWs have demonstrated the insertion loss per unit length of 2.5 dB/cm. This value was found to be higher than expected based on the non-magnetic model of nickel. Whether the increased loss is attributed purely to a low electrical conductivity or there are yet some magnetic phenomena at W-band is still the question for future research. However, the revealed absorption performance of nickel suggests its application for creating mm-wave attenuators and resonant matched loads.

The method can be interesting from the industrial perspective due to its high-power handling capabilities, good repeatability and durability.

Acknowledgment

This work has received funding from the European Union's Horizon 2020 research and innovation programme under the Marie Skłodowska-Curie grant agreement No 860023 and the Sweden-Taiwan Collaborative Research Framework Project "Antenna Technologies for Beyond-5G Wireless Communication" from the Swedish Foundation for Strategic Research.

References

[1] E. Rajo-Iglesias, M. Ferrando-Rocher, and A. U. Zaman, "Gap waveguide technology for millimeter-wave antenna systems," vol. 56, no. 7, pp. 14–2, Jul. 2018.

[2] E. Alfonso, M. Baquero, P.-S. Kildal, A. Valero-Nogueira, E. Rajo-Iglesias, and J. I. Herranz, "Design of microwave circuits in ridge-gap waveguide technology," in *Proc. 2010 IEEE MTT-S International Microwave Symposium*, Anaheim, CA, USA, May 2010, pp. 1544–1547.

[3] M. V. Ivashina, A. R. Vilenskiy, H.-T. Chou, J. Oberhammer, and M. Ng Mou Kehn, " Antenna technologies for beyond-5G wireless communication: Challenges and opportunities," in *Proc. 2021 International Symposium on Antennas and Propagation (ISAP)*, Taipei, Taiwan, 2021, pp. 1–2.

[4] P.-S. Kildal, E. Alfonso, A. Valero-Nogueira, and E. Rajo-Iglesias, "Local metamaterial-based waveguides in gaps between parallel metal plates," vol. 8, pp. 84–87, 2009.

[5] T. Stander, P. van der Walt, P. Meyer, and W. Steyn, "A comparison of simple low-power wedge-type X-band waveguide absorbing load implementations," in *Proc. AFRICON 2007*, Windhoek, South Africa, Sep. 2007, pp. 1–3.

[6] Y. Naito and K. Suetake, "Application of ferrite to electromagnetic wave absorber and its characteristics," vol. 19, no. 1, pp. 65–72, Jan. 1971.

[7] Y. Zhang, Q. Wang, and J. Ding, "Short terminal load with broad bandwidth," *Electronics Letters*, vol. 49, no. 16, pp. 1–2, Aug. 2013.

[8] A. U. Zaman and P.-S. Kildal, "Wide-band slot antenna arrays with single-layer corporate-feed network in ridge gap waveguide technology," vol. 62, no. 6, pp. 2992–3001, Jun. 2014.

[9] B. Zhao, M. Hamidinejad, C. Zhao, *et al.*, "A versatile foaming platform to fabricate polymer/carbon composites with high dielectric permittivity and ultra-low dielectric loss," *Journal of Materials Chemistry A*, vol. 7, pp. 133–140, 2019.

[10] L. de C. Folgueras, M. A. AlvesMirabel, and C. Rezende, "Microwave absorbing paints and sheets based on carbonyl iron and polyaniline: Measurement and simulation of their properties," *Journal of Aerospace Technology and Management*, vol. 2, no. 1, pp. 63–70, 2010.

[11] Q. Yuchang, Z. Wancheng, J. Shu, L. Fa, and Z. Dongmei, "Microwave electromagnetic property of SiO_2-coated carbonyl iron particles with higher oxidation resistance," *Physica B: Condensed Matter*, vol. 406, no. 4, pp. 777–780, Feb. 2011.

[12] S. Lucyszyn, "Microwave characterization of nickel," *PIERS Online*, vol. 4, no. 6, pp. 686–690, 2008.

[13] S. N. Starostenko, K. N. Rozanov, A. O. Shiryaev, V. A. Garanov, and A. N. Lagarkov, "Permeability of nickel determined from microwave constitutive parameters of composites filled with nickel powders," vol. 54, no. 11, pp. 1–5, Nov. 2018.

[14] E. Usta and N. T. Tokan, "Effects of surface finish material on millimeter-wave antenna performance," vol. 9, no. 5, pp. 815–821, May 2019.

PAPER E

Millimeter-Wave Quasi-Optical Feeds for Linear Array Antennas in Gap Waveguide Technology

A. R. Vilenskiy, **Y. Zhang**, E. Galesloot, A. B. Smolders, M. V. Ivashina

2022 16th European Conference on Antennas and Propagation (EuCAP)
Madrid, Spain, Apr. 2022
©IEEE DOI: 10.23919/EuCAP53622.2022.9769175

The layout has been revised.

Abstract

A realization of the quasi-optical (QO) feed concept for linear millimeter-wave (sub-)array antennas is demonstrated in gap waveguide technology. The proposed feed architecture employs an input transition from a ridge gap waveguide (RGW) to a groove gap waveguide (GGW), a radial (H-plane sectoral) GGW section, and a transition to an output RGW array. A design decomposition approach is presented to reduce simulation complexity. Several 20-element QO feed implementations are investigated at W-band demonstrating a 20% relative bandwidth (85–105 GHz), 0.5 dB insertion loss, and a capability of an amplitude taper control within the 10–20 dB range.

1 Introduction

The fast development of modern mobile communication networks, radar and sensing systems determines the growing demand in millimeter(mm)-wave antenna solutions [1], [2]. High mm-wave frequency bands, such as W- and D-band, are of particular interest for existing and envisioned radio applications due to a wide available frequency bandwidth, relatively low atmospheric attenuation, high spatial resolution and positioning accuracy that could be achieved for physically small antenna terminals. On the other hand, a high free-space path loss and limited power-generation capabilities can significantly reduce system operation range at these frequencies. In view of these factors, high-gain phased array antennas (PAAs) with a versatile dynamic beam control have been largely exploited for such systems at high mm-wave frequencies [3]. A design complexity is another severe challenge that makes many traditional PAA architectures unavailable due to high production cost and/or tight manufacturing tolerances. Today, probably the most popular W/D-band PAA solutions employ the antenna-on-chip (AoC) and antenna-in-package (AiP) technologies [4]. However, despite high integration potential and affordability, AoC and AiP implementations are typically narrowband, limited in beam-steering range and radiation efficiency.

Recently, we have proposed a linear (sub-)array concept combining a low-order (1-bit) phase resolution and a spatial quasi-optical (QO) beamforming network [5]. This PAA concept is illustrated in Fig. 1(a) where an array of N_x radiating elements with integrated 1-bit phase shifters is excited through a QO tapered feed. As shown in [5] based on the approach developed in [6], the QO feed can be effectively used as a low-loss alternative to conventional corporate PAA feeds, with its non-linear output phase distribution being deliberately utilized for phase quantization errors randomization.

In this contribution, we concentrate on a gap waveguide (GWG) QO feed implementation at W-band (85 – 105 GHz), as demonstrated in Fig. 1(b). The GWG technology [7], utilizing a 2-D electromagnetic bandgap (EBG) surface (bed of nails in this study) between two parallel metal plates to stop electromagnetic waves propagation, can offer low-loss contactless waveguiding and radiating structures. In [8], we demonstrated a GWG array element design that can be co-integrated with phase-shifting electronics and thus be employed in beam-steering PAAs as opposed to most reported GWG antennas that are fixed-beam. In this way, the GWG QO feed can be used to realize a complete beam-steering W-band PAA system with a fully contactless design greatly alleviating manufacturing and assembling tolerances. Previously, several GWG H-plane horn antennas, employing tapering ridge gap waveguide (RGW), have been reported [9], [10]. In the case of a linear PAA, a wideband impedance matching between a tapering RGW and an array of the output channels is complicated. In that regard, in this study, we propose a QO feed based on a radial (sectoral) groove gap waveguide (GGW) connecting an array of output RGW channels with an RGW input. In particular, the following technical problems will be addressed: (i) impedance matching of the RGW input and output channels; (ii) compensation of an edge elements mismatch; (iii) minimization of transmission coefficients frequency ripples; (iv) controlling the QO feed output amplitude and phase distributions.

2 GWG Quasi-Optical Feed Design

The proposed design is based on the bed of nails EBG surface that forms sidewalls of both the RGW and radial GGW. Main design dimensions are presented in the inset of Fig. 1(b). A single-mode operation bandwidth of the basic RGW spans 80–160 GHz. A dispersion diagram and losses analysis for this RGW can be found in [11]. Thus, the QO feed comprises three main parts: (i) the input basic RGW with a transition to the GGW input; (ii)

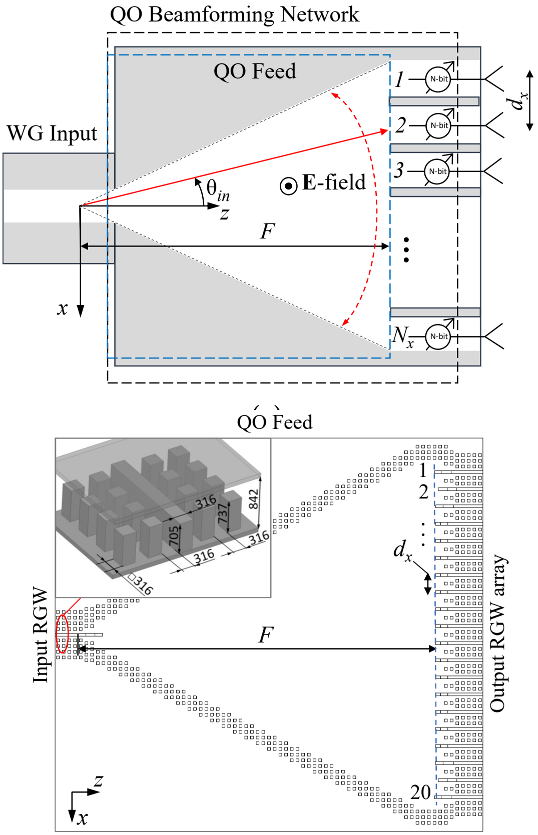

(b)

Figure 1: (a) A linear (sub-)array antenna with a QO beamforming network comprising a QO feed and N-bit integrated phase shifters [5]. (b) An implementation of the QO feed in GWG technology. The inset demonstrates a basic RGW structure (units: μm).

the linearly tapering or radial GGW; (iii) the array of the output RGWs with transitions to the radial GGW output. An inter-element spacing of the output array $d_x = 1.896\,\text{mm} = 0.6\lambda_0$, where λ_0 is the free-space wavelength at the central design frequency $f_0 = 95$ GHz. The targeted design bandwidth is 85 – 105 GHz.

As discussed in [5], [6], for PAAs with a low-order phase resolution (e.g., 1-bit) a crucial design parameter is the QO feed focal ratio $F/(N_x d_x)$, where F is the focal distance (Fig. 1(a)). In the case of the 1-bit phase control, the optimum focal ratio is around 0.8 – 1.0 for a 10 – 20 dB amplitude taper. In this study, the focal ratio has been chosen as 1.0 (a GGW sidewalls tapering angle is 26.5°) that allows having a regular widening of the GGW, where for each two EBG periods ($P_{EBG} = 0.632$ mm) along z-axis the sidewall shifts for one period along x-axis. It helps to generate a more homogeneous field in the GGW area, which results in stabilized transmission coefficients over frequency.

Since a direct optimization of the QO feed with $N_x = 20$ represents an electrically large simulation problem, we have developed a decomposition approach allowing a separate design of the input and output GGW-to-RGW transition structures. That will be detailed in the following subsections. For all simulation models, aluminum has been used with 0.5-μm surface roughness (Groisse model).

2.1 Output RGW-to-GGW Transition: Central Elements

The receiving performance of the central output RGW channels can be simulated using the reciprocity principle by representing the channel as an element of an infinite transmitting 1-D array. Fig. 2 illustrates such simulation model with assigned sidewall ($\pm x$-direction) periodic boundary conditions (PBC), absorbing boundary conditions (ABC) in front ($-z$-direction) of the element, and aluminum walls at $\pm y$-direction. Thus, optimizing element's active reflection coefficient Γ_{out} for a given scan angle θ_s results in the matched receiving of an incident wave from the $\theta_{in} = \theta_s$ direction (inside the QO feed), as depicted in Fig. 1(a). To provide a required impedance matching, we have introduced a wideband matching circuit comprising a 2-step RGW impedance transformer and an EBG sidewalls transition from the 2- to a 1-pin configuration. Fig. 3 shows the final Γ_{out} for different θ_s after a full-wave model optimization in Ansys HFSS. As seen, the element is well-matched for $\theta_s \leq 30°$. When θ_s

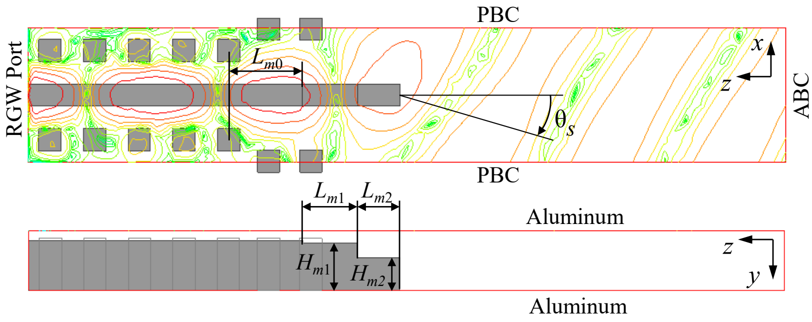

Figure 2: The output RGW element in the infinite 1-D array environment. The overlapping E-field distribution (top plot) is given at 95 GHz and $\theta_s = 30°$.

approaches 40°, the impedance matching significantly degrades, which resembles the scan blindness phenomenon in conventional 2-D arrays [12]. In such the 1-D array this effect can be expected when an equivalent grating-lobe-free condition $\sin(\theta_s) < \lambda/d_x - 1$ (λ is a free-space wavelength) is violated. The latter limits a minimum $F/(N_x d_x)$ for a given d_x/λ_0.

2.2 Output RGW-to-GGW Transition: Edge Elements

For the output RGW elements positioned close to the edge, the PBC imposed in Section 2.1 are not relevant due to the proximity of the GGW sidewalls. A 5-element full-wave model has been created to reconstruct the edge elements operation conditions. Fig. 4 depicts the model for three various configurations (O1 – O3) of the QO feed edge area. The first three edge elements have unique parameters of the matching circuit, whereas elements 4 and 5 are fully identical to the central element. In the xz-plane, the model is surrounded by the ABC.

The designs of the edge elements have been optimized by minimizing their $|\Gamma_{out}|$ for the case of scanning along the $\theta_s = 26.5°$ direction (parallel to the sidewall):

$$\Gamma_{out\,m} = \sum_{n=1}^{5} S^e_{mn} \exp\left(-j(n-m)k_x d_x\right), \; m = 1...3, \tag{E.1}$$

where $[S^e]$ is the S-matrix of the 5-port network; $k_x = 2\pi/\lambda \sin(\theta_s)$. Optimized Γ_{out} for the output configuration #1 is shown in Fig. 5. In general,

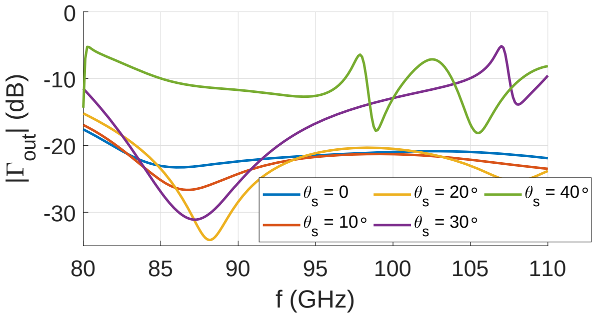

Figure 3: Frequency dependencies of the output periodic element's active reflection coefficient for different scan angles θ_s. Design parameters (in μm): $L_{m0} = 1051$, $L_{m1} = 777$, $L_{m2} = 602$, $H_{m1} = 665$, $H_{m2} = 457$.

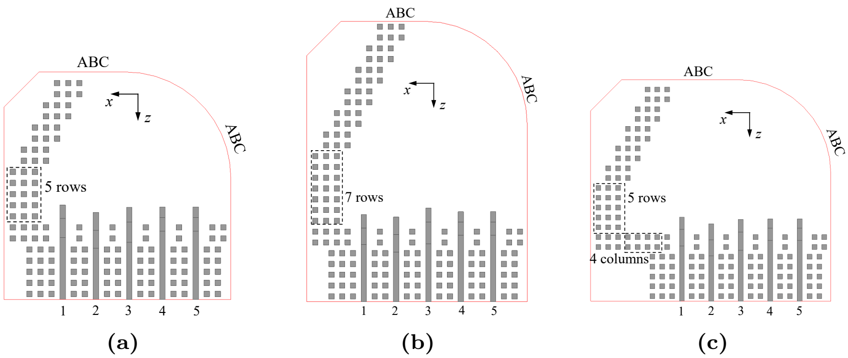

Figure 4: Different configurations of the QO feed edge area: (a) configuration #1 (O1) – 5 additional rows of pins; (b) configuration #2 (O2) – 7 additional rows of pins; (c) configuration #3 (O3) – 5 additional rows and 4 columns of pins.

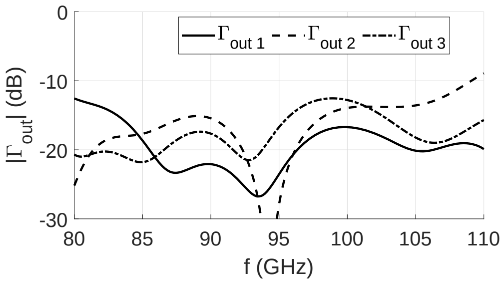

Figure 5: Active reflection coefficients for the edge elements of the configuration O1 (Fig. 4(a)), $\theta_s = 26.5°$. Design parameters (in μm): $L_{m0}^{(1,2,3)} = 693, 68, 417$, $L_{m1}^{(1,2,3)} = 1077, 1026, 1159$, $L_{m2}^{(1,2,3)} = 765, 1028, 826$, $H_{m1}^{(1,2,3)} = 658, 632, 647$, $H_{m2}^{(1,2,3)} = 434, 477, 462$.

a well-matched performance can be achieved for the elements of all configurations. However, each configuration, as will be shown in Section 3, has a different effect on the overall QO feed characteristics.

2.3 Input RGW-to-GGW Transition

A separate model for the input transition has been developed to optimize input impedance matching and investigate the primary (illumination) field of the QO feed. Fig. 6 details three different input configurations (I1 – I3). The model is surrounded by the ABC in the xz-plane. The three designs exploit the same structure of the wideband impedance-matching circuit (Fig. 2). The crucial difference between the configurations is the organization of the RGW-to-GGW transition, which is created by an opening of the input RGW sidewalls. For I1, the transition is formed by $1.5P_{EBG}$ shift of the one row of pins, whereas the following three rows are shifted by P_{EBG} (one-and-three scheme). The two-and-two scheme ($1.5P_{EBG}$ first row shift) is used for the I2 that allows having a wider first GGW section. Finally, the widest input GGW ($2.5P_{EBG}$ first row shift) is utilized in I3 together with the two-and-two scheme.

A good impedance matching performance has been achieved for all configurations as shown in Fig. 7. From the electromagnetic perspective, the input RGW-to-GGW transition can be seen as: (i) a transition from the input RGW to a stepped rectangular GGW; (ii) a transition from the stepped GGW to

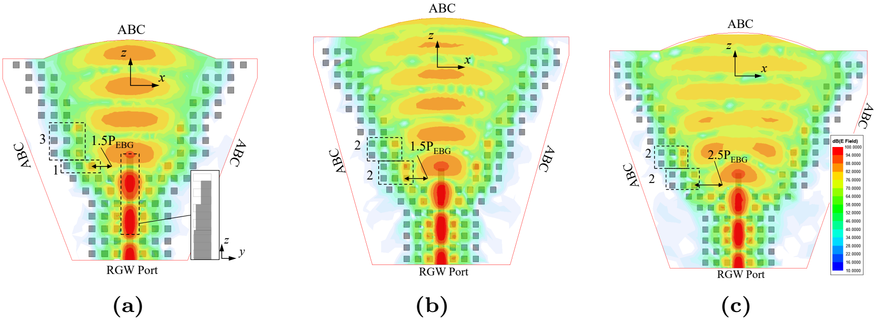

Figure 6: Different configurations of the QO feed input: (a) configuration #1 (I1) – the input aperture is formed by the consequent shift of one and three rows of pins with $1.5P_{EBG}$ shift of the first row (the inset demonstrates a ridge structure in the transition region); (b) configuration #2 (I2) – the input aperture is formed by the consequent shift of two and two rows of pins with $1.5P_{EBG}$ shift of the first row; (c) configuration #3 (I3) – the same as configuration #2 but with $2.5P_{EBG}$ shift of the first row. The instantaneous E-field distributions are given at 95 GHz.

the radial (H-plane sectoral) GGW when the local transverse size of the GWG is much larger than $2P_{EBG}$. Thereby, a transverse structure of the primary field will be defined by an excited modal content of the radial GGW, which, in turn, depends on a modal content excited in the stepped GGW. The latter will be demonstrated below.

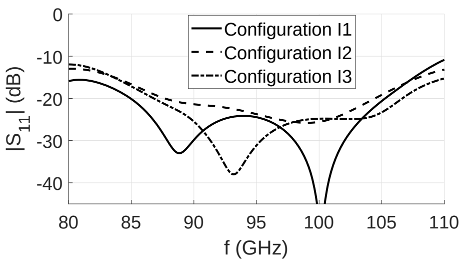

Figure 7: Input reflection coefficient for the three configurations from Fig. 6. Design parameters (in μm): $L_{m0}^{in(1,2,3)} = 324, 573, 653$, $L_{m1}^{in(1,2,3)} = 1063, 987, 1036$, $L_{m2}^{in(1,2,3)} = 966, 855, 903$, $H_{m1}^{in(1,2,3)} = 621, 629, 619$, $H_{m2}^{in(1,2,3)} = 410, 371, 382$.

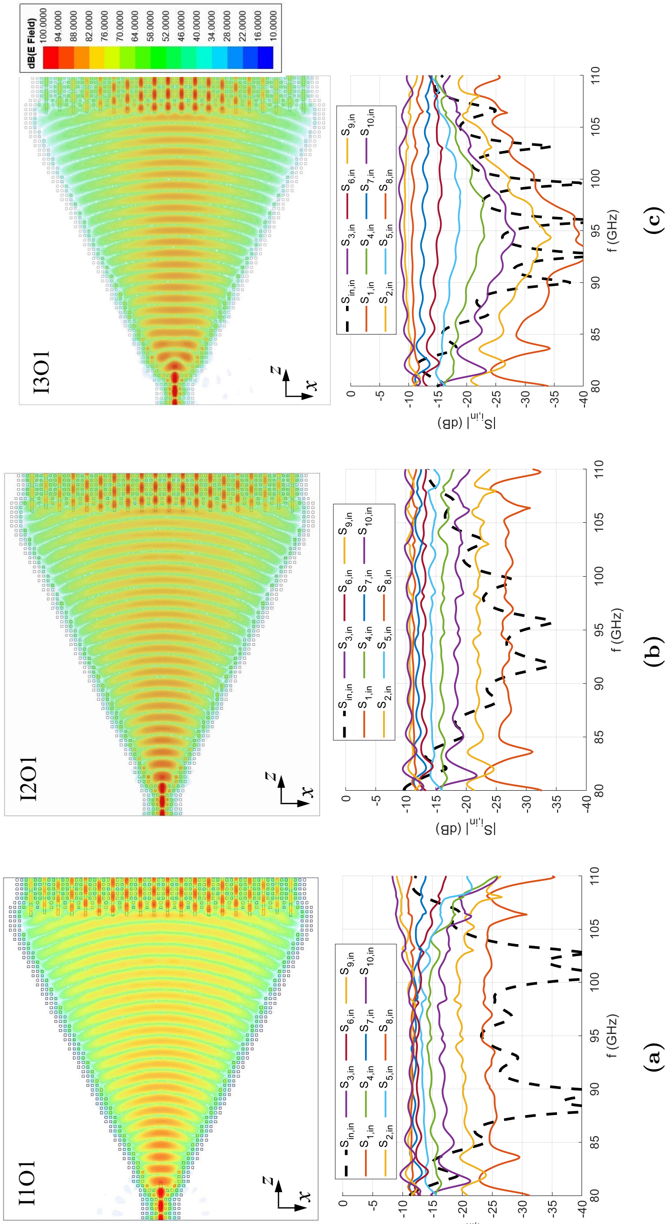

Figure 8: Different configurations of the full QO feed and corresponding S-parameter magnitudes: (a) configuration I1O1; (b) configuration I2O1; (c) configuration I3O1. The instantaneous E-field distributions are given at 95 GHz (input port excited).

3 Full QO Feed Performance

3.1 Frequency Performance

We have designed several QO feeds using different combinations of the input and output transition configurations. Three exemplary designs are demonstrated in Fig. 8 together with simulated magnitudes of S-parameters. In all cases, output configuration O1 has been used. As seen, the input configuration I1 realizes the minimum output amplitude taper. The modal content of the radial GGW predominantly consists of TE_{01} and TE_{03} modes (with respect to the radial direction) that effectively increases illumination of the edge elements. At the same time, the I2 configuration excites mainly TE_{01}, which results in a higher amplitude taper. When the wide I3 configuration is used, the input stepped rectangular GGW becomes over-moded, with both TE_{10} and TE_{30} (with respect to z-axis) excited. In the radial waveguide, this initial GGW field generates a complex multi-modal field content with high directivity determining a very high amplitude taper. Summarizing, it was found that the configurations I1O1 and I2O1 realize a good transmission flatness over frequency with the maximum ripple below ± 1 dB (85 – 105 GHz range).

To demonstrate the effect of the edge elements matching, we have simulated the I2O1 QO feed where all output RGW elements have the same (periodic model) matching circuit. Results, presented in Fig. 9(a), clearly demonstrate the increase in frequency ripples for the edge elements transmission coefficients. It was also found that the the output configuration O3 noticeably deteriorates the transmission performance flatness (Fig. 9(b)) due to significant field reflections from the extended corner regions. In all considered cases, a simulated dissipative loss is below 0.5 dB.

3.2 Amplitude and Phase Distributions Analysis

Fig. 10 presents the output amplitude and phase distributions for different QO feed configurations. In this plot, we also demonstrate analytical curves approximating elements amplitude (A_i) and phase (φ_i) according to the cosine-on-pedestal and cylindrical phase front models [5]:

$$A_i = C + (1 - C)\cos\big(\pi x_i/(N_x d_x)\big). \tag{E.2}$$

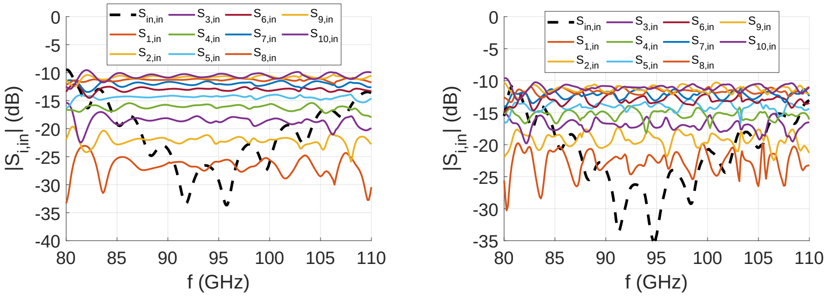

(a) **(b)**

Figure 9: Frequency performance of (a) configuration I2O1 without optimized edge elements, (b) configuration I2O3.

$$\varphi_i = -2\pi/\lambda\left(\sqrt{x_i^2 + F^2} - F\right),\ i = 1...N_x. \tag{E.3}$$

where C is the parameter defining the amplitude taper. As seen, the configuration with I2 input realizes almost ideal cylindrical phase distribution with 16 dB amplitude taper. When I1 input is employed, the taper can be reduced. However, the amplitude distribution becomes more frequency-dependent. This is due to a complex modal content of the radial GGW. For the elongated output configuration O2, the taper can be further reduced to 10–12 dB.

4 Conclusion

In this contribution, we have considered the quasi-optical (QO) feeds for mm-wave linear (sub-)array antennas in gap waveguide (GWG) technology. The holistic design approach has been introduced that relies on the design decomposition principle where both input and output transition parts can be developed using the dedicated electromagnetic models with reduced simulation complexity. The approach has been utilized to develop and investigate several W-band GWG QO feeds with different input and output configurations. The obtained simulation results evidence wideband (85–105 GHz) and low insertion-loss (< 0.5 dB) feed performance with stable transmission characteristics (± 1 dB maximum frequency ripple). Future research directions will

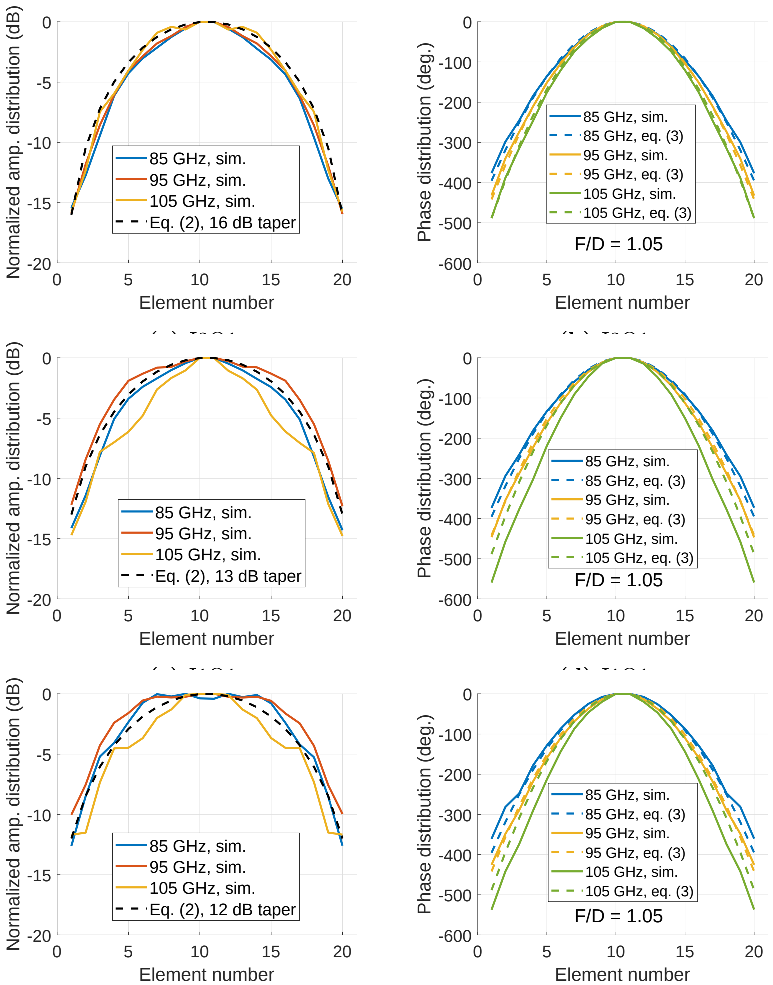

(e) I1O2 **(f)** I1O2

Figure 10: Amplitude (left) and phase (right) distributions for different QO feed configurations.

address additional methods for amplitude and phase distributions control.

Acknowledgment

This work has received funding from the European Union's Horizon 2020 research and innovation programme under the Marie Skłodowska-Curie grant agreement No 860023 and the Sweden-Taiwan Collaborative Research Framework Project "Antenna Technologies for Beyond-5G Wireless Communication" from the Swedish Foundation for Strategic Research.

References

[1] *European vision for the 6G network ecosystem*, White Paper, The 5G Infrastructure Association, Jun. 2021.

[2] M. Ivashina, A. Vilenskiy, H.-T. Chou, J. Oberhammer, and M. N. M. Kehn, "Antenna technologies for beyond-5g wireless communication: Challenges and opportunities," in *Proc. 2021 International Symposium on Antennas and Propagation (ISAP))*, Taipei, Taiwan, Oct. 2021, pp. 1–2.

[3] T. S. Rappaport, Y. Xing, O. Kanhere, *et al.*, "Wireless communications and applications above 100 GHz: Opportunities and challenges for 6G and beyond," *IEEE Access*, no. 7, pp. 78 729–78 757, 2019.

[4] S. Shahramian, M. J. Holyoak, A. Singh, and Y. Baeyens, "A fully integrated 384-element, 16-tile, W-band phased array with self-alignment and self-test," *IEEE Journal of Solid-state Circuits*, vol. 54, no. 9, pp. 2419–2434, 2019.

[5] A. R. Vilenskiy, E. Galesloot, Y. Zhang, A. Bart Smolders, and M. V. Ivashina, "Quasi-optical beamforming network for millimeter-wave electronically scanned array antennas with 1-bit phase resolution," in *Proc. 2021 15th European Conference on Antennas and Propagation (EuCAP)*, 2021, pp. 1–5.

[6] A. R. Vilenskiy, M. N. Makurin, and C. Lee, "Phase distribution optimization for 1-bit transmitarrays with near-field coupling feeding technique," in *Proc. 14th European Conference on Antennas and Propagation, (EuCAP 2020)*, Copenhagen, Denmark, Mar. 2020, pp. 1–5.

[7] A. U. Zaman and P.-S. Kidal, “Gap waveguide in handbook of antenna technologies,” in New York, NY: Springer Science+ Business Media Singapore, 2015, p. 464.

[8] Y. Zhang, A. R. Vilenskiy, and M. V. Ivashina, “W-band waveguide antenna elements for wideband and wide-scan array antenna applications for beyond 5G,” in *Proc. 2021 15th European Conference on Antennas and Propagation (EuCAP)*, 2021, pp. 1–5.

[9] E. Sabbaghi, S. A. Razavi, and M. H. Ostovarzadeh, “Wide band ridge gap waveguide (RGW) fan beam antenna with low side lobes based on parabolic reflector principle,” *IET Microwaves, Antennas & Propagation*, vol. 14, pp. 343–347, 5 2020.

[10] W. Yuan, J. F. Chen, C. Zhang, *et al.*, “Glide-symmetric lens antenna in gap waveguide technology,” *IEEE Transactions on Antennas and Propagation*, vol. 68, no. 4, pp. 2612–2620, Apr. 2020.

[11] A. R. Vilenskiy, Y. Zhang, and M. V. Ivashina, “Methods for attenuating and terminating waves in ridge gap waveguide at W-band: Carbon-loaded foam, carbonyl iron paint, and nickel plating,” in *Proc. 51 European Microwave Conference (EuMC)*, accepted, 2021, pp. 1–5.

[12] A. K. Bhattacharyya, *Phased array antennas: Floquet analysis, synthesis, BFNs and active array systems.* John Wiley & Sons, 2006, vol. 179.

PAPER F

Quasi-Optical Beamforming Network for Millimeter-Wave Electronically Scanned Array Antennas with 1-Bit Phase Resolution

A. R. Vilenskiy, E. Galesloot, **Y. Zhang**, A. B. Smolders, M. V. Ivashina

2021 15th European Conference on Antennas and Propagation (EuCAP)
Dusseldorf, Germany, Mar. 2021
 DOI: 10.23919/EuCAP51087.2021.9410922

The layout has been revised.

Abstract

State-of-the-art design solutions for electronically scanned array antennas are mostly limited to microwave to low mm-wave frequency bands, while the demand for new designs at higher frequencies (i.e. frequencies beyond 100 GHz) is rapidly growing. We attempt to fill in this knowledge gap by presenting a new linear array antenna architecture as a building block of 2D arrays that can enable efficient beam steering and a simplified array design. This concept is based on the combination of a low-loss quasi-optical (QO) feed, providing predefined antenna port excitation, with 1-bit phase shifters which are co-integrated with the array antenna elements. In this study, we formulate the array design problem as minimization of the sidelobe level (SLL) through an optimum quasi-randomization of phase errors. An analytical expression for the optimum focal ratio of the QO feed has been derived to establish the relationships between the key design parameters. These results are validated through numerical simulations revealing that the optimum focal ratio leads to the minimum SLL.

1 Introduction

An increasing demand in millimeter-wave (mm-wave) radio systems for wireless communication and sensing drives the development of high-performance mm-wave phased array antennas (PAAs) with beam-steering capabilities. In particular, E-, W-, and D-bands have already been widely allocated for communication and radar applications and are being considered for future (e.g. beyond 5G) networks deployment [1]. However, high dissipation losses, components cost, and tight manufacturing tolerances at these frequencies severely restrict suitability of the existing design solutions and manufacturing technologies. These complexities steer the research towards non-conventional PAA architectures, where specific design trade-offs can provide relatively high electrical performance with a simple PAA structure.

Recently, the concept of low-order (1- and 2-bit) phase control was applied to beam-steerable PAAs to realize compact and energy-efficient designs at

$<$ 30 GHz bands [2]–[5]. This approach is especially promising for higher frequencies. In fact, at high mm-wave frequencies, the state-of-the-art monolithic digital phase shifters (PSs) typically provide 2.5–3 dB insertion loss per bit [6]. At the same, the PAA gain loss due to 1-bit phase quantization errors is around 3.8 dB and almost 1 dB for 2-bit quantization [7]. Thus, at W-band, 1-bit and 2-bit based architectures demonstrate similar antenna gain and efficiency, while the 1-bit PAAs have an advantage of a simpler and more compact design. The key challenge of such designs is phase quantization sidelobes appearing due to periodic PAA aperture phase errors [8], which are especially severe for the 1-bit PAAs. As studied in [7], parasitic mirror lobes occur during beam-steering when a 1-bit PAA is exited with a linear phase and a simple rounding-off method is used to set the PS phase. This effect can be reduced via phase quantization error randomization, as demonstrated in [9].

In this work, we investigate the 1-bit PAA concept for the applications at $\sim$100 GHz bands. A new linear array antenna architecture is proposed as a building block of 2D arrays which can enable efficient beam steering, while overcoming the major physical constraints and power loss at these frequencies.

2 Proposed 1-bit PAA architecture

The proposed linear PAA architecture is illustrated in Fig.1. It includes an array of N_x radiating antenna elements with inter-element spacing d_x. The elements are excited through a planar quasi-optical (QO) beamforming network. This network comprises a QO feed – representing a low-loss alternative to conventional corporate feed networks for mm-wave large-scale arrays ($N_x > 10$) – and N_x 1-bit PSs which can be co-integrated with the individual array elements. The PS's states differ from element to element between 0 and 180° values depending on a beam-steering direction. The QO feed is a crucial component for efficient feeding that also realizes a beam-steering functionality in conjunction with the 1-bit PSs. The design principle of such a hybrid (QO feed + PSs) beamforming network can be described in the following way. Due to the 1-bit phase quantization, it is necessary to have a certain nonlinear initial phase distribution at the array ports (see the reference plane at the input ports of the PSs in Fig. 1). This nonlinear distribution is essential to eliminate the 1-bit parasitic mirror lobes [4], [7]. It can be considered as a

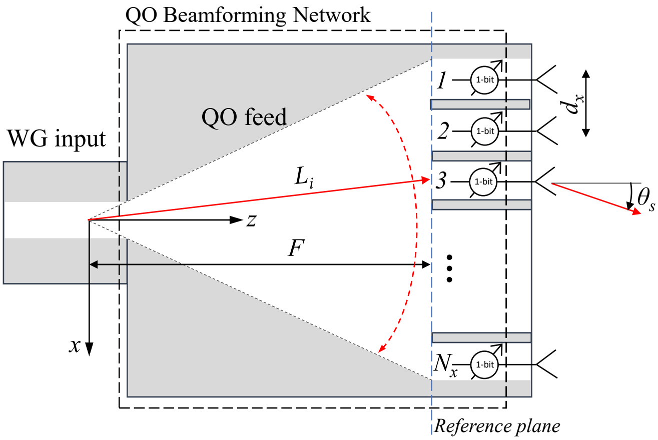

Figure 1: A 1D sub-array building block of the proposed 1-bit beam-steering phased array architecture at W-band.

phase error quasi-randomization method realizing the performance close to the phase-added method [9]. In hardware, this initial excitation can be implemented by feeding the sub-array through a tapered waveguide section with the focal ratio $F/(N_x d_x)$ (*cf.* [10]), where F is the focal length (see Fig. 1).

The main advantage of this architecture is its highly-integrated and simple design, which can be manufactured in a standard waveguide technology and, as opposed to corporate feed PAAs, conveniently realizes the nonlinear initial phase distribution for high N_x. In fact, using the space (optical) PAA feeding to deliberately destroy the periodicity of phase quantization errors was proposed a long time ago in [11] and is used in 1- and 2-bit transmitarrays with a focal source [3], [5]. Nevertheless, there are still open questions that we address in this study: *(i) What is the optimum initial phase distribution in terms of the lowest 1-bit PAA sidelobe level (SLL)? (ii) What is the optimum QO feed design realizing the latter?*

In [7], these questions were addressed for 1-bit PAAs with a uniform amplitude distribution. In this paper, we extend this approach to non-uniform amplitude distributions and provide an in-depth analysis of the SLL performance showing that the maximum SLL can be effectively reduced by using the optimum QO feed focal ratio.

3 1-Bit Array Far Field

3.1 Radiation Model

We consider a linear array of N_x elements (Fig. 1). Neglecting the edge effects, the array far field can be represented as

$$\mathbf{E}_{FF}(\theta) = \mathbf{F}_e(\theta) \sum_{i=1}^{N_x} A_i \mathrm{exp}(j[\Phi_i + \varphi_i^{\Sigma}]), \tag{F.1}$$

where $\mathbf{F}_e$ is the embedded element pattern (azimuthal dependence is omitted); $\Phi_i = k_0 x_i \mathrm{sin}(\theta)$, $x_i = [i-(N_x+1)/2]d_x$, $k_0 = 2\pi/\lambda_0$ is the wavenumber, λ_0 is the free-space wavelength; A_i and φ_i^{Σ} are the i-th element excitation amplitude and phase. The latter can be expressed through the output phase φ_i^{QO} at the reference plane and the 1-bit PS phase φ_i^{PS}:

$$\varphi_i^{\Sigma} = \varphi_i^{QO} + \varphi_i^{PS}. \tag{F.2}$$

On the other hand, $\varphi_i^{\Sigma} = \Phi_i^0 + \delta\varphi_i$, where $\Phi_i^0 = -k_0 x_i \mathrm{sin}(\theta_s)$ is an ideal element phase, θ_s is a beam-steering angle, $\delta\varphi_i$ is a phase quantization error. The excitation through the QO feed is approximated by a cylindrical phase front emanating from the focal center at the distance F from the reference plane (Fig. 1):

$$\varphi_i^{QO} = -k_0\big(\sqrt{x_i^2 + F^2} - F\big). \tag{F.3}$$

In (F.3), we assume the QO feed propagation constant equals k_0. At the same time, the amplitude distribution is modeled as the cosine-on-a-pedestal function [8] (with the taper parameter C), which was found to be a reasonable approximation for the QO feed with y-oriented E-field (Fig. 1):

$$A_i = C + (1-C)\mathrm{cos}\big(\pi x_i/(N_x d_x)\big). \tag{F.4}$$

Since we are dealing with the 1-bit phase quantization, φ_i^{PS} switches between 0 and 180° values during beam steering [7], and thus we need to find an optimum value of F that will provide "the best" $\delta\varphi_i$ randomization over the PAA aperture.

3.2 Optimum Quasi-Optical Feed Design

Let us consider the AF, which is given by the summation factor in (F.1). Following the procedure used in [7], [12], we can represent the PAA AF in the spectral domain as a superposition of radiation from the continuous apertures with phase distributions $\Phi_{mh}(x)$. Indices m and h denote the grating lobe and phase quantization orders, respectively. Thus, each spectral term F_{mh}, $h \neq 0$, gives the contribution to the AF due to the phase quantization errors. We will herein refer to these terms as phase quantization lobes (PQLs). For electrically large PAAs with $N_x d_x >> \lambda_0$, the stationary phase method can be used to estimate PQL values [7]:

$$F_{mh}(\theta) = \frac{(-1)^{m(N_x-1)}\sqrt{2\pi}}{\sqrt{-jd^2\Phi_{mh}(x_0)/dx^2}} \frac{A(x_0)}{1+Mh} \mathrm{e}^{j\Phi_{mh}(x_0)}, \tag{F.5}$$

$$\begin{aligned}\Phi_{mh}(x) =& \Phi(x) + \Phi^0(x) + \\ & Mh(\Phi^0(x) - \varphi^{QO}(x)) - \frac{2\pi m x}{d_x},\end{aligned} \tag{F.6}$$

$$Mh\frac{d\varphi^{QO}(x_0)}{dx} = k_0\sin(\theta) - k_0\sin(\theta_s)(1+Mh) - \frac{2\pi m}{d_x}, \tag{F.7}$$

where $M = 2^p$, and $p = 1$ is the number of PS bits. In (F.5)–(F.7), all continuous functions $\big(A(x),\ \varphi(x)\big)$ are equal to the discrete equivalents at array grid points x_i. We can now require PQL power values to remain constant and equal to K_h^2 for any m. This leads to the differential equation

$$\frac{d^2\varphi^{QO}(x)}{dx^2} = -\frac{2\pi A^2(x)}{K_h^2 M|h|(1+Mh)^2}. \tag{F.8}$$

It is now up to us to choose any value of K_h^2. However, from (F.7) and (F.8) we can find that decreasing K_h^2 leads to the F_{mh} PQL widening. In [12], it was suggested that the PAA SLL can be minimized if PQLs do not overlap. We will employ the same approach here. From (F.5), we can see that the PQL width is determined by $A(x_0)$, which is non-zero only for $x_0 \in [-N_x d_x/2; N_x d_x/2]$. According to (F.7), PQLs are equidistantly distributed in the u-space, where $u = k_0\sin(\theta) - k_0\sin(\theta_s)(1+Mh)$, with the period $2\pi/d_x$. Thus, requiring that the PQL width be equal $2\pi/d_x$ we arrive at

$$M|h|\left(\frac{d\varphi^{QO}(N_x d_x/2)}{dx} - \frac{d\varphi^{QO}(-N_x d_x/2)}{dx}\right) = \frac{2\pi}{d_x}. \tag{F.9}$$

Integrating (F.8) one time and employing (F.9), we find the optimum $K^2_{h\,opt}$:

$$K^2_{h\,opt} = \frac{N_x d_x^2}{(1+Mh)^2}\left[C^2 + \frac{4C(1-C)}{\pi} + \frac{(1-C)^2}{2}\right]. \tag{F.10}$$

Next, integrating twice both sides of (F.8) and setting integration constants to 0 we can find the sought-for optimum initial phase distribution φ^{QO}_{opt}:

$$\begin{aligned}\varphi^{QO}_{opt}(x) = &-\frac{2\pi}{K^2_{h\,opt} M|h|(1+Mh)^2}\times \\ &\left[\left(C^2 + \frac{(1-C)^2}{2}\right)\frac{x^2}{2} - \frac{2C(1-C)N_x^2 d_x^2}{\pi^2}\cos\left(\frac{\pi x}{N_x d_x}\right)\right. \\ &\left. - \frac{(1-C)^2 N_x^2 d_x^2}{8\pi^2}\cos\left(\frac{2\pi x}{N_x d_x}\right)\right].\end{aligned} \tag{F.11}$$

The PQLs with lower $|h|$ have the highest peak values and, thus, affect the SLL to a greater extent. Therefore we consider $|h| = 1$. Since the QO feed can physically realise φ^{QO} as described by (F.3), we need to relate it to (F.11). To do this, we first represent (F.3) as $\varphi^{QO}(x) \approx -k_0 x^2/(2F)$, $F/(N_x d_x) > 0.5$, and use the cosine function approximation $\cos(\Theta) \approx 1 - \Theta^2/2$, $\Theta < 1$. Then, from (F.11), we can find the approximate value of the optimum focal distance F_{opt}:

$$F_{opt} \approx \frac{M N_x d_x^2}{\lambda_0}\left[C^2 + \frac{4C(1-C)}{\pi} + \frac{(1-C)^2}{2}\right]. \tag{F.12}$$

It should be mentioned that the employed two-term cosine expansion gives a high error for $\Theta > 1$. Therefore, (F.12) tends to underestimate F_{opt} for small C. Finally, we can find the normalized PQL power as $Q_h^2 = K^2_{h\,opt}/F_{00}^2$, where F_{00} is the main lobe field intensity (see (13) in [7]) $F_{00} = \int_{-N_x d_x/2}^{N_x d_x/2} A(x)\,dx = N_x d_x(C + 2(1-C)/\pi)$.

$$Q_h^2 = \frac{1}{N_x(1+Mh)^2}\frac{[C^2 + \frac{4C(1-C)}{\pi} + \frac{(1-C)^2}{2}]}{(C + 2(1-C)/\pi)^2}. \tag{F.13}$$

The highest PQL power is observed for $h = -1$. It determines the expected lower bound of the average SLL, which was found to be similar to the average phase error SLL of a PAA with phase errors uniformly distributed between $-\pi/M$ and $+\pi/M$ [9]. Let us consider two special cases.

- *Uniform amplitude distribution ($C = 1$)*:

$$F_{opt} \approx MN_x d_x^2/\lambda_0, \quad Q_{-1}^2 = 1/N_x. \tag{F.14}$$

- *Cosine amplitude distribution ($C = 0$)*:

$$F_{opt} \approx MN_x d_x^2/(2\lambda_0), \quad Q_{-1}^2 = \pi^2/(8N_x). \tag{F.15}$$

The last result evidences that the average SLL for the tapered distribution is almost the same as for the uniform one. This is due to the quasi-random nature of PQLs.

4 Numerical Simulations

In this section, we provide the far-field simulated results for linear PAAs, as computed from (F.1). For all the considered cases of the PAAs, the inter-element spacing is chosen $d_x = 0.6\lambda_0$ and the embedded element pattern has the shape as shown in Fig. 2. The linear array radiating element has been designed to enable grating lobe-free and impedance-matched beam steering up to $|\theta_s| = 45°$. The amplitude taper has been computed as $-20\log(A(x_1))$.

The simulated SLL performance for different array parameters is given in Fig. 3 versus the QO feed focal ratio $F/(N_x d_x)$. Here, we consider: maximum SLL, first SLL, and mean SLL. Each metric is computed first for each θ_s and then averaged over the $-40...40°$ beam-steering range. The mean SLLs are relatively invariant with focal ratio variations, and generally depend only on N_x, as predicted by (F.13). The computed values, however, are slightly (1-2 dB) higher, which is believed to be due to higher-order PQLs. For electrically large array apertures ($N_x > 10$), the increase in the amplitude taper from 0 to 10 dB effectively reduces the first SLL. Nevertheless, the two above-mentioned trends are no longer valid for small N_x with high taper values, when the PAA aperture is electrically small and PQLs cannot be effectively reduced. On the

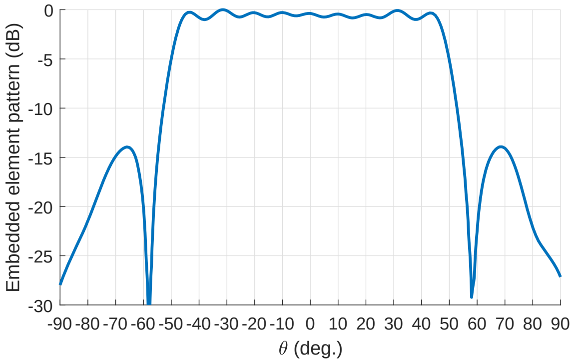

Figure 2: Normalized embedded element radiation pattern.

other hand, such configurations are rarely used for 1-bit PAAs. An important observation in Fig. 3 is that the maximum SLL curves demonstrate well-observable local minima. Positions of these minima are quite close to the expected values of optimum focal ratios (vertical dashed lines) as obtained from (F.12). The computed optimum value is underestimated for the tapered distributions, as we have discussed in Section 3.2. However, the demonstrated results clearly indicate the existence of the optimum focal ratio in terms of maximum SLL minimization. It is also important that the SLL improvement is more significant for tapered distributions, which is usually the case for the QO feeds. Fig. 4 shows achievable minimized maximum SLL as was found from numerical results analysis for different N_x and tapers.

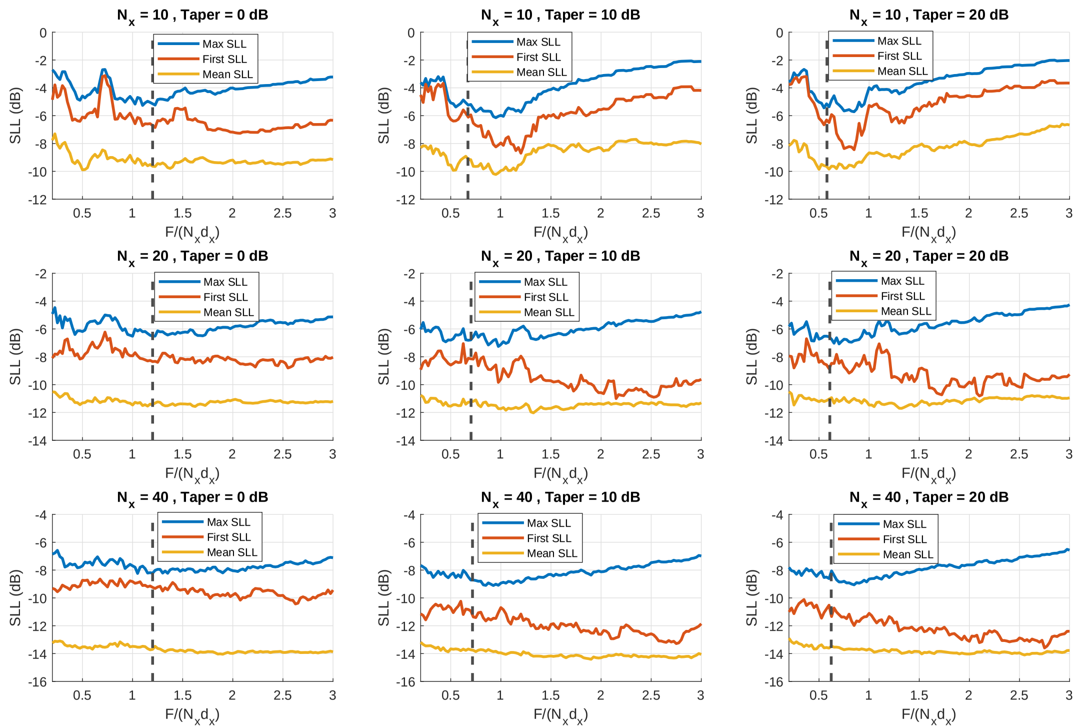

Figure 3: Averaged (over $|\theta_s| \leq 40°$ beam-steering range) SLL performance computed for different configurations of the 1-bit linear phased array antenna versus the focal ratio $F/(N_x d_x)$ of the quasi-optical feed. Vertical dashed lines show the expected optimum focal ratio values as approximated by (F.12).

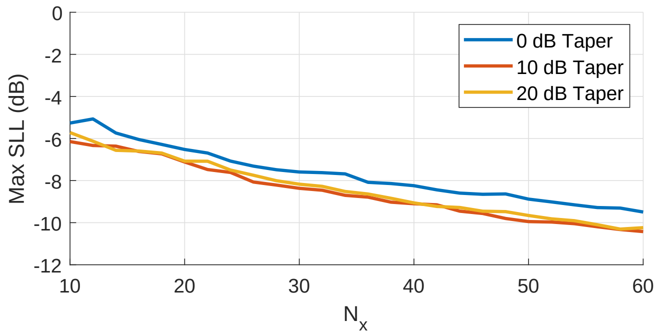

Figure 4: Averaged (over $|\theta_s| \leq 40°$ beam-steering range) maximum SLL versus the number of array elements for different tapers at the optimum (numerically defined) focal ratio $F/(N_x d_x)$ of the quasi-optical feed.

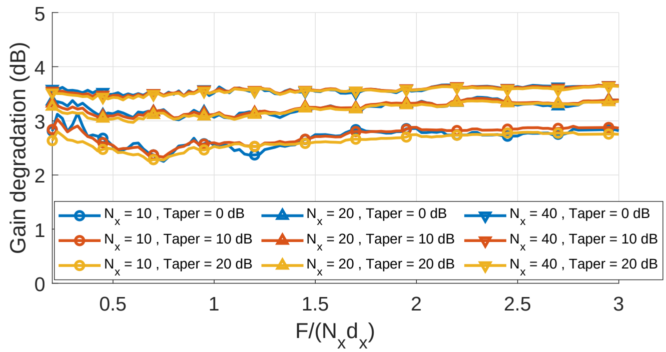

Figure 5: Averaged (over $|\theta_s| \leq 40°$ beam-steering range) gain degradation due to phase quantization errors for different array configurations versus the focal ratio $F/(N_x d_x)$ of the quasi-optical feed.

The array gain degradation due to the phase quantization errors was estimated as $|\sum_{i=1}^{N_x} A_i|^2/\max(|AF(\theta)|^2)$. The averaged results are shown in Fig. 5. With increasing of N_x, we can observe that the degradation reaches its asymptotic value $\text{sinc}(\pi/2)$ (see (13) in [7]).

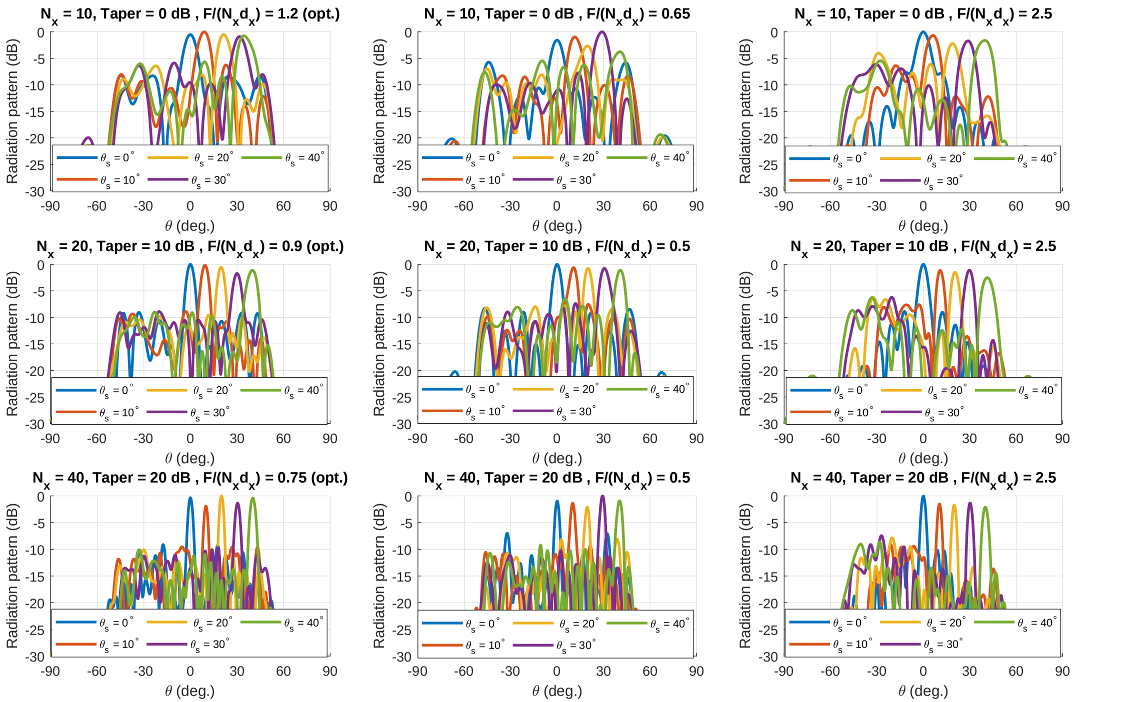

Figure 6: Far-field patterns for different 1-bit phased array antennas within 0...40° beam-steering range (10° step). The left column corresponds to the optimum focal ratios as obtained from Fig. 3

.

To illustrate the effect of the focal rati o on the far-field performance, the computed PAA radiation patterns are given in Fig. 6 for three configurations: $N_x = 10, 20, 40$ with Taper = 0, 10, 20 dB, respectively. Each configuration is considered for the optimum (left column, as found from Fig. 3), lower, and higher $F/(N_x d_x)$. It can be observed that while the mean SLL remains almost identical, the optimum focal ratios provide balanced SLL distributions over the entire visible angular space, and thus the maximum SLL is effectively reduced for the optimum cases. We, therefore, can summarise that the QO feed, providing the excitation phase distribution (F.3), indeed has the optimum focal ratio that depends on the distribution taper and realizes the lowest maximum SLL performance.

5 Conclusion

We have considered the optimum QO feed design for the linear PAA with the 1-bit phase resolution. The approach is based on the array PQLs non-overlapped distribution that provides “the best” phase quantization error randomization and realizes steerable radiation patterns with minimized maximum SLL. The main design relations for the optimum QO feed focal ratio were found analytically and verified numerically considering array channels amplitude distribution with an arbitrary taper. The proposed approach provides fairly accurate initial configuration of the QO feed. Further correction, of course, can be required to compensate for the edge and coupling effects as well as for non-perfect electrical performance of integrated PSs. The latter is a subject of future work. The extension of the method to the case of a 1-bit planar array (obtained by stacking of N_y linear arrays) is quite straightforward if the amplitude and phase distributions can be presented as $A(x, y) = A_x(x)A_y(y)$, $\varphi^{QO}(x, y) = \varphi_x^{QO}(x) + \varphi_y^{QO}(y)$. The average power SLL is then $\propto 1/(N_x N_y)$.

Acknowledgment

This work has received funding from the European Union’s Horizon 2020 research and innovation programme under the Marie Skłodowska-Curie grant agreement No 860023 and the Sweden-Taiwan Collaborative Research Framework Project “Antenna Technologies for Beyond-5G Wireless Communication" from the Swedish Foundation for Strategic Research.

References

[1] T. S. Rappaport, Y. Xing, O. Kanhere, *et al.*, "Wireless communications and applications above 100 GHz: Opportunities and challenges for 6G and beyond," *IEEE Access*, vol. 7, pp. 78 729–78 757, Jul. 2019.

[2] M. C. Viganó, D. L. del Río, F. Bongard, and S. Vaccaro, "Sparse array antenna for Ku-band mobile terminals using 1 bit phase controls," vol. 62, no. 4, pp. 1723–1730, Apr. 2014.

[3] A. Clemente, L. Dussopt, R. Sauleau, P. Potier, and P. Pouliguen, "Wideband 400-element electronically reconfigurable transmitarray in X band," vol. 61, no. 10, pp. 5017–5027, Oct. 2013.

[4] A. R. Vilenskiy, M. N. Makurin, C. Lee, and M. V. Ivashina, "Reconfigurable transmitarray with near-field coupling to gap waveguide array antenna for efficient 2D beam steering," vol. 68, no. 12, pp. 7854–7865, Dec. 2020.

[5] A. Clemente, F. Diaby, L. D. Palma, L. Dussopt, and R. Sauleau, "Experimental validation of a 2-bit reconfigurable unit-cell for transmitarrays at Ka-band," *IEEE Access*, vol. 8, pp. 114 991–114 997, 2020.

[6] J. G. Yang, J. Lee, and K. Yang, "A W-band InGaAs PIN-MMIC digital phase-shifter using a switched transmission-line structure," in *Proc. 2012 International Conference on Indium Phosphide and Related Materials*, Santa Barbara, CA, USA, Aug. 2012, pp. 1–3.

[7] A. R. Vilenskiy, M. N. Makurin, and C. Lee, "Phase distribution optimization for 1-bit transmitarrays with near-field coupling feeding technique," in *Proc. 14th European Conference on Antennas and Propagation, (EuCAP 2020)*, Copenhagen, Denmark, Mar. 2020, pp. 1–5.

[8] R. J. Mailloux, *Phased array antenna handbook*, Second. Norwood, MA: Artech House, 2018.

[9] M. S. Smith and Y. C. Guo, "A comparison of methods for randomizing phase quantization errors in phased arrays," vol. 31, no. 6, pp. 821–828, Nov. 1983.

[10] R. Maaskant, W. A. Shah, A. U. Zaman, M. Ivashina, and P.-S. Kildal, “Spatial power combining and splitting in gap waveguide technology,” *IEEE Microw. Wireless Compon. Lett.*, vol. 26, no. 7, pp. 472–474, Jul. 2016.

[11] C. J. Miller, “Minimizing the effects of phase quantization errors in an electronically scanned array,” in *Proc. 1964 Symp. Electronically Scanned Phased Arrays and Applications, RADC-TDR-64-225*, vol. 1, RADC Griffiss AFB, NY, USA, 1964, pp. 17–38.

[12] D. I. Voskresenskiy, L. I. Ponomarev, and V. S. Filippov, *Convex scanning antennas: basic theory and analysis methods.* Moscow: Soviet Radio, 1978, (in Russian).